AGSO

PARAFFIN SOLIDIFICATION IN MODEL FUELS

by

A.P. Radliński, L. Barré and D. Espinat

Record 1997/30

AGSO

AUSTRALIAN GEOLOGICAL SURVEY ORGANISATION

AUSTRALIAN GEOLOGICAL SURVEY ORGANISATION
DEPARTMENT OF PRIMARY INDUSTRIES & ENERGY

AGSO RECORD 1997/30

Paraffin Solidification in Model Fuels

A. P. Radliński[†], L. Barré[‡] and D. Espinat[‡]

[†]Australian Geological Survey Organisation, GPO Box 378,
Canberra City, A.C.T. 2601, Australia.
[‡]Institut Français du Pétrole, 1 et 4, avenue de Bois-Préau,
BP 311, 92506 Rueil-Malmaison Cedex, France.

DEPARTMENT OF PRIMARY INDUSTRIES & ENERGY
Minister for Resources & Energy: Senator the Hon. Warwick Parer
Secretary: Paul Barratt

AUSTRALIAN GEOLOGICAL SURVEY ORGANISATION
Executive Director: Neil Williams

ISSN 1039 - 0073
ISBN 0642250391

Research described in this report was initiated at the Institut Français du Pétrole. The experiments have been performed and partial data analysis was carried out at IFP. The interpretative work and report writing has been completed in Canberra.

Acknowledgement: We thank Mr. J. P. Durand and Mr. P. Gateau for providing the additives used in this study.

Contents

Summary

The major part of the study described in this report was performed on model diesel fuels. These are solutions of aliphatic molecules in an aromatic solvent. We have used either a realistic mixture of normal alkanes in the range C8 to C29 (peaked at C16) based on one of the commercial diesel fuels (called mixture A), or a single n-alkane dissolved in toluene or nitrobenzene. The concentration of n-alkanes in model fuels studied by us varied from 10% to 80%, but most data were obtained for concentrations 10%, 15% and 20%, which are close to these found in commercial diesel fuels.

There are two major issues addressed in this work. Firstly, we have developed the methodology and acquired systematic experimental data that enabled us to gain insight into the microscopic mechanisms of the low-temperature solidification of diesel fuels. Secondly, we have analysed quantitatively the T_c-depressant action of four different polymethylacrylate additives in model fuels.

We have employed a number of experimental methods. The main body of data reported here comes from the video-enhanced optical observations of the fuel solidification process, small angle X-ray scattering and the small angle neutron scattering. These experiments were performed in a wide temperature range above and below T_c (from $-100°C$ to $80°C$ in some cases). Other methods, which have been used less extensively, included gas chromatography, dynamic light scattering, scanning tunneling microscopy and surface tension measurements. We have also performed some wide angle X-ray scattering experiments on frozen fuels, but the results are not discussed in this report.

It turns out that paraffin solidification in model fuels is a complex process. For single n-alkane solutions, the n-alkane molecules begin to aggregate into small monodisperse objects at temperatures as high as $40°C$ above T_c. The geometry of these objects is flat in nitrobenzene solutions, regardless of the paraffin chain length, but in toluene solutions changes to spherical for heavier paraffins. Only several n-alkane molecules in all-trans configuration are typically contained in a single flat aggregate whose aspect ratio (length-to-width) may vary from 1 to 2. The concentration of aggregates increases as the temperature decreases and reaches its maximum at T_c. At this temperature up to 30% of the total number of n-alkane molecules may be contained in aggregates.

For the nitrobenzene solutions of mixture A, the flat aggregates are polydis-

perse and their size distribution is consistent with a model according to which only molecules of similar chain length aggregate with each other. In contrast to this, the aggregates in toluene are spherical and their size distribution is a polydisperse bimodal. 99.8% of the paraffin volume fraction aggregates into densely-packed spheres of mean radius 5.25Å and the remainder into much larger spherical objects of mean radius 39.3Å. As the temperature decreases below T_c, the aggregates neither coalesce nor become nuclei of crystallisation. They continue to co-exist with the solid phase down to temperatures well below T_c, until eventually the last pockets of liquid solidify. For the 20% nitrobenzene solutions of mixture A there is a preferential fractionation of paraffins into the solid phase: the heavy chains solidify first and then, at about 10°C below T_c, the lightest species follow. In contrast to this, during the solidification of the less concentrated nitrobenzene solutions as well as toluene solutions (of any concentration of mixture A) no fractionation is observed.

Fuels gradually solidify as the temperature decreases below T_c, but under the quenching conditions used by us the growth of the crystalline phase is rather limited. The bulk of the solid phase remains amorphous and solidification occurs via the gellification rather than crystallisation process. The details of fuel solidification depend both on the paraffin type and concentration and the type of solvent. Although certain general features can be identified, the model fuel solidification process is system-specific. Therefore, in order to fully recognise the variety of possible patterns and modes of solidification, research on the properties of fuels of different compositions (and for a number of paraffin concentrations in particular) is a necessity.

We have investigated the effect of four different polymeric additives on the crystallisation temperature of 10% and 20% solutions of mixture A in toluene and nitrobenzene. These additives were pure polymethylacrylates containing either 12 or 18 carbon atoms in the side chain. For each side chain length two polymers were used: one of the number average molecular mass, M_n, of about 5000 and another of about 40000.

The response curves for model fuels (T_c versus the additive content) were obtained up to the polymer concentration of 3000 ppm. Typically, the response is best for small additive concentrations (about 100 ppm) and saturates at about 1000 ppm. The response of the toluene-based model fuels (maximum decrease of T_c of about 10°C at 1000 ppm) is by a factor of 10 stronger than for their nitrobenzene-based counterparts.

We have assumed a model according to which certain proportion of n-alkanes aggregates around the additive molecules and, therefore, does not take part in the normal crystallisation process. This enables one to calculate on the basis of experimental data the number of paraffin molecules eliminated from the crystallisation process per monomer of additive. For the 18-carbon side chain polymethylacrylates this number varies from about 1000 (at additive concentration 100 ppm) to about 100 (at additive concentration 1000 ppm) and is similar for the 20% toluene-based and nitrobenzene-based model fuels. For the

12-carbon side chain additives the corresponding numbers are in the range 15-100 and 10-20, respectively. It is a clear-cut conclusion that our model enables a comparison of the T_c-depressant additive effectiveness in different fuels based on the proposed universal mechanism for the molecular affinity. It transpires that the decisive factor for a T_c-depressant effectiveness is a good match between the polymethylacrylate side chain length and the paraffinic chain length. The chain length distribution for mixture A is peaked at C15-C16 and, therefore, it is much more compatible with the 18-carbon side chain polymethylacrylates than with the 12-carbon ones.

The additive conformation in toluene at temperatures 25°C and −7°C was studied using the Zimm analysis of small angle neutron scattering data. The weight average molecular mass, M_w, radius of gyration, R_g, and the second virial coefficient, A_2, were determined for the two light additives ($M_n \approx 5000$). It turned out that the polydispersity of these molecules, defined as $\frac{M_w}{M_n}$, is 1.6 for the 18-carbon side chain polymer and 2.9 for the 12-carbon one. The corresponding values of R_g are 22 Å and 27 Å, respectively. This difference is caused by different polymer-solvent interactions for both species: they are attractive for the short side chain polymer ($A_2 = 0.0013$) and repulsive for the long side chain one ($A_2 = -0.0014$). Also, we have established that the values of R_g and A_2 for the 12-carbon side chain polymer do not change down to the temperature −7°C. This indicates that the polymer conformation also remains unchanged, which rules out the possibility of polymer crystallisation in this temperature range.

The results of small angle neutron scattering experiments performed on 20% solutions of mixture A in toluene containing several thousands ppm of additives are not conclusive, but remain in general agreement with our model of additive action in model fuels. In particular, upon addition of polymer we observe three- to four-fold swelling of the radii of small spherical aggregates observed in the additive-free model fuels. Furthermore, the large aggregates either grow to the mean radius of 49 Å (for heavy polymers) or dissolve completely (for light polymers). The scattering cross section becomes by a factor of five smaller than in similar solutions without additives, which strongly indicates that the aggregates become penetrated by solvent molecules. However, the interpretation may be further complicated due to the fact that the aggregates may have spatially varying contrast profile, which has been ignored in our analysis. In order to fully address the complex issue of the additive-induced microstructure evolution more small angle scattering experiments are needed, in particular for various additive concentrations and in a wider Q-range.

In the course of this work it became apparent that, owing to the chemical and structural complexity of model fuels, several complementary experimental techniques should be used in order to gain better insight into various aspects of the observed phenomena and make connection with other work. We have used gas chromatography to acquire data about the chemical composition of liquid phase in freezing fuels at temperatures below T_c. Dynamic light scattering

and scanning tunneling microscopy were employed to independently confirm the existence of aggregates in the liquid phase and observe the growth of solid phase at the interface with highly oriented pyrolytic graphite. Preliminary surface tension results confirmed a possibility of surface crystallisation in pure mixture A. Wide angle X-ray scattering experiments (not reported here) provided an insight into the structure of solid phase in frozen fuels. Finally, the near-infrared spectroscopy data and preliminary experiments using a commercial infrared video camera indicate that direct optical observations of paraffin crystallisation in black (non-transparent) crude oils are possible. Therefore, the methodology developed in this work for diesel fuels can be readily extended to more complex systems, including crude oils.

Chapter 1

Introduction

Crude oils are complex natural colloidal systems composed of saturated hydrocarbons, aromatic hydrocarbons, resins and asphaltenes [1]. Crude oil may contain several hundred different chemical compounds, among which the normal alkanes, isoalkanes and cycloalkanes typically amount to about 50% of total mass. Diesel fuels are middle distillates of crudes and typically contain 10% to 30% of n-alkanes. The precipitation of waxes during the production, storage and use of crude oils and fuels is a serious industrial problem of costly consequences. From the analysis of wax deposits it has been long recognised that normal alkanes are the major component of precipitated solids. In the industrial practice various curative mechanical and thermal methods for the removal of waxy deposits have been used. Furthermore, there is a range of chemical additives specifically developed for preventing wax solidification at the low temperatures. All these activities require better understanding of the paraffin solidification at various levels, from the purely descriptive identification of various stages of this process to the molecular-level structural concepts and predictive thermodynamic models. It has been the purpose of this project to contribute to this knowledge.

The increasing degree of complexity of paraffinic systems may be illustrated by the following list:

- Pure normal alkane.
- Binary or ternary mixture of n-alkanes.
- Binary solution of a single n-alkane in a single aromatic solvent.
- Model fuel: (a) solution of a mixture of n-alkanes in a single aromatic solvent or (b) solution of a single n-alkane in a natural (paraffin-free) diesel solvent.

- Model crude oil: (a) solution of a crude oil wax in a single aromatic solvent or (b) solution of a single n-alkane in a natural (paraffin-free) crude oil solvent.
- Diesel fuel: middle distillate, a solution of a multicomponent light wax in a multicomponent natural solvent.
- Crude oil.

Systems in the beginning and towards the end of the list have been extensively studied and vast literature on the subject is available. Below we give only limited reference to some of the previous work in order to indicate some of the areas of interest. Two useful major review articles on the properties of n-alkanes are available: an older one by Turner [2] and a recent one in a book edited by Small [3]. The latter reference contains comprehensive tables of the thermal properties of n-alkanes. Many detailed reports on various aspects of n-alkane crystallisation have been published. The subjects of interest included the kinetics of crystal nucleation in n-alkane liquids by the droplet technique [4], the crystal structure of $C_{36}H_{74}$ by X-ray diffraction [5], the thermally-driven phase transitions in $C_{33}H_{68}$ [6] and in a number of C19 to C46 n-alkanes [7], differential scanning calorimetry and infrared spectroscopy study of the solid state phase transitions in the odd n-alkanes C17 to C29 [8] and a detailed X-ray diffraction study of the rotator phase for the paraffin range C20 to C33 [9].

There have been at least several hundred published papers describing the properties of pure n-alkanes. Owing to this work, the crystallisation process in n-alkanes is very well known. In the range C9-C29 the stable (low temperature) crystal structure is orthorombic for the paraffins with odd number of carbon atoms and triclinic for the even n-alkanes. When the temperature is increased, there is a first-order phase transition to the rotator phase [9]. In this phase, the paraffinic chains are packed in a pseudo-hexagonal or a two-dimensional disordered rectangular packing and are free to rotate along the long axis ([10], [11]). This is an intermediate state of matter between the solid and liquid, one not encountered in simple liquids. The rotator phase melts to an isotropic liquid, but for the odd paraffins from C23 upwards it first undergoes a transition into a true (rotator) hexagonal phase. These transformations are illustrated in the phase diagram in figure 1.1.

The literature on wax solidification in crude oils and petroleum products, including fuels, is very extensive and ranges from purely scientific, through the applied to typically industrial reports. A review of methods used for thermal analysis of petroleum products has been published by Wesolowski [12]. Selected examples of other work are: an early X-ray diffraction and electron microscopy study on crystal morphology of waxes present in tubular equipment [13]; a series of papers on wax precipitation from North Sea crude oils using DSC, polarisation microscopy and viscometry [14], determination of solid phase content using NMR [15] and thermodynamic modelling [16] as well as the application

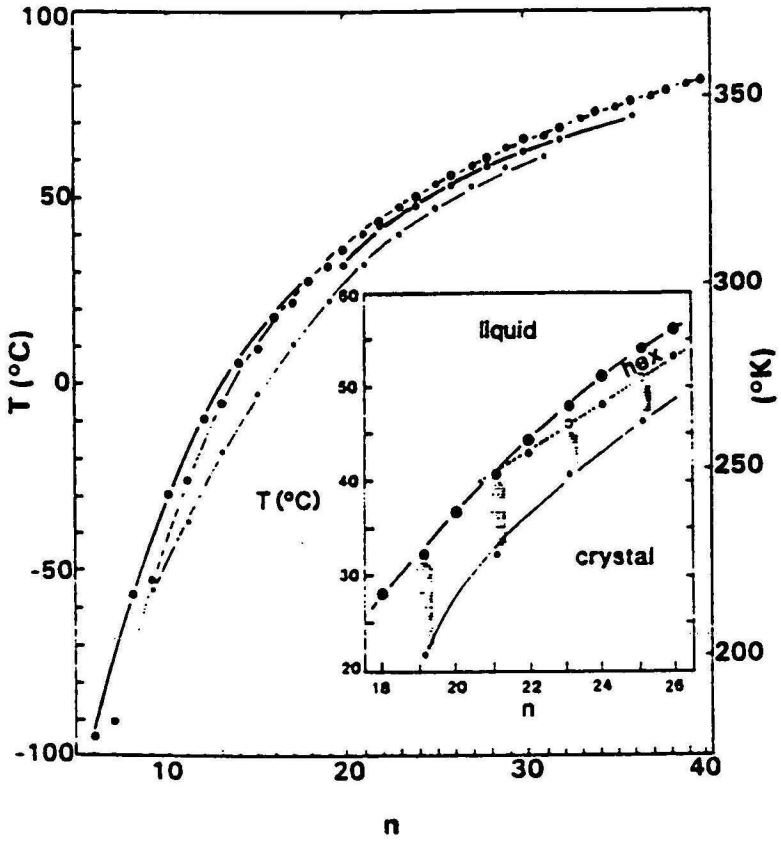

Figure 1.1: Transition temperatures for n-alkanes. Black symbols are even-number carbon alkanes; grey symbols are odd-number carbon alkanes. Large circle indicates melting to an isotropic liquid, while small circle indicates transition from tightly packed crystal to rotator phase. (Inset) Detail for C18 - C26 alkanes. Open gray circles indicate transition from the pseudo-hexagonal to true hexagonal chain packing. The shaded vertical lines show the temperature range over which the pseudo-hexagonal packing exists in the odd-chain molecules. (After [17], page 195).

of high temperature high resolution gas chromatography to paraffinic deposits in petroleum production pipelines [18].

There is an on-going interest in the thermal analysis of crude oils and their derivatives. One of the early works on waxes and petrolatums is [19]; Miller [20] published for the first time a comprehensive scheme for studies of hydrocarbon waxes by thermal analysis. There is a series of papers in French on DSC investigations of single n-alkanes dissolved in a paraffin-free diesel fuel base solvent ([21], [22], [23]), an analysis of thermal stability of the microcrystalline wax melts [24], a report on solid state phase transitions in petroleum waxes [25], and a DSC and polarisation microscopy work on the wax crystallisation in crude oils and on crystallisation of pure paraffins in oil-free crude oils [26]. As illustrated above, the experimental techniques like X-ray diffraction, DSC, polarisation microscopy, chromatography and viscometry have been the typical tools used in research on wax solidification in crude oils and their derivatives.

There has been also another line of approach, based on the recognition that petroleum products are nothing but complex colloidal systems and applying research methods developed for use in the colloid science. These methods include such sophisticated techniques as Small Angle X-ray Scattering (SAXS), Small Angle Neutron Scattering (SANS) and freeze-fracture electron microscopy. An example of such approach may be the study by Espinat and coworkers on the asphaltenes [27].

Little work has been published on the intermediate systems, model crudes and model fuels ([21], [22], [23] and [26]). Even the few systems studied have not been fully controlled since the natural crude oil or diesel fuel solvents have been used. Yet understanding of the model systems is a crucial step for the development of general ideas about paraffin solidification in natural petroleum products. The reality is that although a large body of data is available for pure n-alkanes and their binary and ternary solutions, these systems are too simple compared to crude oils to justify direct comparisons and extrapolation of results. On the other hand, at the current stage of our knowledge the fuels and crude oils are too complex to allow for anything but phenomenological, system-specific description of their behaviour.

This project has been an attempt to try and narrow down the conceptual gap between the simple n-alkane systems and natural petroleum products. We have decided to focus on the model systems of known composition and to use a number of complementary experimental techniques. We have not been rigid in this approach, however, and have investigated at least certain aspects of practically every system from our list, from pure n-alkanes to crude oils. Crude oils and model crudes have been studied under an umbrella of a different project and the results have been reported separately [28].

Chapter 2

Small angle scattering in model fuels: background information

2.1 Theoretical background

2.1.1 General considerations

The theoretical foundations of the Small Angle Scattering (SAS) techniques are discussed extensively in several publications ([29, 30, 31, 32, 33] and references cited therein). In this section we only present a general overview of the theory, with particular emphasis on the aspects directly applicable to the interpretation of our results.

The principle of SAS experiments is illustrated in figure 2.1. A flux of monochromatic neutrons or X-ray photons propagating in the direction of their wavevector $\mathbf{K_0}$ is elastically scattered inside a sample of volume V. One measures the intensity dI scattered in the direction $\mathbf{K}$, where by convention $\mathbf{K} - \mathbf{K_0} = \mathbf{S}$ and the quantity $\mathbf{Q} = 2\pi\mathbf{S}$ is called the scattering vector.

The magnitude of the scattering vector is related to the radiation wavelength and the scattering angle Θ:

$$Q = \frac{4\pi}{\lambda} \sin\Theta \tag{2.1}$$

The upper limit of Θ in SAS experiments is about 5°, whereas the lower limit is determined by the incident beam divergence. As the linear size of objects that contribute most to the scattering at a given Q-value is $\frac{2\pi}{Q} = \frac{\lambda}{2\sin\Theta}$, the choice of wavelength and the angle Θ determine the suitability of experimental system for studying objects within a given size range. In experimental practice

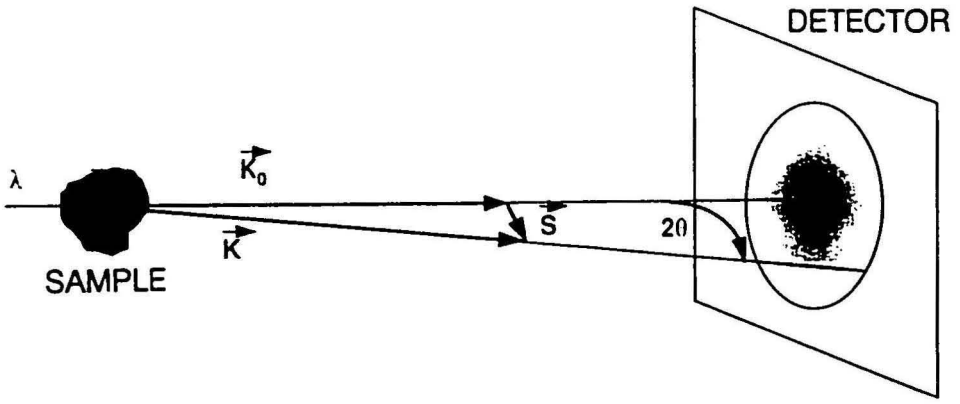

Figure 2.1: Schematic diagram of a small angle scattering experiment.

the range of Θ can be varied by changing the sample-detector distance and in the case of neutron scattering the wavelength can be adjusted in the range 3Å to 20Å, depending on the facility used. The available Q-range is one of the most important characteristics of a SAS experimental system. Table 2.1 compares Q-ranges and the corresponding particle size ranges for several SANS and SAXS facilities, some of which were used in this work. It can be seen that SAS techniques are suitable for studying objects in the size range from nearly atomic to microscopic. If the incident flux of the scattering particles is denoted Φ_0 (*i.e.* $\Phi_0 = I_0/s$, where I_0 is the incident intensity and s is the cross section area of sample), then:

$$dI \propto \Phi_0 \frac{d\sigma}{d\Omega} d\Omega \tag{2.2}$$

where $d\sigma$ is the elemental scattering cross section and $d\Omega$ is the solid angle element. The quantity $\frac{d\sigma}{d\Omega}(Q)$ is called the differential cross section. $\frac{d\sigma}{d\Omega}(Q)$ contains information about the scattering properties of the system under study and it is the purpose of SAS experiment to measure this quantity.

The magnitude of $\frac{d\sigma}{d\Omega}(Q)$ explicitly depends on the character of the radiation-matter interaction. Neutrons interact directly with the nuclear potential and the scattering amplitude, $A(\mathbf{Q})$, is given by:

$$dA(\mathbf{Q}) = \rho_n(\mathbf{r}) \exp(-i\mathbf{Q}\mathbf{r}) dV \tag{2.3}$$

where $\mathbf{Q}$ is the scattering vector, dV the scattering volume element and ρ_n is

Table 2.1: Q-ranges and the corresponding particle size ranges accessible with several SAS arrangements. The IFP SAXS system and the PAXE facility were used in the course of this work. The instrument D11 in ILL, Grenoble, and the USAXS system in CEA, Saclay, are examples of modern SAS instruments that enable studies of particularly large particles.

Experimental arrangement	Q_{min} (Å^{-1})	Q_{max} (Å^{-1})	l_{min} (Å)	l_{max} (Å)
SAXS IFP	9.9×10^{-3}	0.66	10	630
USAXS CEA Saclay	5.0×10^{-4}	0.1	65	12000
SANS PAXE LLB Saclay	3.0×10^{-3}	4.0	1.6	2100
SANS D17 ILL Grenoble	3.0×10^{-3}	1.0	6	2100
SANS D11 ILL Grenoble	1.0×10^{-3}	0.5	13	10000

Table 2.2: Neutron coherent scattering length densities for selected nuclei.

Nucleus	H	D	^{12}C	^{14}N	^{16}O
ρ_n (10^{-12} cm)	−0.3739	0.667	0.6646	0.936	0.5803

the coherent scattering length density for neutrons defined as:

$$\rho_n(\mathbf{r}) = \frac{1}{V}\sum_i b_i(\mathbf{r} - \mathbf{r}_i) \tag{2.4}$$

where the summation is extended over all the nuclei i contained in the scattering volume V. The coherent scattering lengths for the naturally abundant isotopes, b_i, are well known. For light elements they are dominated by the resonant scattering and vary widely from one nucleus to another. They can be totally different for two different isotopes of one nucleus, the most important example being the hydrogen and deuterium. Coherent length densities for the nuclei present in the substances studied in this work are given in table 2.2.

Electromagnetic radiation in X-ray domain interacts with the electronic cloud of atoms. The scattering amplitude for X-rays is given by:

$$dA(\mathbf{Q}) = I_e\rho_e(\mathbf{r})\exp(-i\mathbf{Q}\mathbf{r})dV \tag{2.5}$$

where $I_e = \frac{e^2}{mc^2} = 2.82 \times 10^{-13}$ cm is the scattering amplitude of a single electron and $\rho_e(\mathbf{r})$ is the electronic density (i.e. number of electrons per unit volume). By comparison of equations 2.3 and 2.5 one can see that the product $I_e\rho_e(\mathbf{r})$ plays the same role in SAXS as the scattering length density $\rho_n(\mathbf{r})$ does in SANS.

As discussed above, the SAS techniques have been specifically designed for studies on large objects and do not have the atomic resolution of the classical wide-angle X-ray diffraction. Scattering is a process which occurs on the density fluctuations either on the interface between two phases or within a single phase. The composition of a phase may be complex; for instance, it may be a mixed crystal of several normal alkanes. The neutron scattering length density for such a single-phase, complex mixture of molar mass M is:

$$\rho_n = \frac{N_A d}{M} \sum_j p_j (\sum_i s_i b_i)_j \tag{2.6}$$

where N_A is the Avogadro number, d is density, s_i is the proportion by number of nucleus i in the compound j and p_j is the proportion by molecular number of the compound j in the mixture.

For X-ray scattering, the product $I_e\rho_e$ is simply:

$$I_e\rho_e = \frac{N_A d}{M} N_e I_e \tag{2.7}$$

where N_e is the number of electrons per one supra-molecule of composition as in the double summation in equation 2.6.

The quantity measured in the SAS experiment is the scattering intensity $I(Q)$, equivalent to the differential scattering cross section $\frac{d\sigma}{d\Omega}$:

$$I(Q) = A(Q)A^*(Q) = C_0 \int_V \gamma(\mathbf{r}) \exp(-i\mathbf{Q}\mathbf{r}) dV \tag{2.8}$$

where $\gamma(\mathbf{r})$ is the (nuclear or electronic) density-density correlation function and C_0 is unity for neutrons and I_e^2 for X-rays. Thus, the general result follows that the small-angle scattering intensity is a Fourier transform of the density-density correlation function.

For a multi-phase system the correlation function has the form ([34, 35]):

$$\gamma(\mathbf{r}) = \sum_i \sum_j P_{ij}(\mathbf{r})(\rho_i - \rho_0)(\rho_j - \rho_0) \tag{2.9}$$

where $\rho_i = \rho_{ei}$ or ρ_{ni}, ρ_0 is the volume average of ρ_e or ρ_n, indices i and j indicate separate phases of the system and $P_{ij}(\mathbf{r})$ is the probability that a point

at distance $\mathbf{r}$ away from a randomly selected point in phase i happens to be in phase j. For a two-phase system equation 2.9 in the integral form reduces to:

$$\gamma(\mathbf{r}) = \int_V \Delta\rho(\mathbf{r}')\Delta\rho(\mathbf{r}'+\mathbf{r})dV' \tag{2.10}$$

where $\Delta\rho(\mathbf{r}) = \rho(\mathbf{r}) - \rho_0$ is the fluctuation of the electronic or nuclear density at point $\mathbf{r}$ from its average value ρ_0. Finally, for the isotropic systems one can average equation 2.8 over all the directions of $\mathbf{r}$ and obtain [31]:

$$\frac{d\sigma}{d\Omega}(Q) = 4\pi C_0 \int_0^\infty r^2\gamma_0(\mathbf{r})\frac{\sin Qr}{Qr}dr \tag{2.11}$$

and, inversely:

$$\gamma_0(\mathbf{r}) = \frac{1}{C_0}\int_0^\infty \frac{Q^2}{2\pi^2}I(Q)\frac{\sin Qr}{Qr}dQ \tag{2.12}$$

where

$$\gamma_0(\mathbf{r}) = \frac{\gamma(\mathbf{r})}{\int_V \Delta\rho^2 dV} \equiv \frac{\gamma(r)}{V\overline{\Delta\rho^2}}. \tag{2.13}$$

The above substitution of $\gamma_0(\mathbf{r})$ for $\gamma(\mathbf{r})$ is useful since $\gamma_0(\mathbf{r}=0)$ is normalised to unity. The quantity $\overline{\Delta\rho^2}$ is the volume-average square of the density fluctuations.

The traditional way of expressing the scattering cross section is:

$$\frac{d\sigma}{d\Omega}(Q) = C_0 V\overline{\Delta\rho^2}F(Q) \tag{2.14}$$

where the form factor $F(Q)$ is given by:

$$F(Q) = 4\pi\int_0^\infty r^2\gamma_0(r)\frac{\sin Qr}{Qr}dr \tag{2.15}$$

For a strictly two-phase system of densities ρ_1 and ρ_2, respectively, one gets:

$$\overline{\Delta\rho^2} = (\rho_1-\rho_2)^2\Phi_1(1-\Phi_1) \tag{2.16}$$

It follows from equations 2.8, 2.9, 2.10 and 2.11 that given the geometry of the scattering object one can exactly calculate the Q-dependence of $\frac{d\sigma}{d\Omega}$. The inverse is not possible, though. The experimental value of $\frac{d\sigma}{d\Omega}(Q)$ can be only known for some values of Q and with limited accuracy. This enables one to calculate the correlation function, for example from equation 2.12, only with limited precision. As in the process of calculating the correlation function some details

of the structural information are inevitably lost, there is no way of deconvoluting the precise particle shape from the experimentally determined correlation function [36].

In the view of this situation the interpretation of SAS results, perhaps with the exception of few simple cases, is as much an art as science. The usual procedure can be roughly divided into two major steps. Firstly, the limiting behaviour of $\frac{d\sigma}{d\Omega}$ in the large-Q and small-Q regions is analysed in order to work out some general characteristics of the scattering systems. This is discussed in the following section. Secondly, using those characteristics a structural model of the scatterer is postulated and attempted to fit to the experimental data. This can be done either by using general formulae like 2.11 or, more often, by approximating the shape of scatterer by simple geometrical forms of (polydisperse if necessary) spheres, rods, discs, slabs, self similar structures, etc., for which the analytical expression for $F(Q)$ (equation 2.15) is known.

That usually does not work the first time around and may take a great deal of skill and time to accomplish. The major difficulty in this trial and error procedure is related to the fact that the scattering curves are usually smooth and can be fitted reasonably well by many different structural models if several fitting parameters need to be used, which is often the case. On the other hand, if the model requires only one or two parameters, the fit may not be perfect and it has to be decided whether this is caused by the inadequacy of the model, or its approximate character, or the experimental artefacts.

While interpreting the SAS data serious errors of judgement can be made and, therefore, it is a good practice to seek independent confirmation of the presumed structure by other experiments. The best, if applicable, are the direct imaging techniques like the optical microscopy, electron microscopy, tunneling microscopy and other related means. One has to keep in mind, however, that SAS techniques are the only non-invasive methods for the study of submicroscopic structures and, therefore, they enable one to gain structural information about the specimen in its natural state: in solution, at high or low temperature, under stress, etc. In contrast to this, the direct imaging techniques are by nature invasive as they require the sometimes quite involved process of sample preparation. This process may cause profound structural changes in the sample, in particular inside the soft matter. The only way to quantify those changes would be to employ the SAS techniques, which makes the argument somewhat circular.

2.1.2 The limiting behaviour of $\frac{d\sigma}{d\Omega}$.

Small-Q limit: the Guinier region.

Guinier has shown [37] that in the small-Q region the Q-dependence of the scattering cross section for any scattering system flattens out with the following

Table 2.3: Radii of gyration for three simple geometrical objects.

Object	R_g^2
Sphere of radius R	$\frac{3}{5}R^2$
Parallelepiped of sides a, b and c	$\frac{1}{12}(a^2+b^2+c^2)$
Cylinder of height $2H$ and radius R	$\frac{1}{2}R^2+\frac{1}{3}H^2$

limiting behaviour:

$$I(Q) = I(0)\exp(-\frac{R_g^2Q^2}{3}) \tag{2.17}$$

provided the values of Q are such that $QR_g \ll 1$, where R_g is the radius of gyration of the scattering particle. For a homogeneous particle R_g is defined as:

$$R_g^2 = \frac{1}{2}\frac{\int_0^\infty \gamma_0(x)x^4dx}{\int_0^\infty \gamma_0(x)x^2dx} \tag{2.18}$$

and can be calculated for any shape. Radii of gyration for three simple geometrical objects are listed in table 2.3.

It follows from equation 2.17 that the plot of $\log I(Q)$ versus Q^2 gives a straight line with a slope -$\frac{1}{3}R_g^2$, independently of the shape of the scattering object. Furthermore, the limiting value of the scattering cross section is:

$$\frac{d\sigma}{d\Omega}(0) \equiv I(0) = \Phi_1(1-\Phi_1)(\rho_1-\rho_2)^2\mathcal{V} \tag{2.19}$$

where $\mathcal{V}$ is volume of a *single* scattering particle and Φ_1 is the total volume fraction of these particles. This result indicates that a process of particle aggregation which does not change the first three terms in equation 2.19 would result in the increase of $I(0)$ proportional to the number-average volume of the aggregate.

The relation 2.17 can be further specialised in order to obtain more specific structural information, provided the analytical form of F(Q) is known. There are two particular geometrical shapes of interest in this study: polymer chains in solution and flat plates of near-atomic thickness. These two cases are discussed next.

The Zimm plot.

The analysis of scattering data for polymer molecules in solutions can be conveniently done using the classical Zimm approach [38]. In this case the scattering

law in the Guinier region specialises to the following form:

$$\frac{Ac}{\frac{d\sigma}{d\Omega}(Q)} = \frac{1}{M_w}(1 + \frac{Q^2 R_g^2}{3}) + 2A_2(Q)c \tag{2.20}$$

where

$$A = C_0 \frac{(\rho_1 - \rho_2)^2}{N_A d_1^2} \tag{2.21}$$

Equation 2.20 has been derived assuming that $2cM_wA_2(Q) \ll 1$. M_w is the weight-average polymer molecular mass (in g/mole), A_2 is the second virial coefficient of the osmotic pressure, c is the polymer concentration (in g/cm^3) and d is the polymer density (in g/cm^3).

The three parameters characterising the polymer molecules and their interaction with solvent, R_g, M_w and A_2, can be calculated along the lines of equation 2.20 as three independent limits:

$$M_w = (\lim_{Q\to 0}\lim_{c\to 0} \frac{Ac}{\frac{d\sigma}{d\Omega}(Q)})^{-1} \tag{2.22}$$

$$R_g = (\frac{3}{Q^2}(\lim_{c\to 0} \frac{M_w Ac}{\frac{d\sigma}{d\Omega}(Q)}) - 1)^{\frac{1}{2}} \tag{2.23}$$

$$A_2 = \frac{1}{2c}((\lim_{Q\to 0} \frac{Ac}{\frac{d\sigma}{d\Omega}(Q)}) - \frac{1}{M_w}) \tag{2.24}$$

These three limits can be conveniently determined graphically by constructing the so-called Zimm plot. In Zimm plot, several series of experimental values of $\frac{d\sigma}{d\Omega}(Q)$ obtained for the same sequence of Q-values for several polymer concentrations c are plotted in the coordinate system $\frac{Ac}{I(Q)}$ (the ordinate) versus $Q^2 + kc$; k is an arbitrary constant selected in such a way that the range of $Q^2 + kc$ values for a given polymer concentration c would overlap with its counterpart for the next concentration after several experimental points (i.e., after several Q-values). The final result does not depend on the specific value of k. An example of a Zimm plot is presented in figure 2.2.

Flat discs: the limiting behaviour in small-Q region.

Cylinder is one of the simple shapes for which an analytical expression for F(Q) is available (see next section). If the cylinders radius is denoted by R and its height by $2H$ then for flat cylinders (discs) $R \gg H$. In the Q-range such that $QH \leq 1$ and $QR \gg 1$ one gets:

$$F(Q) = \mathcal{V}\frac{2}{(QR)^2} \exp\left[-\frac{(QH)^2}{3}\right] \tag{2.25}$$

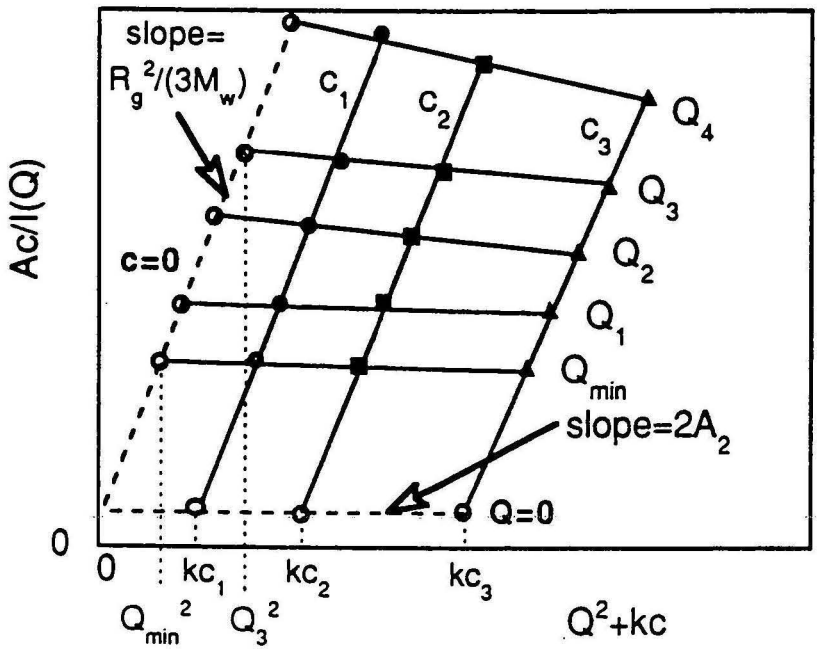

Figure 2.2: An example of Zimm plot with detailed explanations. Experimental data for three different polymer concentrations are shown using three sets of full symbols. Open circles indicate the graphically determined limits: the nearly-horizontal broken line for $Q \rightarrow 0$ and the nearly-vertical one for $c \rightarrow 0$. The positions of open circles were determined in the former case by taking the intercepts of lines least-square fitted to the constant-concentration data series with the vertical dotted lines corresponding to the appropriate kc-values ($k = 10$ in the case shown in the figure). In the latter case, the limiting values were graphically found by intercepting the lines fitted to the constant-Q experimental data with the vertical dotted lines corresponding to the appropriate Q-values (Q^2_{min}, Q^2_2, Q^2_3, etc.). The slopes of the $Q = 0$ and $c = 0$ limiting lines are $2A_2(Q)$ and $\frac{1}{3M_w}R_g^2$, respectively. These two limiting lines intercept the ordinate at the point $\frac{1}{M_w}$.

which for yet smaller Q-values ($QH \ll 1$ and $QR \gg 1$) simplifies to:

$$F(Q) = \mathcal{V}\frac{2}{(QR)^2} \tag{2.26}$$

One should note that the above formulae are valid in the Q-range outside the Guinier region; indeed, for a flat cylinder $R_g^2 \simeq \frac{1}{2}R^2$ (table 2.3), so $QR \gg 1$ given $QR_g \gg 1$. It follows from equation 2.25 that in the region of its applicability the disc thickness can be determined by plotting $\log(Q^2 I(Q))$ versus Q^2; the slope of the linear part of this plot is $-\frac{1}{3}H^2$. We demonstrate in the next section that the calculations of F(Q) for flat cylinders and flat parallelepipeds (slabs) of the same thickness and volume lead to indistinguishable results. Therefore, it is reasonable to expect that the limiting behaviour expressed in equation 2.25 would apply to any flat particle of roughly regular shape.

2.2 The form factor for simple geometrical shapes

In the course of this work we have modelled the X-ray and neutron scattering in paraffinic systems using simple geometrical representation for the individual molecules of n-alkanes (either thin rods or thin slabs), flat aggregates of these molecules (flat slabs or discs) and for the paraffin-polymer aggregates (spheres). In order to respects the steric constraints imposed by the chemical composition of the solutions studied we have used polydisperse distributions whenever necessary. Below we list the formulae used and give a brief discussion of the slab geometry, which has been used less extensively in previous studies than the other geometries. A comprehensive discussion of the analytical expressions for F(Q) is given in [33].

- Cylinders of radius R and height $2H$:

$$F(Q) = 2\pi R^2 H \int_0^{\frac{\pi}{2}} \frac{\sin^2(QH\cos\alpha)}{(QH\cos\alpha)^2}\frac{4J_1^2(QR\sin\alpha)}{(QR\sin\alpha)^2}\sin\alpha d\alpha \tag{2.27}$$

- Spheres of radius R:

$$F(Q) = \mathcal{V}\left[3\frac{\sin(QR) - QR\cos(QR)}{(QR)^3}\right]^2 \tag{2.28}$$

- Parallelepipeds of edges $A \leq B \leq C$, where $\frac{A}{B} = a$, $\frac{C}{B} = c$ and $QB = \mathcal{B}$ [39]:

$$F(\mathcal{B}, a, c) = \int_0^1 F_k(\mathcal{B}(1-x^2)^{\frac{1}{2}}, a)\left[\frac{\sin(\frac{\mathcal{B}cx}{2})}{\frac{\mathcal{B}cx}{2}}\right]^2 dx \tag{2.29}$$

where

$$F_k(\mathcal{B},a)=\int_0^1\left[\frac{\sin\left[\frac{\mathcal{B}}{2}\cos(\frac{\pi}{2}u)\right]\sin\left[\frac{\mathcal{B}a}{2}\sin(\frac{\pi}{2}u)\right]}{\frac{\mathcal{B}}{2}\cos(\frac{\pi}{2}u)\frac{\mathcal{B}a}{2}\sin(\frac{\pi}{2}u)^2}\right]^2 du \qquad (2.30)$$

- In case of polydyspersity F(Q) has the general form:

$$F(Q)=\sum_{y_{min}}^{y_{max}}\Phi_1(y)(1-\Phi_1(y))F(Q,y) \qquad (2.31)$$

where y is the geometrical parameter of the polydisperse distribution and $\Phi_1(y)$ is the volume fraction of particles with dimension y.

Apart from the polydispersity resulting from the imposed n-alkane molecular chain length distribution we have used two analytical distributions: Normal and lognormal. The corresponding formulae are:

- The Normal distribution:

$$f(x)=\frac{1}{\sqrt{2\pi}\sigma}\exp\left[-\frac{1}{2}(\frac{x-x_0}{\sigma})^2\right] \qquad (2.32)$$

- The lognormal distribution:

$$f(x)=\frac{1}{\sqrt{2\pi}\sigma x}\exp\left[-\frac{1}{2}(\frac{\ln x-\ln x_0}{\sigma})^2\right] \qquad (2.33)$$

Scattering from flat parallelepipeds (slabs) is shown in figure 2.3. In all three cases the slabs have thickness 5 Å. The curves were computed using the lognormal size distribution (equation 2.33) with a small value of σ. For larger aspects ratios the scattering curve becomes less steep, but the overall change is not very pronounced. Figure 2.4 shows a comparison of differential cross sections for monodisperse flat slabs and discs of the same thickness 5 Å and same volume. The slab base is 20 Å × 20 Å and the disc radius is 11.3 Å. F(Q) for slabs and discs was calculated using formula 2.29 and 2.27, respectively. The accuracy of our calculations for slabs was cross-checked by computing F(Q) directly using the Debye formula 2.11 and no differences were found. It is apparent that there is no experimentally distinguishable difference between the scattering from the system of slabs and discs.

The character of the lognormal distribution (2.33) is illustrated in figure 2.5 for three different values of parameter σ. These particular distributions have been used to calculate the F(Q) curves for polydisperse discs and slabs (figures 2.6 and 2.7, respectively).

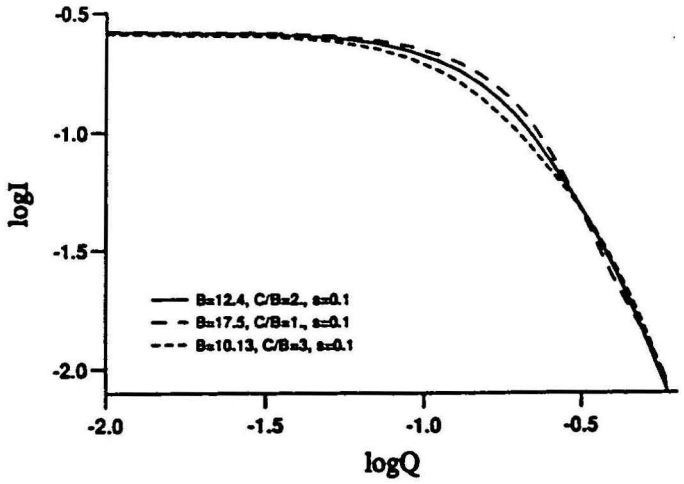

Figure 2.3: Scattering from monodisperse flat slabs of different aspect ratios. In all three cases the slabs have thickness 5 Å. The aspect ratios ($\frac{C}{B}$) are 1 (broken line), 2 (solid line) and 3 (dense broken line)

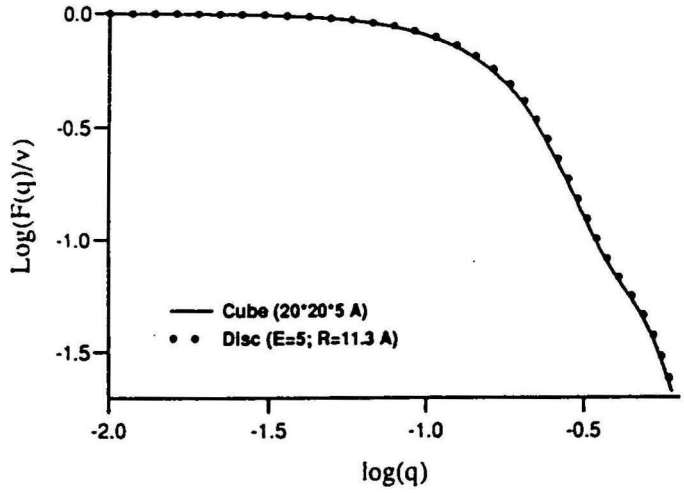

Figure 2.4: The comparison of differential cross sections for monodisperse flat slabs and discs of thickness 5 Å and same volume. For explanation see text.

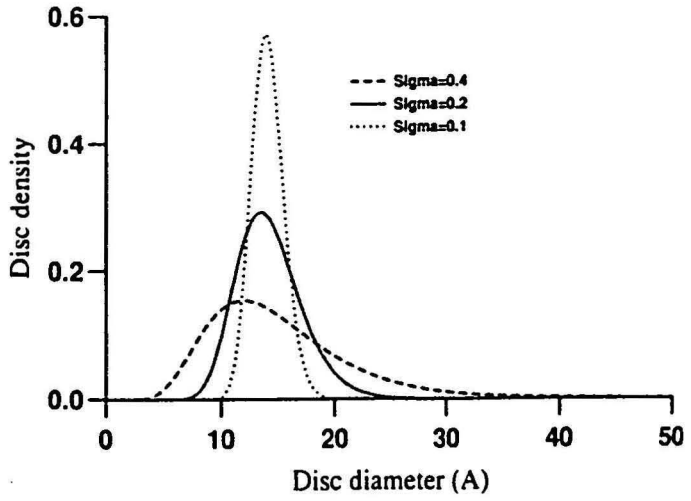

Figure 2.5: Lognormal distribution centered at 14 Å.

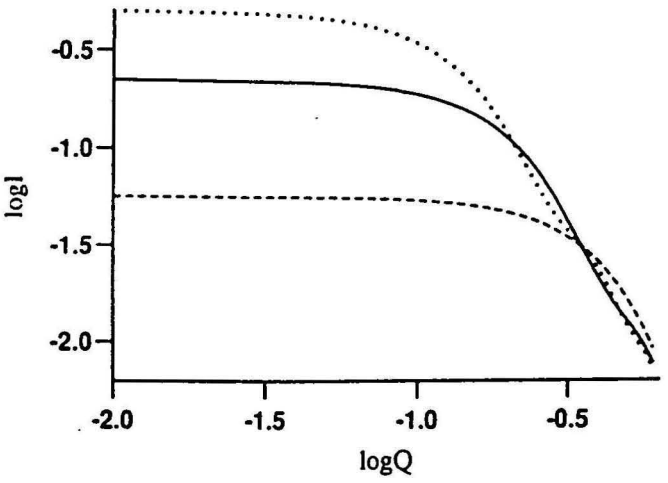

Figure 2.6: Scattering from polydisperse flat discs 5 Å thick. The distribution of disc diameter is centered at 14 Å. The values of parameter σ are 0.1 (dotted line), 0.2 (solid line) and 0.4 (broken line).

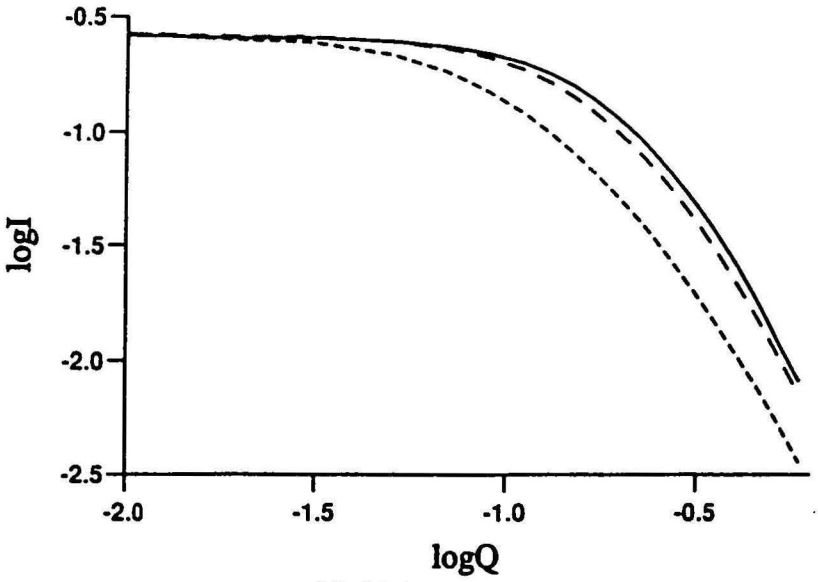

Figure 2.7: Normalised scattering from polydisperse flat slabs: C/B= 2, B= 12.4 Å. The values of parameter σ are 0.4 (solid line), 0.2 (broken line) and 0.1 (dense broken line).

For polydisperse discs (figure 2.6), the scattering curve for $\sigma = 0.1$ is similar to that computed for a monodisperse distribution of discs. After normalisation at $Q = 0$ the curves become progressively flatter as polydispersity increases (compare with figure 2.7). As it is illustrated in figure 2.8, truncation of a log-Normal distribution of discs at a small value below the peak affects the scattering cross section only in a minor way.

The system of thin slabs (or rectangular thin plates) used by us has a polydisperse distribution of the longest edge, C (figure 2.7). However, the distribution of C-sizes has been cut off to comply with the requirement $B \leq C$ for which the equation is valid. The F(Q) curves shown in figure 2.7 have been normalised at $Q = 0$; the three distributions of C are like in figure 2.5, with $\frac{C_0}{B} = 2$ and $B = 12.4$ Å. Like for the discs, the increased polydispersity of slabs results in a flatter scattering curve.

2.2.1 Large-Q limit in the small-Q range: the Porod region

The large-Q limit of the small angle domain is the region where the atomic resolution has not been yet achieved, but the observation scale is small and a well-defined interface appears to be smooth. This is the so-called Porod region. In this limit, the differential scattering cross section for a two-phase system with sharp interface is [40]:

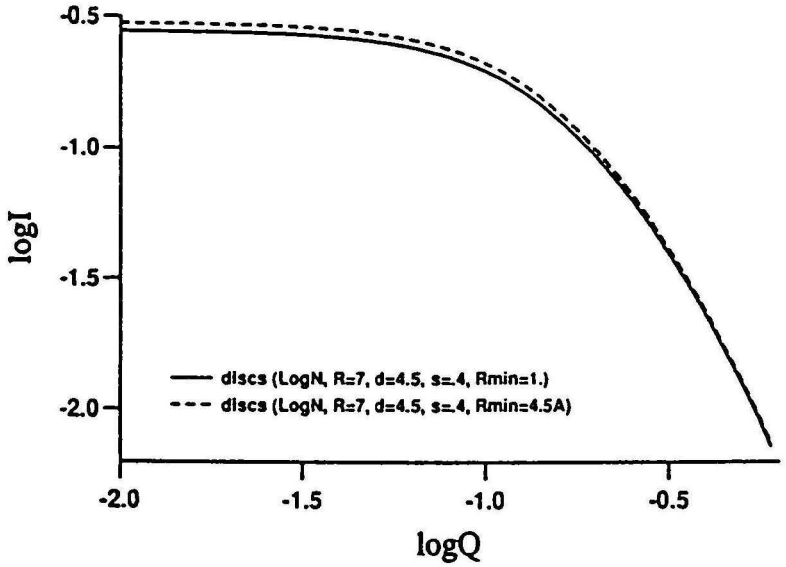

Figure 2.8: Comparison of scattering from two log-Normal distributions of 4.5 Å thick flat discs: full (broken line) and truncated at $\rho = 4.5$ Å (solid line). The values of parameters are $\rho = 7$ Å, $\sigma = 0.4$.

$$\frac{d\sigma}{d\Omega}(Q) = 2\pi C_0(\rho_1 - \rho_2)^2 Q^{-4}\frac{S}{V} \tag{2.34}$$

where S is the total area of interface inside the scattering volume V. The specific surface area, $\frac{S}{V}$, can be expressed in a different form:

$$\frac{S}{V} = \frac{\pi\Phi_1(1-\Phi_1)\left[\lim_{Q\to large\ value}(Q^4\frac{d\sigma}{d\Omega}(Q)\right]}{\mathcal{I}} \tag{2.35}$$

where $\mathcal{I}$ is the invariant of the system defined as:

$$\mathcal{I} = \int_0^\infty Q^2\frac{d\sigma}{d\Omega}(Q)dQ = 2\pi^2 C_0(\rho_1 - \rho_2)^2\Phi_1(1-\Phi_1) \tag{2.36}$$

Equation 2.34 predicts the classical Q^{-4} behaviour of the scattering cross section in the large-Q limit of the small angle region. This result is explicitly dependent on the assumption of existence of a sharp and smooth interface region. If the interface geometry is different, for instance fractal or subfractal (that is rough), the exponent may vary from the Porod result of -4 [41].

2.3 Experimental procedures

2.3.1 Absolute measurements of SAXS and SANS

For small angle scattering, the experimentally registered signal is the number of counts $I(\Theta)$, which is proportional to the number of neutrons or photons scattered by the sample of surface area A and thickness t per unit time and registered by a detector element positioned at angle Θ from the direction of the incident beam. Quantitatively, this is expressed as:

$$I = I_0 A t T \frac{d\sigma}{d\Omega} d\Omega E(\Theta, \lambda) + background \tag{2.37}$$

where λ is the neutron or photon wavelength, T is sample transmission, I_0 is the incident beam intensity and $E(\Theta, \lambda)$ is the quantum efficiency of the detector array. In equation 2.37 I_0 and $E(\Theta, \lambda)$ are characteristics of the experimental system and $d\Omega$ can be determined from the experiment geometry, whereas A, t, T and $\frac{d\sigma}{d\Omega}$ are sample-dependent. Therefore, in order to calculate $\frac{d\sigma}{d\Omega}$ from the experimentally measured $I(\Theta)$ one also has to measure the following quantities:

- sample surface area A
- sample thickness t
- sample transmission T
- incident flux I_0
- detector efficiency $E(\Theta, \lambda)$
- sample-independent scattering background (due to electronic noise, cosmic radiation, etc.)

The last four measurements are performed routinely for each experimental configuration (i.e. each combination of the sample-detector distance and the neutron or X-ray wavelength λ). For the measurements of I_0 and T attenuating filters are used. $E(\Theta, \lambda)$ is determined using one-millimetre thick water sample as a Q-independent scattering standard of known absolute cross section. The background is determined by counting while the beam is blocked. For liquid samples, the scattering of empty container is measured and subtracted from the data. The calculations of $\frac{d\sigma}{d\Omega}$ are performed using custom written computer programs.

2.3.2 Incoherent scattering on hydrogen atoms: blanks

For a set of N identical nuclei the neutron scattering cross section is given by:

$$\frac{d\sigma}{d\Omega}(Q) = \langle \sum_i^N \sum_j^N b_i b_j \exp(i\mathbf{Q}(\mathbf{r}_i - \mathbf{r}_j)) \rangle \tag{2.38}$$

where $\mathbf{r}_i$ is the position of nucleus i. The average is taken over the different isotopes and possible orientations of the nuclear spin. The latter procedure is necessary since neutrons have a non-zero nuclear spin: $I = \frac{1}{2}$. The net result is:

$$\frac{d\sigma}{d\Omega}(Q) = \sum_i^N \sum_j^N \langle b_i \rangle \langle b_j \rangle \langle \exp(i\mathbf{Q}(\mathbf{r}_i - \mathbf{r}_j)) \rangle + \sum_i^N (\langle b_i^2 \rangle - \langle b_j \rangle^2) \tag{2.39}$$

The first term in 2.39 is the Q-dependent coherent scattering that carries the structural information about the system, whereas the latter term describes the Q-independent incoherent scattering. The incoherent scattering is isotropic in the solid angle 4π and for majority of nuclei it is small compared to the coherent term. An important exception is the hydrogen nucleus ($I = \frac{1}{2}$), for which the total coherent cross section is $\sigma_{coh} = 2 \times 10^{-24}$ cm^2 and the incoherent one is $\sigma_{incoh} = 79 \times 10^{-24}$ cm^2. Therefore, for systems containing large concentrations of hydrogen atoms the incoherent background is large. For X-ray scattering the incoherent background is very weak and can be neglected.

The value of $\sigma_{incoh} = 79 \times 10^{-24}$ cm^2 is strictly correct only for dilute systems. In concentrated systems, because of the multiple scattering σ_{incoh} depends both on the neutron wavelength and sample geometry [42]. Therefore, the best practical way to deal with the problem is to directly measure the incoherent background on a blank sample (i.e. sample with no Q-dependent scattering component) and subtract it from the data.

Blanks are prepared by substituting part of the deuterated solvent with protonated solvent in such proportion that the incoherent scattering of the original sample is matched by the total scattering of the blank. The incoherent background of the original sample is:

$$\frac{d\sigma^{inc}}{d\Omega} = \Phi \frac{N_A n^H}{v_m} \frac{\sigma_{inc}^H}{4\pi} \tag{2.40}$$

whereas the total scattering of a blank has the form:

$$\frac{d\sigma_{blank}}{d\Omega} = \frac{d\sigma_{blank}^{coh}}{d\Omega} + \frac{d\sigma_{blank}^{incoh}}{d\Omega} = \Phi_H(1-\Phi_H)\left(\frac{N_A b_H}{v_m^H} - \frac{N_A b_D}{v_m^D}\right)^2 \frac{v^H}{N_A} + \Phi_H \frac{N_A n_{blank}^H}{v_m^H} \frac{\sigma_{inc}^H}{4\pi} \tag{2.41}$$

In equation 2.40, Φ is the volume fraction of the protonated solvent, v_m is its molar volume, $N_A n^H$ is the number of protons in one mole of solute, N_A is

Avogadro number and σ_{inc}^{H} is the proton incoherent cross section. The factor of 4π comes from the integration over the solid angle. The meaning of symbols in equation 2.41 is similar; indices H and D refer to the protonated and deuterated solvent, respectively. The coherent term has a form like in equation 2.14. Since the solvent particles are very small, the Guinier region extends to large Q-values and the form 2.19 can be used, where $\mathcal{V} = \frac{v_H}{N_A}$ is the volume of a single solvent molecule. The incoherent term is fully analoguous to equation 2.40, except instead of the protonated solute one is using the protonated solvent.

The volume fraction Φ_H of the protonated solvent to be used in the blank can be found from the requirement that $\frac{d\sigma^{inc}}{d\Omega} = \frac{d\sigma_{blank}}{d\Omega}$. For the practical purposes, however, for both the toluene and nitrobenzene solvent used in this work the coherent term in equation 2.41 does not exceed one percent of the corresponding incoherent scattering. Therefore, since $\frac{N_A n^H}{v_m}$ is the number of hydrogen atoms per unit volume, blanks can by prepared simply by chosing the volume concentration of hydrogen atoms in blanks the same as in the original sample.

We have prepared blanks for a number of solutions of mixture A (for definition of mixture A see Chapter 3) in deuterated toluene and deuterated nitrobenzene (table 2.4). It is well known that scattering of blanks often scales with transmission [42]. In the following three figures we test this property for the dilute nitrobenzene blanks (figure 2.9), dilute toluene blanks (figure 2.10) and concentrated toluene blanks (figure 2.11). It is clear that the incoherent scattering intensity scales well with transmission for the dilute blanks of both solvents, but not for the concentrated blanks. This is probably caused by the wavelength-dependence of the multiple scattering, which is particularly accentuated for the hydrogen-rich samples.

2.3.3 Contrast data for SANS and SAXS: selection of solvents

Organic solvents used for preparing model fuels should resemble as closely as possible the natural solvent, but also have to exhibit reasonable neutron and X-ray contrast with paraffins and be transparent for both types of radiation. Toluene is widely used in industrial studies of crude oils and their derivatives and, therefore, it is a necessary choice of solvent. Protonated toluene shows very little neutron or X-ray contrast with paraffins. By deuterating toluene a satisfactory contrast for neutrons can be achieved, as calculated using table 2.2 and equation 2.6. A similar effect is observed for nitrobenzene (figure 2.12).

For a classical X-ray source with a copper cathode no contrast-enhancement techniques are available and the paraffin solutions in toluene scatter too weakly to be measured. Using equation 2.7 we have calculated the X-ray scattering length density (the product $I_e\rho_e$) for several organic solvents. As the proportion of heavy atoms in the solvent increases, the contrast with the paraffins becomes

Table 2.4: Transmission and incoherent cross section measured for blanks used in this study. D-nb is deuterated nitrobenzene and D-tol is deuterated toluene. Values in the headings of columns 3 to 8 correspond to the neutron wavelength (in Å), followed by the sample-detector distance (in metres). Different combinations of these values correspond to different Q-ranges.

Blank for sample	t mm	Transmission			$\frac{d\sigma_{blank}}{d\Omega}$ (cm^{-1})		
		4Å,1.3m	6Å,1.9m	12Å,4.3m	4Å,1.3m	6Å,1.9m	12Å,4.3m
5%A:D-nb	2		0.753	0.742		0.168	0.183
10%A:D-nb	2		0.745	0.739		0.179	0.193
15%A:D-nb	2		0.710	0.688		0.229	0.251
20%A:D-nb	2		0.691	0.659		0.269	0.301
5%A:D-tol	2		0.783	0.776		0.137	0.15
10%A:D-tol	2		0.726	0.6832		0.236	0.290
15%A:D-tol	2		0.693	0.6287		0.309	0.38
20%A:D-tol	2		0.657	0.576		0.380	0.520
40%A:D-tol	1	0.747	0.717		0.497	0.345	
60%A: D-tol	1	0.708	0.666		0.608	0.417	
80%A:D-tol	1	0.672	0.627		0.675	0.468	

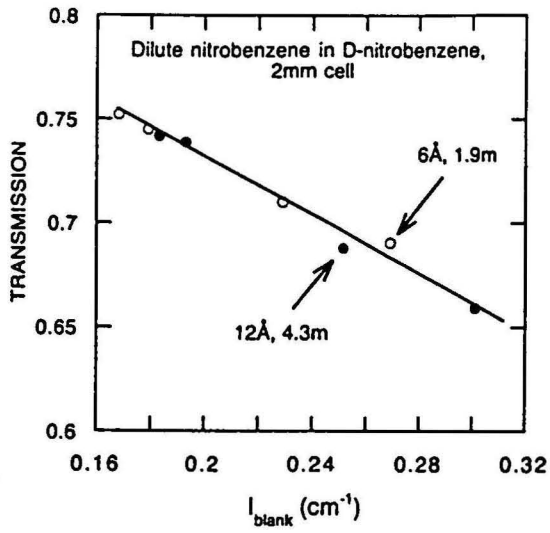

Figure 2.9: Correlation between the transmission and scattering intensity for blanks corresponding to concentrations 5, 10, 15 and 20% of mixture A in deuterated nitrobenzene. Cell thickness is 2 mm.

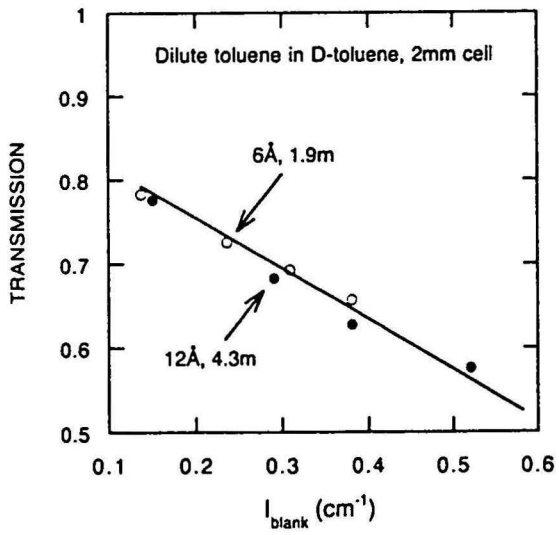

Figure 2.10: Correlation between the transmission and scattering intensity for blanks corresponding to concentrations 5, 10, 15 and 20% of mixture A in deuterated toluene. Cell thickness is 2 mm.

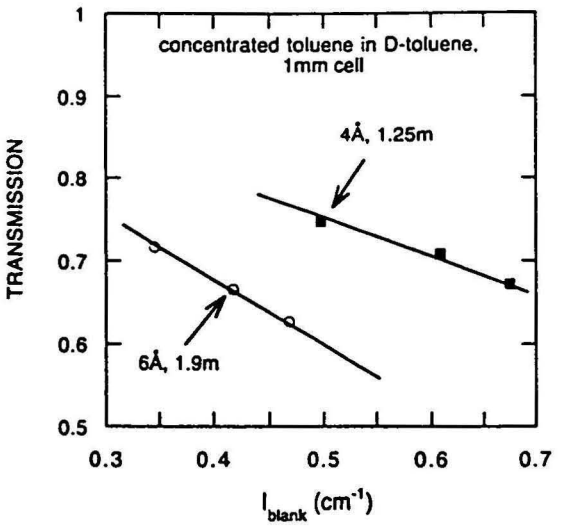

Figure 2.11: Correlation between the transmission and scattering intensity for blanks corresponding to concentrations 40%, 60% and 80% of mixture A in deuterated toluene. Cell thickness is 1 mm.

more and more pronounced (figure 2.13). However, this is countered by the decreasing X-ray transparency of the solvent, as illustrated in figure 2.14. As the thickness of glass capillaries used for X-ray scattering experiments is about 1 mm, the experimental upper limit for the solvent absorption coefficient is about 10 cm^{-1}. The only solvent that offers a reasonable compromise between the contrast and transparency is nitrobenzene and, therefore, it has been selected for X-ray studies.

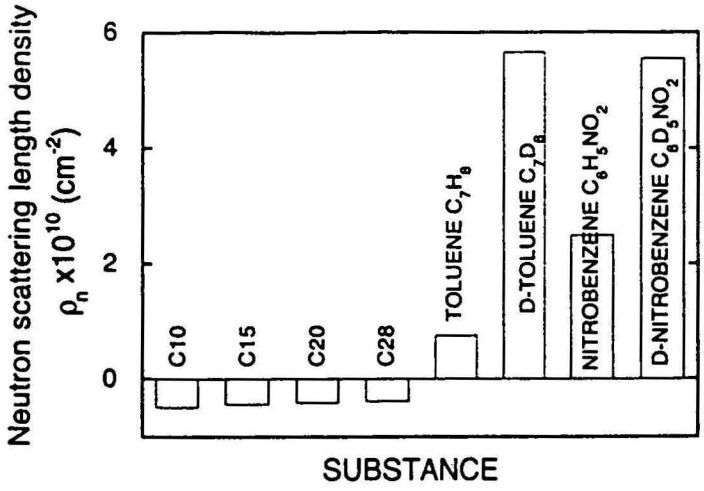

Figure 2.12: Calculated neutron scattering length density, ρ_n, for n-alkanes in the range C10 - C28, and the protonated and deuterated toluene and nitrobenzene.

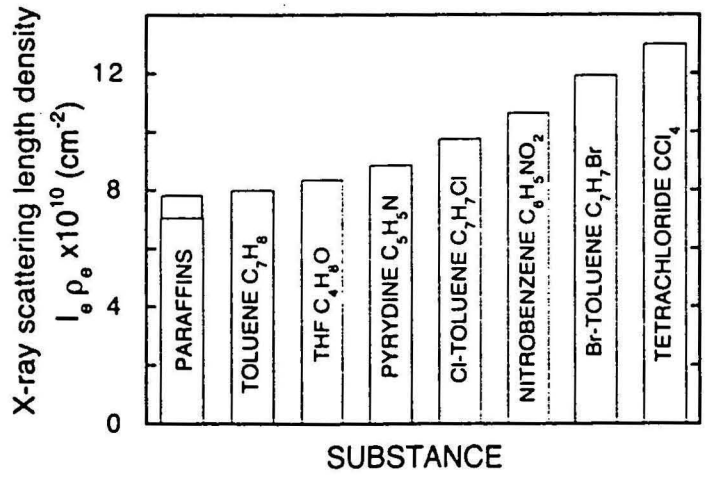

Figure 2.13: Calculated X-ray scattering length density (the product $I_e\rho_e$) for paraffins and various organic solvents. The range for paraffins corresponds to various components of mixture A, where heavier paraffins scatter more strongly than the light ones.

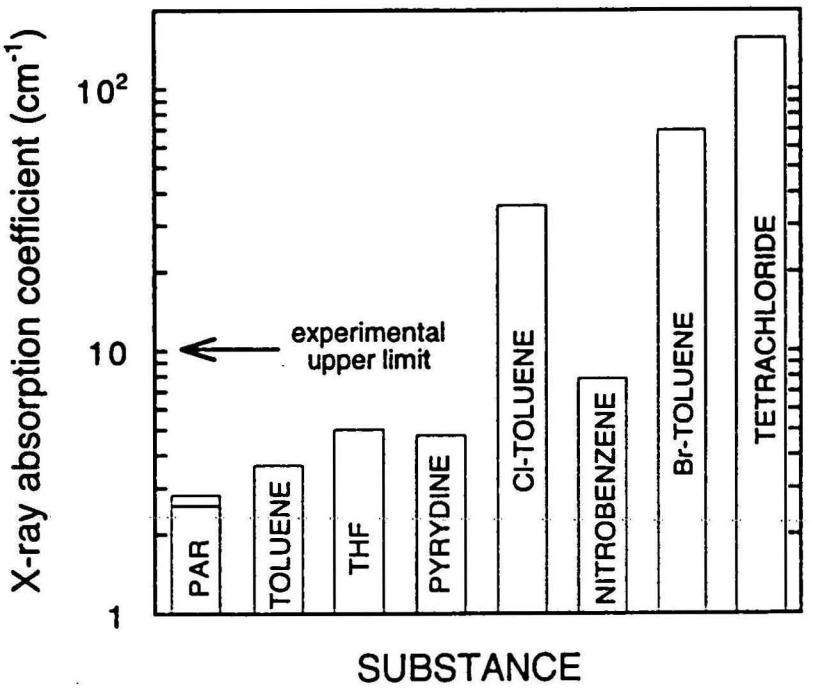

Figure 2.14: Calculated X-ray absorption coefficient for paraffins and various organic solvents. The range for paraffins corresponds to various components of mixture A, where heavier paraffins absorb X-rays more strongly than the light ones.

Chapter 3

Small Angle X-ray Scattering in model fuels

3.1 Real and model diesel fuels

Diesel fuels are middle distillates of crude oils. Typical diesel fuel contains up to 30% of broadly distributed paraffins (mostly n-alkanes) dissolved in a mixture of aromatic solvents. Normal alkanes are the least soluble components of fuels and are responsible for fuel solidification at low temperatures. The solidification is a complex, gradual process occuring over a temperature range of at least several degrees centigrade. In this chapter we discuss the structural aspects of fuel solidification at the molecular level. Major experimental tools used to gain insight into the microstructure of fuels are SAXS and SANS.

Real diesel fuel is a mixture of hundreds of aliphatic and aromatic compounds. Such complexity allows little control over its composition and makes the experimental results system specific. Figure 3.1 shows the n-alkane distribution for one of industrial diesel fuels, Fuel A. We have used this distribution to prepare a similar mixture of n-alkanes called throughout this report mixture A. Various amounts of mixture A were then dissolved in toluene and nitrobenzene. These model fuels are still quite complex (they contain 20-odd different chemical compounds), but they are well-defined chemically. Also, they contain all the major components responsible for fuel solidification.

Furthermore, a number of solutions of various single n-alkanes in nitrobenzene and toluene were investigated. These model fuels are quite simple, but they have provided important microstructural insights which we have applied to the analysis of more complex systems.

As discussed previously, the scattering cross section for X-rays depends on the electronic density contrast in the scattering medium and on the geometry of scattering particles. Table 3.1 contains data needed for calculations of the

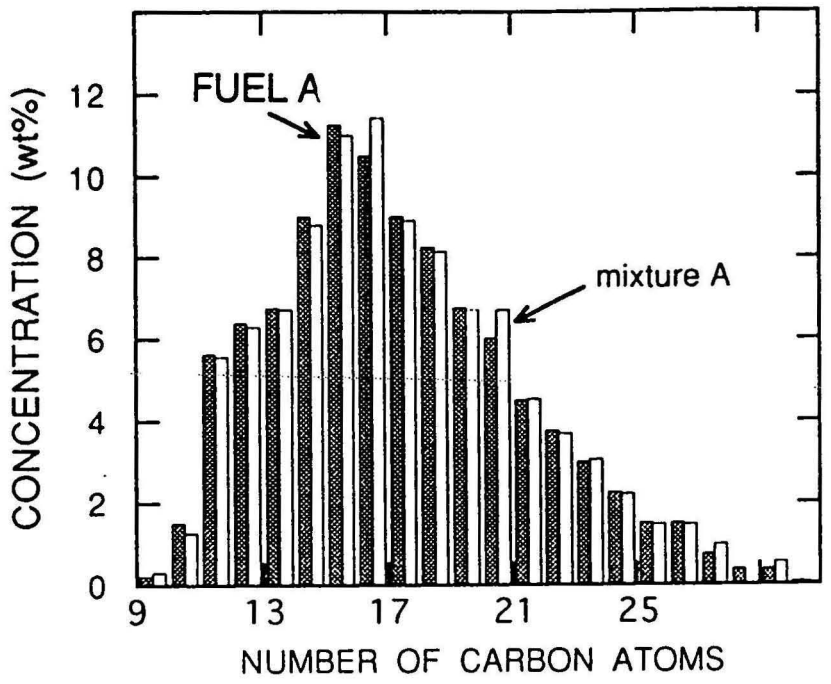

Figure 3.1: Distribution of normal alkanes in Fuel A diesel fuel and in mixture A.

small angle X-ray scattering by n-alkane solutions in toluene and nitrobenzene. This information has been used to obtain the theoretical fits presented in this chapter.

By comparing columns 3 and 4 of table 3.1 one notices increasing discrepancy between the end-to-end molecular distances for n-alkanes in solid and liquid phase. In solid phase, the n-alkane molecules are arranged in a crystalline order in all-trans configuration, which results in the maximum possible end-to-end distances. In contrast to this, the molecules in liquid phase are free to assume a number of statistically-allowed conformations. Since the statistical segment length in n-alkanes corresponds to about eigth carbon-carbon distances, for very light paraffins the end-to-end distances in the liquid phase do not differ much from their solid-state counterparts. As the paraffin chain becomes longer, however, the molecular coiling-up becomes more and more important, the end-to-end distances shorten compared to the crystalline values and the liquid paraffins behave very much polymer-like. Normal alkanes containing more than about 100 carbon atoms are usually referred to as polyethylene.

3.2 Solutions of pure n-alkanes in nitrobenzene

Since both the electronic density and geometrical shape of at least lighter paraffins (which do not exhibit pronounced conformational effects) in good solvents are well established, their small angle scattering cross section can be calculated exactly. This can be done in a number of ways: either directly from formula 2.11, or from equation 2.27 or 2.29. In practice, one should allow for some discrepancy between the measured and calculated absolute scattering intensity. This may be caused by systematic errors in the calibration of the experimental arrangement as well as by a possible small departure of the molecular geometry in solution from the expected n-alkane molecular shape and size. Based on our experience, the discrepancy should not exceed a factor of 2 and in majority of cases is much closer to unity.

In order to gain insight into the behaviour of paraffins in solution for simplest possible systems, a number of 20 *vol*% nitrobenzene solutions of n-alkanes ranging from C11 to C29 were examined by SAXS. Some of the representative experimental results are shown in figures 3.2, 3.3, 3.4, 3.5 and 3.6. Although data were acquired in a wide range of temperatures above T_c, for none of the solutions neither the observed SAXS Q-dependence nor its intensity could be ascribed solely to isolated paraffin molecules (monomers). In general, the scattering intensity was several times larger than expected, thus indicating a presence of certain number of paraffin aggregates in solution.

Some clues about the size and shape of aggregates can be gained from the analysis of experimental data in the small-Q and large-Q limit. The structural model can be then refined by fitting to the entire set of experimental points.

Firstly, it is evident that the individual aggregates may only contain small

Table 3.1: Electronic density and geometrical data for n-alkane molecules. The end-to-end distances in the liquid phase have been determined by Brady and coworkers [57]. The solid phase data have been compiled from the reviews by Turner [2] and Small [3]. The steric thickness of n-alkane molecule is about 4.5 Å. TOL - toluene, NB - nitrobenzene.

molecular properties				molar mass (g/mole)	density (g/cm^3)	% of molecules in mix A
No of carbon atoms	No of electrons	end-to-end dist (Å)				
		solid	liquid			
8	66	8.9	9.4	114	0.702	0.59
9	74	10.05		128	0.718	2.11
10	82	11.42	11.2	142	0.730	8.28
11	90	12.70		156	0.740	8.53
12	98	13.95	12.6	170	0.749	8.37
13	106	15.22		184	0.756	10.14
14	114	16.49	14.4	198	0.763	11.79
15	122	17.75		212	0.768	11.43
16	130	19.02	16.0	226	0.773	8.37
17	138	20.29		240	0.778	7.20
18	146	21.56	17.8	254	0.777	5.60
19	154	25.36		268	0.785	5.30
20	162	26.64	19.5	282	0.789	3.40
21	170	27.90		296	0.792	2.65
22	178	29.17	20.3	310	0.794	2.09
23	186	30.44		324	0.797	1.45
24	194	31.71		338	0.799	0.93
25	202	33.0		352		0.89
26	210	34.24		366	0.803	0.57
27	218			380	0.805	0
28	226	36.80		394	0.807	0.311
29	234	38.05		408	0.808	0.036
TOL	50			92	0.867	
NB	64			123	1.204	

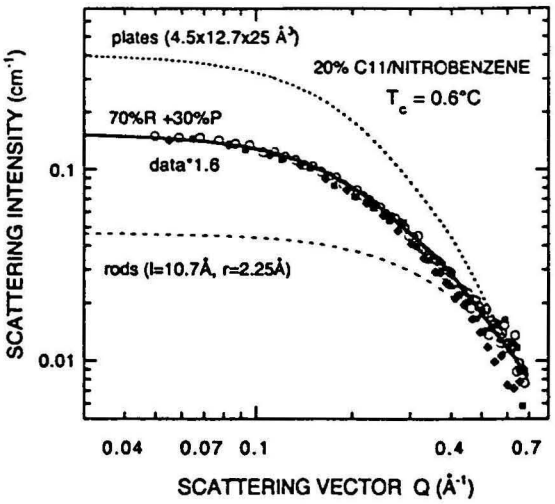

Figure 3.2: SAXS data for a 20% solution of C11 in nitrobenzene at three temperatures: 23°C (circles), 32°C (squares) and 50°C (diamonds). The temperature of crystallisation for this solution is 0.6°C. The origin of fitting lines for rods and plates (AR= 2) is described in detail in the text.

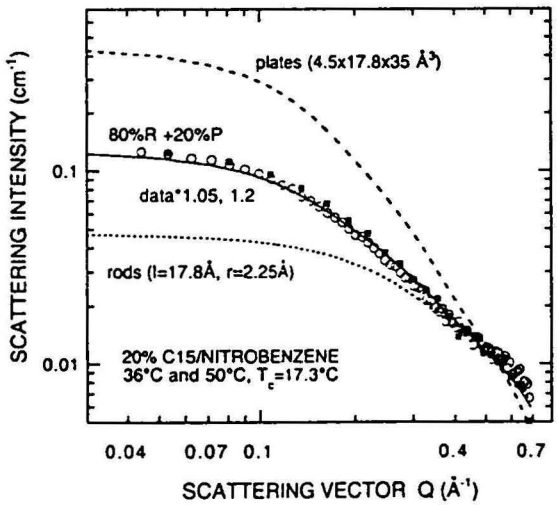

Figure 3.3: SAXS data for a 20% solution of C15 in nitrobenzene at two temperatures: 36°C (circles) and 50°C (squares). The temperature of crystallisation for this solution is 17.3°C. The origin of fitting lines for rods and plates (AR= 2) is described in detail in the text.

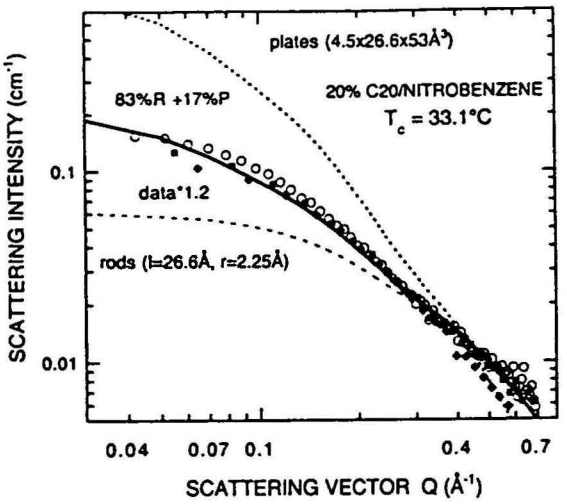

Figure 3.4: SAXS data for a 20% solution of C20 in nitrobenzene at three temperatures: 36°C (circles), 50°C (squares) and 65°C (diamonds). The temperature of crystallisation for this solution is 33.1°C. The origin of fitting lines for rods and plates (AR= 2) is described in detail in the text.

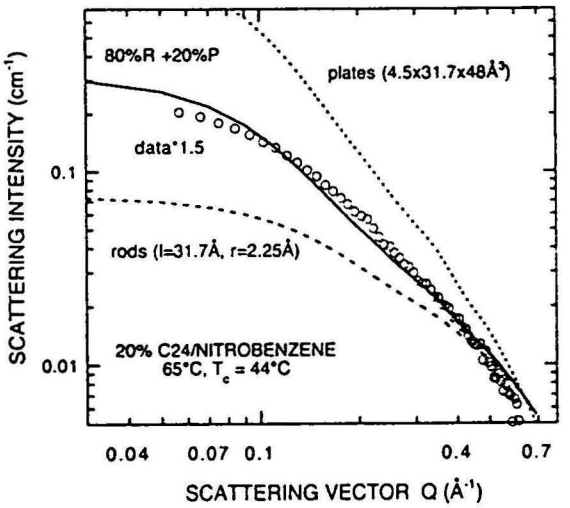

Figure 3.5: SAXS data for a 20% solution of C24 in nitrobenzene at 65°C. The temperature of crystallisation for this solution is 44°C. The origin of fitting lines for rods and plates (AR= 1.5) is described in detail in the text.

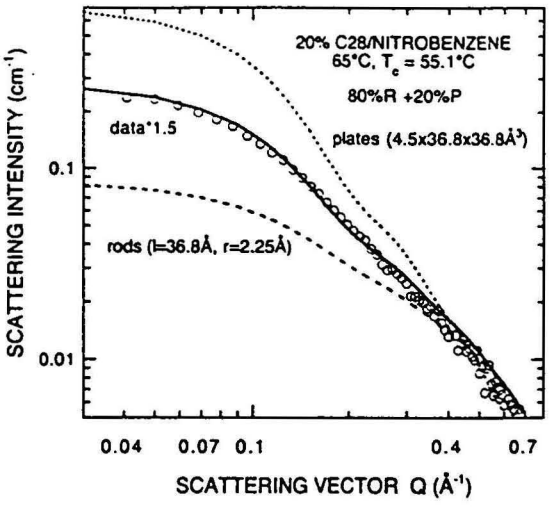

Figure 3.6: SAXS data for a 20% solution of C28 in nitrobenzene at 65°C. The temperature of crystallisation for this solution is 55.1°C. The origin of fitting lines for rods and plates (AR= 1) is described in detail in the text.

number of paraffin molecules since the departure of experimental data from the theoretical curve calculated for monomers extends to the large-Q region. We have calculated the intensity of small angle scattering for the system of n-alkane monomers in nitrobenzene for every type of n-alkane according to equation 2.27 assuming that the molecules are of cylindrical shape (rods). The lengths and radii of these rods reflect the molecular geometry of n-alkanes (table 3.1) and are given in the corresponding figures. Furthermore, we have verified that numerically identical results are obtained using equation 2.29, which assumes that single scatterer is a parallelepiped, using the same length and volume of the scattering particle as for the rods. Therefore, it appears that the scattering curve is not very sensitive to the fine detail of the scatterer's shape. This is an important finding which gives us confidence that the scattering from a zig-zag-shaped all-trans n-alkane molecule can be well approximated by scattering from a simpler geometrical object: rod or parallelepiped.

Secondly, it follows from equation 2.25 that the thickness H of a flat aggregate can be determined by plotting $\log(Q^2 I(Q))$ versus Q^2: the slope of the linear part of this plot is $-\frac{1}{3}H^2$. We have constructed these plots and have consistently obtained H about 5Å, independently of the number of carbon atoms in the aliphatic chain. (As discussed in the preceding chapter, one expects that the limiting behaviour expressed by equation 2.25 would apply to any flat particle of roughly regular shape.) Therefore, we conclude that n-alkanes aggregate by forming flat 'rafts' built of several monomers. This is consistent with the

measured scattering intensity extrapolated to $Q = 0$ being only several times larger than the theoretical result for rods, since according to equation 2.19 the scattering intensity at $Q = 0$ is proportional to $\mathcal{V}$, the number-average volume of single scattering object.

The above information about the structure of paraffin aggregates was incorporated into the final fitting procedure. It was assumed that the paraffin molecules exist in nitrobenzene solution in two forms: monomers and flat aggregates. The geometry of monomers is pre-determined by the n-alkane species present in the solution, and so is the length (measured along the axis of the aliphatic chains) and thickness of the aggregate. This simply follows from the fact that 5Å is very close to the n-alkane molecular thickness and it is rather hard to imagine that two paraffin molecules could aggregate in any other way than side-to-side. We assume a monodisperse distribution of the aggregate width (i.e. single aggregation number), which may be different for every species of n-alkane molecules. This leaves two unknown parameters: the aggregate width and the proportion of aggregated molecules in the solution. The aggregate width is determined by the aspect ratio, AR, by definition equal to the ratio of aggregate width to its length. The scattering curve for aggregates assumed to be ideal parallelepipeds (slabs) was computed using formula 2.29.

As an example, figure 3.7 shows the calculated scattering cross section for a 20% soluton of C28 in nitrobenzene, assuming various forms of aggregation for the n-alkane molecules: monomers or flat aggregates (plates) of various aspect ratios varying from 1 to 3. The results of calculations are expressed in absolute units. As expected, in the large-Q limit the data for aggregates fall on a single line whose slope depends only on the aggregate thickness. In the small-Q limit the scattering intensity increases with the volume of single aggregate particle. We have performed similar computations for other n-alkanes present in mixture A.

As can be seen from figures 3.2, 3.3, 3.4, 3.5 and 3.6, reasonable fits can be obtained along the lines of our structural model for the entire range of paraffins. Numerical values characterising the fitted curves (e.g. 80%R + 20%P) refer to the distribution of the scattering intensity between the two species, R(ods) and P(lates), and the proportion of the aggregated n-alkane molecules can be calculated from these values. It turns out that up to about 30% of paraffin molecules can be contained in aggregates.

We observe a marked decrease of the aggregate aspect ratio from about 2 for light paraffins (up to C20) to about 1 for heavier paraffins. The reason of such behaviour is not clear, although it may be related to the increasing influence of conformational effects which are totally ignored in our model. Within the temperature range studied (from near T_c to about 50 degrees Centigrade above T_c) there may be a small temperature variation of the SAXS spectra. In this report we do not follow this issue in detail and for most n-alkanes we show in one plot curves taken at different temperatures and only one 'average' theoretical fit is displayed. For every case, however, fits were made to each individual

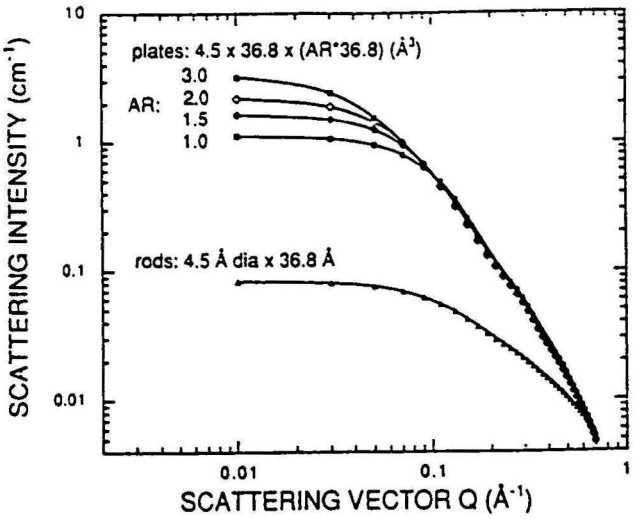

Figure 3.7: SAXS cross section for a 20% solution of C28 in nitrobenzene calculated for various forms of n-alkane aggregation. Rods represent monomers of C28. Plates represent 4.5Å thick aggregates of molecular length 36.8Å and various aspects ratios AR.

curve and it was usually possible to obtain marginally better results than these shown. As a rule, the differences between the best fitting parameters obtained for data collected at different temperatures were not large. The quality of fits could be probably further improved by allowing a polydisperse distribution of the aggregate size, but this would not alter our main conclusion: the coexistence of monomers and a significant number of aggregates.

The most significant result that follows from our analysis of SAXS data is that n-alkanes dissolved in nitrobenzene at temperatures near T_c form flat aggregates ('rafts') of several molecules. The width-to-length (aspect) ratio of these aggregates varies from 2 for light n-alkanes to 1 for these heavier than C24. These aggregates may exist even at temperatures 50°C above T_c. For 20 *vol%* solutions, the absolute volume fraction Φ_a of molecules bound in the aggregates varies from 0.03 to 0.06, which accounts for 15% to 30% of the total number of n-alkane molecules present in the solution. This phenomenon has not been previously reported and only a hint of a possibly related behaviour can be found in a series of papers by Brady and coworkers reporting on weak molecular alignment in liquid n-alkanes [58].

3.3 Solutions of mixture A in nitrobenzene

SAXS studies versus temperature were performed on three different solutions of mixture A in nitrobenzene: 10 *vol%*, 15 *vol%* and 20 *vol%* [1]. The most extensive set of data (temperature range −30°C to 70°C) was acquired for the 20% solution. In general, the scattering contrast between n-alkanes and nitrobenzene is weak. Long experimental runs of the order of 12 hours were necessary for the 20% solution in order to acquire good quality data. For less concentrated solutions the times were even longer, which limited the number of collected experimental data sets. Experiments at temperatures below 0°C were particularly difficult since there were problems with ice condensation on the capillary over the long time periods, even though an overpressured dry air sample environment was used in these cases.

The thermal evolution of SAXS spectra for the three solutions is shown in figures 3.8, 3.9 and 3.10. The crystallisation temperature T_c varies from 12.5°C to 17.8°C for these systems. No theoretical fits are shown for clarity; these are discussed in detail below in this section. It turns our that like for the solutions of single paraffins in nitrobenzene discussed in the previous section, the character of X-ray scattering is determined by contributions from monomers and aggregates. At high temperatures (50°C - 70°C) very few aggregates are present and the scattering is dominated by monomers. As the temperature drops to 20°C, the scattering intensity increases markedly and the scattering curves become steeper owing to paraffin aggregation. Using the $\log(Q^2 I(Q))$ versus Q^2 plot we have determined that the aggregates are flat objects about 5Å thick. This behaviour is analoguous to that found for the solutions of single n-alkanes in nitrobenzene.

At the temperatures below T_c the intensity of the broad scattering band decreases and at the same time a Bragg peak appears for the paraffin concentrations 20% and 15%. This effect is most pronounced for the former sample (figure 3.10), where the Bragg peak is observed at a Q value corresponding to the repeat distance in the crystalline state (related to the average paraffin chain length) $\frac{2\pi}{Q} = 30$ Å. As the temperature decreases further, the Bragg peak shifts towards the larger Q values which indicates gradual incorporation of lighter n-alkanes into the crystalline state. This process is studied in detail elsewhere in this report using gas chromatography. At the temperature −30°C the system is entirely solid and the repeat distance decreases to 21 Å. The broad band due to the monomer and aggregate scattering disappears, the intensity of the Bragg peaks markedly increases and the volume fraction of the crystalline phase becomes so large that one observes the onset of the Porod limit.

From the wide angle X-ray scattering results obtained in a similar temperature range (not discussed in this report) it is apparent, however, that only small proportion of the solidified fuel has crystallised. Majority of the solid phase

[1] A short account of results presented in this section has been contributed to the International Conference 'Horizons in Small Angle Scattering from Mesoscopic Systems' [59].

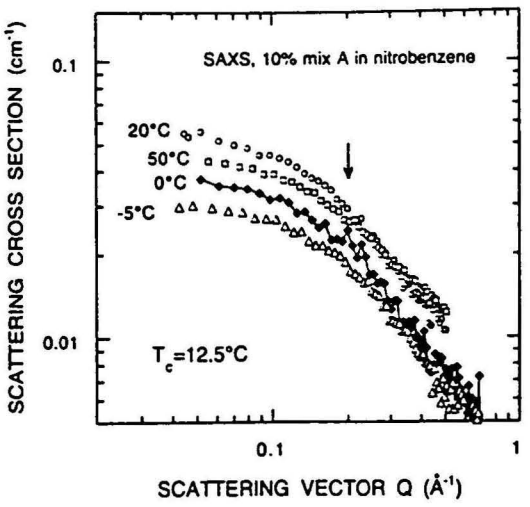

Figure 3.8: SAXS data for 10% solution of mixture A in nitrobenzene in the temperature range −5°C to 50°C.

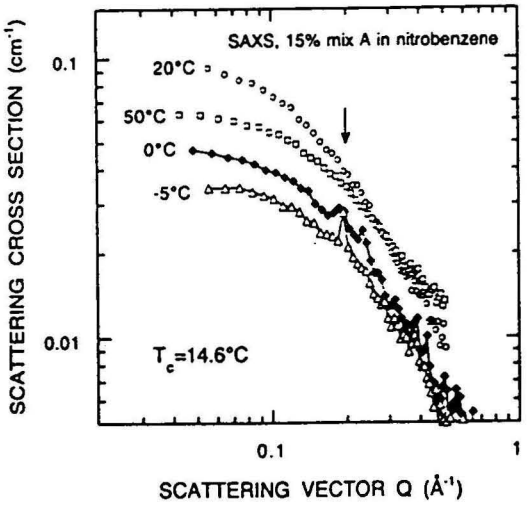

Figure 3.9: SAXS data for 15% solution of mixture A in nitrobenzene in the temperature range −5°C to 50°C.

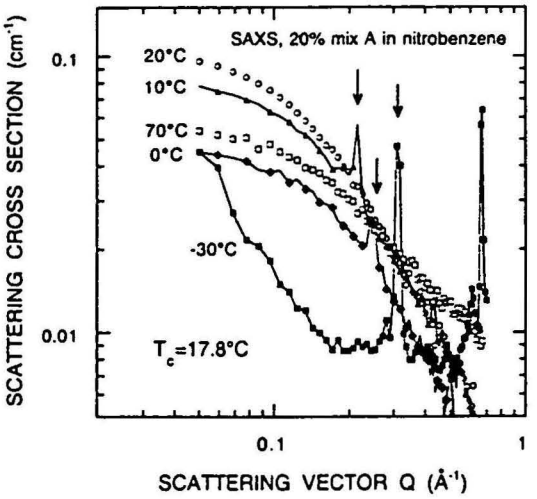

Figure 3.10: SAXS data for 20% solution of mixture A in nitrobenzene in the temperature range −30°C to 70°C.

remains in the amorphous state and only a small fraction of the randomly-oriented crystallites meet the Bragg condition for the one-dimensional detector under the experimental conditions used for SAXS measurements. Therefore, the intensity of Bragg peaks may be sample-dependent and may even change as the same sample is being thermally cycled around T_c and the crystallite orientation varies with each cycle. Therefore, the apparent lack of Bragg peaks in figure 3.8 does not necessarily mean that there is no crystalline phase in the 10% sample at the temperature −5°C. Indeed, two-dimensional detection is needed for this type of studies.

On the basis of the optical observations (discussed elsewhere in this report) it is known that the system becomes mechanically rigid (i.e. reaches its pour point) at the temperature 10°C. This happens by gelation and, consequently, large pockets of liquid remain in the bulk, as evidenced by the presence in the SAXS spectrum of a broad band in addition to the Bragg peaks. As the temperature drops, there is a selective transport of n-alkanes from the liquid phase to solid phase, which affects the SAXS characteristics of the liquid phase. All this has to be accounted for in the structural model used to fit the experimental data for the liquid phase.

Based on the above considerations as well as the results obtained for the solutions of single n-alkanes in nitrobenzene, we consider two general types of scattering objects in our structural model: monomers of n-alkanes and flat aggregates of n-alkanes. The monomers have a polydisperse size distribution which is fixed by the difference between the n-alkane content in mixture A

(which is known, see figure 3.1) and the n-alkane content in aggregates (which is to be determined). Since there are 21 n-alkanes present in the solution, the number of free parameters for a general fit would be excessive. In order to circumvent this problem we have initially assumed that (1) only like n-alkanes (i.e. these with the same number of carbon atoms) aggregate with each other and (2) the distribution of aggregates is a truncated lognormal (equation 2.33), with two free fitting parameters, σ and ρ_0. The shape (i.e. the aspect ratio) of the aggregates has to be determined as well.

Assumption (1) is consistent with the well-known chemical affinity and steric considerations for n-alkanes. Assumption (2) is far-reaching, though, and needs to be verified. It follows from the analysis presented in detail below that it is consistent with our SAXS data to conclude that at every temperature the concentration number of molecules bound in aggregates for each n-alkane is proportional to the total concentration number of molecules of this particular n-alkane present in the liquid phase, the proportionality factor being approximately the same for every n-alkane. As the n-alkane distribution in mixture A (figure 3.1) can be well approximated by a truncated lognormal, this conclusion is equivalent to the reduction of a 22-parameter fitting problem to a 3-parameter one, the extra parameter (in addition to σ and ρ_0) describing the aggregate geometry (for instance, the aspect ratio AR).

It has been shown in the previous chapter that no matter whether the scattering by monomers is computed using circular rods (equation 2.27) or square slabs (equation 2.29), the numerical data are identical provided these objects have same length and volume. This conclusion holds also for very short (or rather thin) rods and slabs. In other words, scattering by square aggregates (i.e. thin plates of aspect ratio 1) can be calculated exactly using the formula for thin rods (or rather discs) of the same thickness and volume. This substitution is advantageous in terms of the computing time, but the formula for slabs has to be used if aspects ratios different from unity are to be used.

Consider SAXS data presented in figures 3.12 and 3.13 for three mixture A concentrations (10%, 15% and 20%) at three temperatures above T_c (20°C, 50°C and 70°C). We have been able to fit all the experimental curves along the lines of our model assuming a truncated lognormal distribution ($\sigma = 0.4$, $\rho = 12.4$ Å) of square aggregates with aspect ratio equal to 1. The actual calculations were performed using formula 2.27. Apart from the small adjustment of the absolute scattering intensity, these are 3-parameter fits with a constraint: according to assumption (2), the aggregate size distribution should depend neither on the mixture A concentration in nitrobenzene nor the temperature.

Indeed, all the SAXS experimental data taken at temperatures above T_c can be interpreted as a sum of scattering by two types of objects: (i) n-alkane monomers distributed like in mixture A and (ii) 4.5 Å thick square aggregates distributed according to a single truncated lognormal distribution. We show below that the latter distribution logically follows from assumption (2). Furthermore, the observed systematic variation of the aggregate concentration with

Table 3.2: Absolute volume fraction of the aggregated paraffin molecules in nitrobenzene-based model fuels at various temperatures. The experimental error is ±0.005.

model fuel	temperature (°C)				
	−30	0	20	50	70
20% A in NB	0	0.056	0.09	0.02	0.01
15% A in NB			0.068	0.01	0.01
10% A in NB			0.003	0	0

the temperature and paraffin concentration (table 3.2 and figure 3.11), and the dissolution of aggregates at high temperatures in particular, lend further support to our model.

Although the results of fits presented above seem to be conclusive, we have looked into the question of the shape of aggregates in a more specific way. As described in detail in the following chapter, we have sampled the liquid phase of model fuels at various temperatures and the distribution of n-alkanes in each sample was determined using gas chromatography. Using assumption (2) it was possible to calculate a hypothetical distribution of rectangular n-alkane aggregates in the liquid phase for any aspect ratio. At temperatures above T_c the content of n-alkanes in liquid phase does not change with temperature and a single distribution should apply universally. In figure 3.14 we compare the aggregate distributions calculated for three aspect ratios (bars) with the truncated lognormal distribution that gives best fit to the experimental data. It is evident that the distribution of aggregates with aspect ratio equal to unity is closest to the distribution determined by the fitting procedure. This means that if the aggregate distribution had been originally based on the GC data, the fits shown in figures 3.12 and 3.13 would have only one free parameter each, namely the proportion of molecules bound in the aggregates.

Figure 3.15 shows numerical fits to the SAXS data collected for the 20% solution of mixture A in nitrobenzene at the temperature 0°C. In these conditions the model fuel is gellified and this was the lowest temperature at which it was possible to collect samples of liquid phase for GC analysis. Theoretical fit performed according to our structural model resulted in the distribution of square aggregates (AR= 1) much narrower than that obtained for the room temperature data. A comparison of this distribution with its counterpart calculated on the basis of GC data is shown in figure 3.16. Once again, the agreement between the two distributions is very good. This provides a very strong argument supporting our aggregation model.

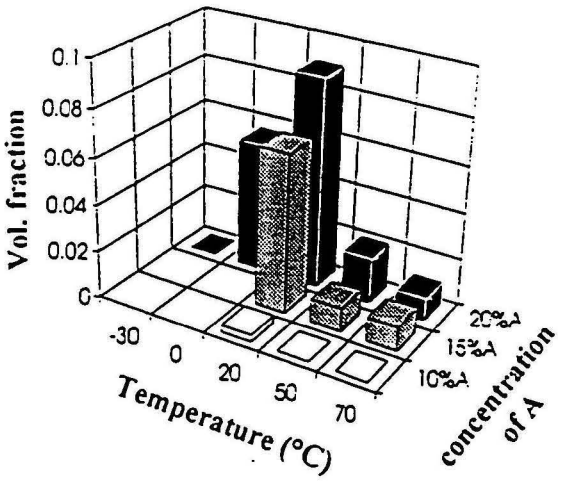

Figure 3.11: Absolute volume fraction of the aggregated paraffin molecules in nitrobenzene-based model fuels at various temperatures. Numerical data for this figure are compiled in table 3.2.

The SAXS results for model fuels based on nitrobenzene indicate that fuel solidification occurs by gellification at a pour point several degrees Celsius below T_c. For instance, for the 20% solution of mixture A in nitrobenzene $T_c = 17.8°C$ and pour point is at 10°C. It is a remarkable finding that throughout a wide temperature range above and below T_c the n-alkanes form atomically thin, side-to-side, roughly square aggregates of like molecules. The concentration of these aggregates seems to be largest at temperatures near T_c, where up to 30% of n-alkane molecules may be aggregated (table 3.2). These aggregates do not act as nuclei of crystallisation. At temperatures below T_c the liquid phase containing both aggregates and n-alkane monomers coexists with the crystalline phase and the amorphous phase. As the temperature decreaseas below T_c, the n-alkanes are selectively incorporated into the solid phase, starting with the heavy ones. Model fuels solidify entirely (in the bulk) at temperatures much lower than pour point (at about −30°C for the 20% solution of mixture A in nitrobenzene). The solid phase is predominantly amorphous.

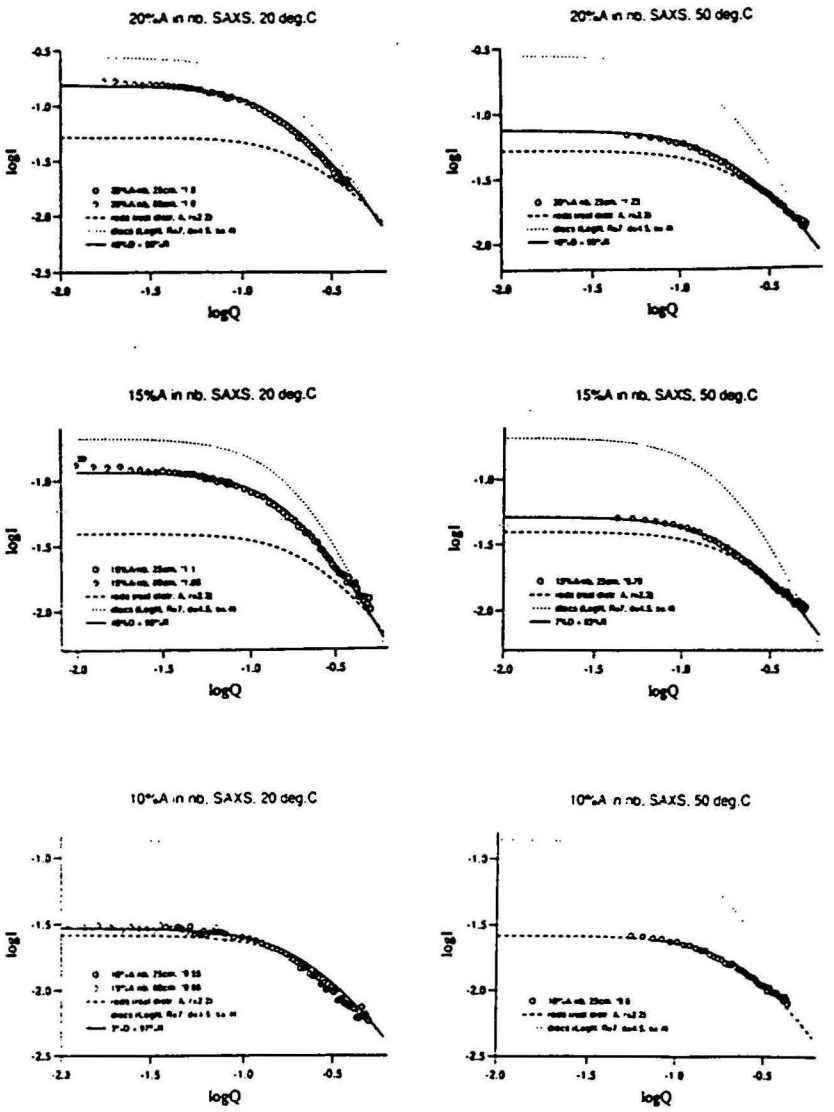

Figure 3.12: SAXS data for 10%, 15% and 20% solution of mixture A in nitrobenzene at 20°C and 50°C. Full information about data and the fitting procedure is displayed in the legend. Broken line corresponds to the calculated scattering by monomers, dotted line by aggregates and the final fit is shown with the solid line.

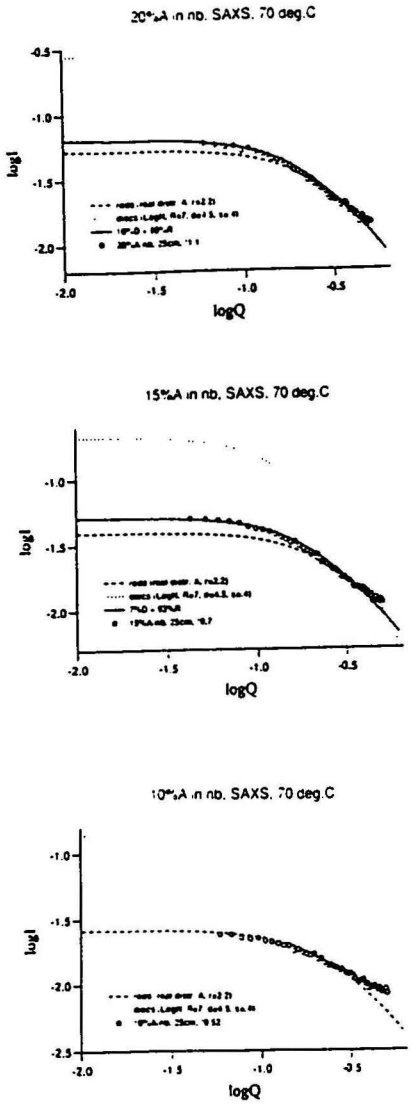

Figure 3.13: SAXS data for 10%, 15% and 20% solution of mixture A in nitrobenzene at 70°C. Full information about data and the fitting procedure is displayed in the legend. Broken line corresponds to the calculated scattering by monomers, dotted line by aggregates and the final fit is shown with the solid line.

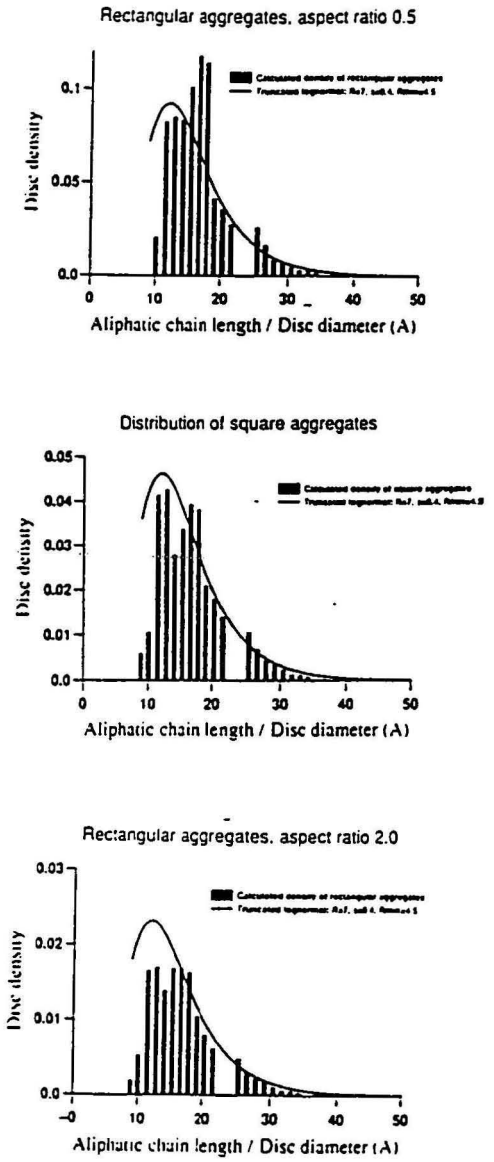

Figure 3.14: Comparison of the best-fit aggregate size distribution (for aspect ratio 1) at temperatures above T_c (solid line) with the distributions calculated on the basis of gas chromatography data using assumption (2) for aspect ratios 0.5, 1 and 2 (bars). Note very good agreement for the aspect ratio equal to unity (square aggregates).

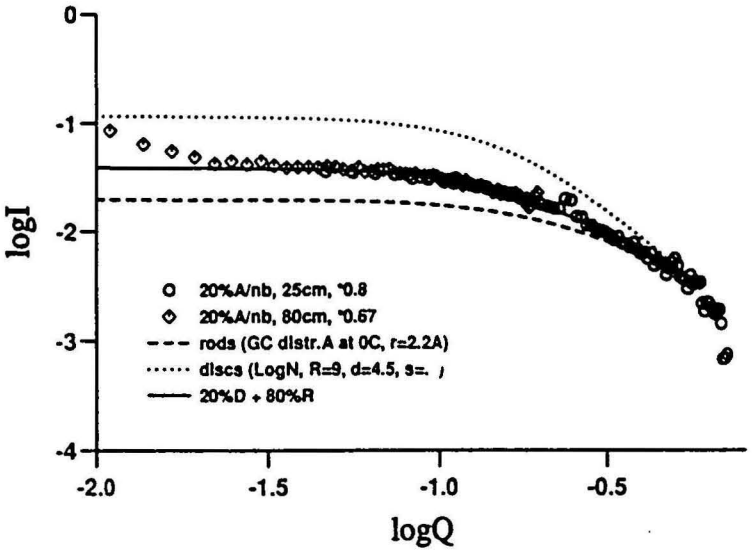

Figure 3.15: SAXS data for the 20% solution of mixture A in nitrobenzene at 0°C. Full information about data and the fitting procedure is displayed in the legend. Broken line corresponds to the calculated scattering by monomers, dotted line by aggregates and the final fit is shown with the solid line.

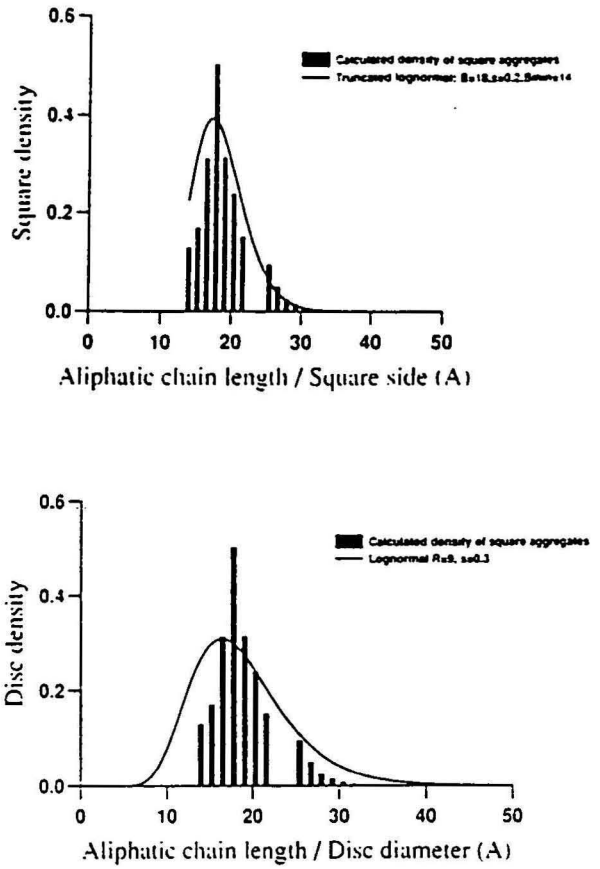

Figure 3.16: Top: comparison of the best-fit aggregate size distribution at the temperature 0°C (solid line) with the distribution calculated on the basis of gas chromatography data using assumption (2) for aspect ratio 1 (bars). Bottom: Sensitivity of the fitting procedure is demonstrated using a lognormal distribution with parameter $\sigma = 0.3$, which is markedly wider that the GC-determined distribution at 0°C, but narrower than the original distribution of mixture A. The distributions represented by bars and solid line are clearly different.

Chapter 4

Small Angle Neutron Scattering in model fuels

4.1 Solutions of mixture A in nitrobenzene

It follows from equations 2.14 and 2.16 that SAXS and SANS provide essentially the same information about the microstructure of model fuels. This is a qualified, statement, however: it is only true if (1) solvent deuteration does not introduce chemically specific changes and (2) the incoherent component of SANS can be eliminated, for instance by using blanks.

For the solutions of mixture A in nitrobenzene the extensive SAXS experiments discussed in the previous section resulted in a detailed structural model for the evolution of liquid phase with temperature. Nevertheless, we have done additional SANS expriments for the solutions of mixture A in deuterated nitrobenzene (D-nitrobenzene) for two specific reasons: firstly, to acquire data that would test the assumptions (1) and (2) and, therefore, enable us to bridge the gap between the SAXS-based information for the nitrobenzene solutions of mixture A and SANS-based information for the D-toluene solutions of mixture A and, secondly, to gain additional insight into the paraffin crystallisation process at temperatures below T_c in the small-Q range, which was not accessible with our SAXS equipment.

Because of the contrast enhancement by solvent deuteration, the absolute scattering cross section for SANS is larger than that for SAXS. This can be directly calculated using equation 2.16 and the scattering length densities shown in figures 2.12 (for SANS) and 2.13 (for SAXS). For the solutions of mixture A in nitrobenzene (SAXS) and D-nitrobenzene (SANS) the calculated SANS-to-SAXS intensity ratio is 4 : 1, and the measured ratios vary from 5 : 1 to 10 : 1. The discrepancy, although not large, reflects the inaccuracy of the absolute intensity calibration inherent in both techniques.

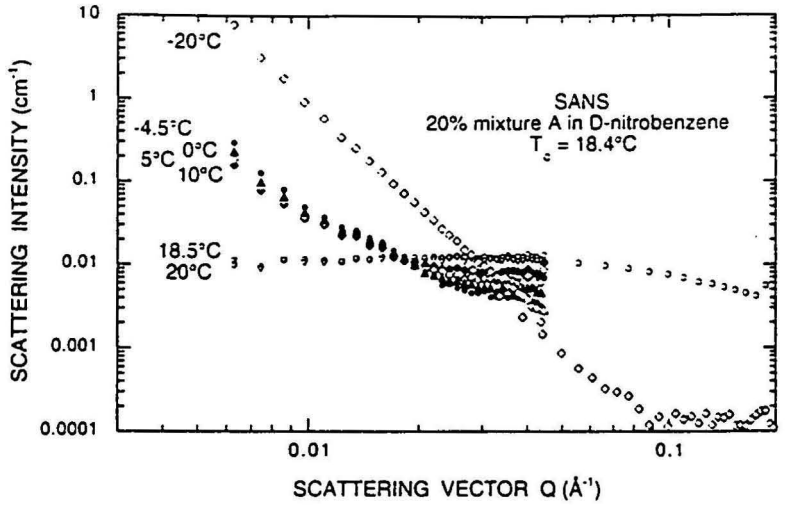

Figure 4.1: SANS data for the 20% solution of mixture A in D-nitrobenzene in the temperature range −20°C to 20°C. The value of T_c is 17.8°C.

Figure 4.1 shows SANS data for the 20% solution of mixture A in deuterated nitrobenzene in the temperature range −20°C to 20°C. Majority of data have been acquired in the small-Q region, but there is an overlap with the corresponding SAXS spectra presented in figure 3.10. When SANS and SAXS spectra taken at room temperature for solutions with various concentrations of mixture A are brought to the same scale the experimental curves coincide in the overlap region, as expected (figure 4.2). In the small-Q region the SANS scattering cross section does not depend on Q, which agrees with the theoretical predictions based on our structural model.

For temperatures gradually decreasing below T_c, the experimental curves in figure 4.1 exhibit an increased contribution from a steep scattering background in the small-Q region. The onset of this background was also observed for the lowest-temperature SAXS curve in figure 3.10. The scattering occurs on the interface between the crystallised paraffin and the liquid (or amorphous) phase and is usually referred to as Porod limit (equation 2.34). Since the crystalline faces are smooth, a Q^{-4} power law is expected and indeed observed in Porod limit. Figure 4.3 shows the Porod region for two different concentrations of mixture A in D-nitrobenzene at −20°C. The specific surface of the crystalline phase, $\frac{S}{V}$, calculated using equation 2.34 for the 20% solution at this temperature is about 4×10^3 cm^2/cm^3. It is important to note that the Q^{-4} power law for the Porod contribution is observed from the onset of the paraffin crystallisation just below T_c. The varying slopes of experimental curves acquired at different temperatures are caused by the superposition of the temperature-

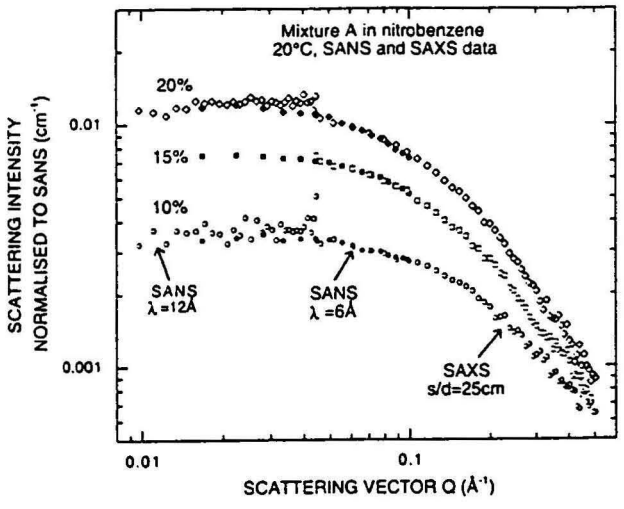

Figure 4.2: Combined SAXS and SANS data for the 10%, 15% and 20% solution of mixture A in nitrobenzene (SAXS) and D-nitrobenzene (SANS) at the temperature 20°C.

dependent liquid phase scattering background and the temperature-dependent Porod contribution. The fact that we were able to obtain the expected power law in the entire temperature range by subtracting the liquid phase background from the experimental data shown in figure 4.1 indicates that the scattering from blanks has well represented the incoherent scattering of our samples.

4.2 Solutions of single n-alkanes in toluene

SANS data have been acquired for D-toluene solutions of three n-alkanes: C15, C20 and C28. The experiments were performed at several temperatures from −6.5°C to 40°C and the paraffin concentration ranged from 10% to 80%. The results are compiled in figures 4.4, 4.5, 4.6 and 4.7.

It is clear that the character of the SANS spectra markedly varies both between different n-alkanes as well as with the n-alkane concentration. Even if the lowest paraffin concentrations of 10% and 20% in deuterated toluene are only considered, the results for different n-alkanes are much more diverse than the corresponding SAXS data for the nitrobenzene solutions.

The scattering of 20% solution of C15 in D-toluene can be modelled in a familiar fashion as a combination of contributions from the monomers and flat aggregates of aspect ratio equal to unity. These aggregates exist at unchanged concentration even 40°C above T_c (figure 4.8 and 4.9). The scattering of the

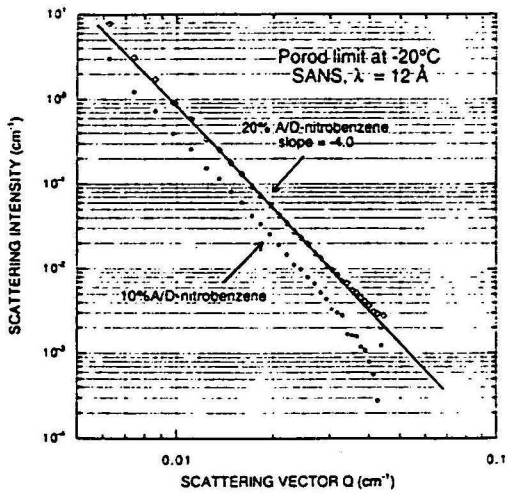

Figure 4.3: Porod region for the SANS spectra of the 10% and 20% solution of mixture A in D-nitrobenzene at the temperature −20°C.

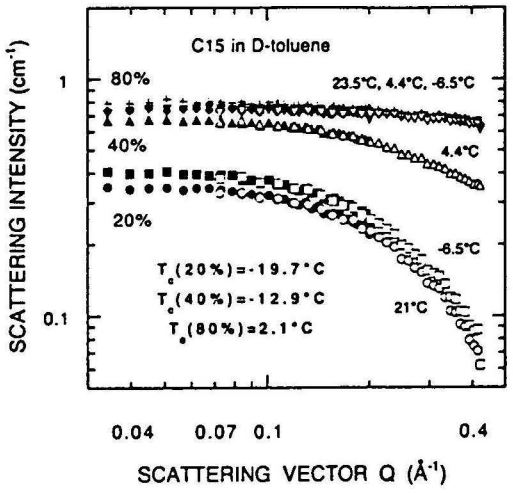

Figure 4.4: SANS results for the 20%, 40% and 80% solution of C15 in D-toluene at various temperatures in the range −6.5°C to 23°C. T_c is the crystallisation temperature.

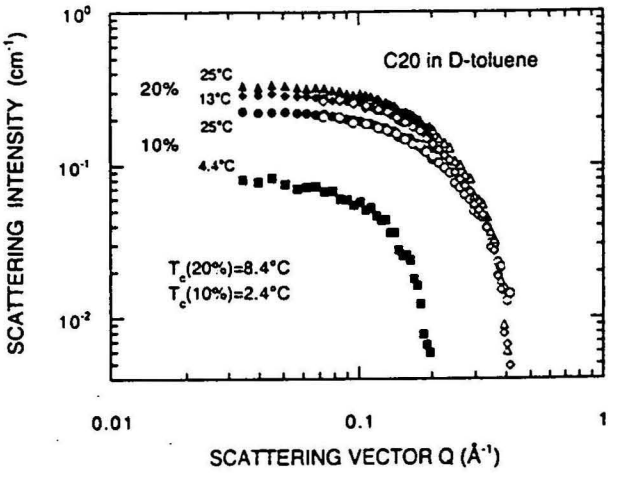

Figure 4.5: SANS results for the 10% and 20% solution of C20 in D-toluene at various temperatures in the range 4.4°C to 25°C. T_c is the crystallisation temperature.

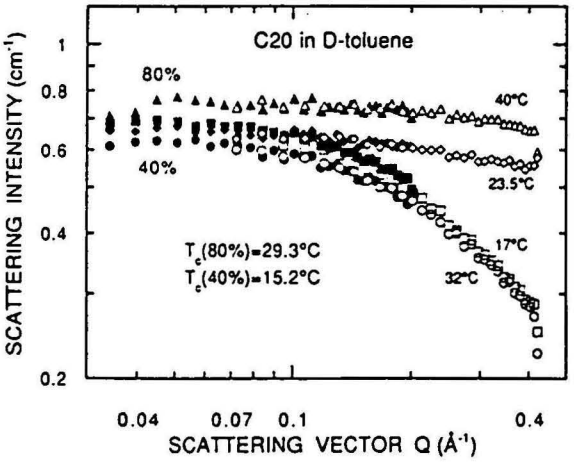

Figure 4.6: SANS results for the 40% and 80% solution of C20 in D-toluene at various temperatures in the range 17°C to 40°C. T_c is the crystallisation temperature.

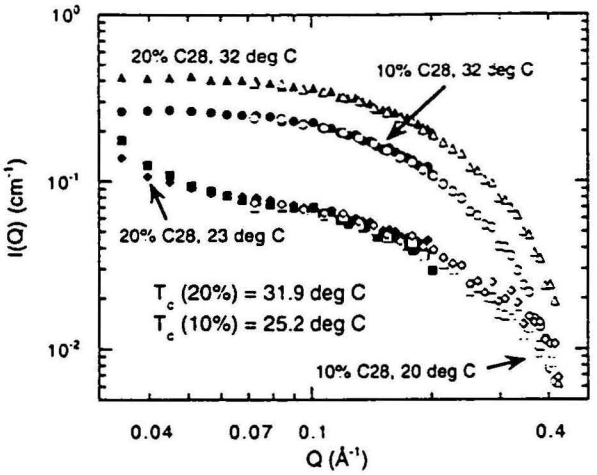

Figure 4.7: SANS results for the 10% and 20% solution of C28 in D-toluene at various temperatures in the range 20°C to 32°C. T_c is the crystallisation temperature.

40% and 80% solutions cannot be modelled in a consistent way. The flattening of scattering spectrum in general indicates the existence of small objects. When these objects are approximated by spheres, however, it turns out that the shape and intensity of experimental curves can be only reproduced using a very compact geometry and unrealistically high contrast values. As illustrated for the 40% solution in figure 4.10, in order to account for the experimental results the scattering objects would have to be of 8Å diameter and contrast would have to exceed that calculated for the C15/D-toluene system by a factor of 2.7. These values would have to be 5Å and 18, respectively, for the 80% solution. Such numbers are obviously non-physical and may indicate that our data contain artefacts caused by, for instance, the multiple scattering effects or some other unknown phenomenon. Therefore, further analysis is limited to the 10% and 20% solutions of n-alkanes in D-toluene.

SANS data for the 20% solution of C20 in D-toluene cannot be interpreted as a combination of scattering from monomers and flat aggregates (figure 4.11). In the large-Q region the experimental points fall off much steeper than the theoretical values, thus indicating that some compact, three-dimensional objects are present in the solution. We have assumed a spherical geometry of the paraffin aggregates and this approximation turned out to provide very good fits for both 10% and 20% solutions. In all the cases, however, the scattering contrast between the aggregates and the solvent (calculated ignoring the volume fraction term in equation 2.16) was smaller than the value $\Delta\rho = 3.7\times10^{21}\text{cm}^{-4}$

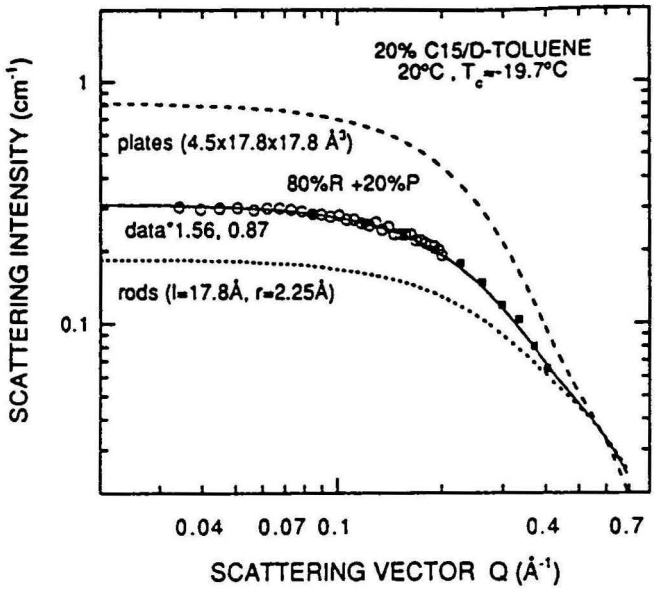

Figure 4.8: Theoretical fits to the SANS data for the 20% solution of C15 in D-toluene at the temperature 20°C. R represents monomers (modelled as rods) and P are flat aggregates (modelled as rectangular plates). Dimensions of rods and plates used in the model are shown. The percentage numbers refer to the relative intensity distribution between the two types of scattering objects. The numbers next to *data** are the multiplication factors used to align data acquired using two different experimental configurations and reflect the accuracy of the absolute calibration procedure. T_c is the crystallisation temperature.

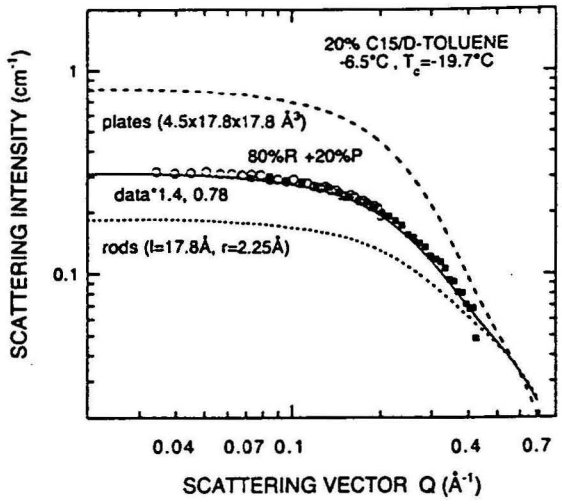

Figure 4.9: Theoretical fits to SANS data for the 20% solution of C15 in D-toluene at the temperature $-6.5°C$. For meaning of symbols see caption to figure 4.8.

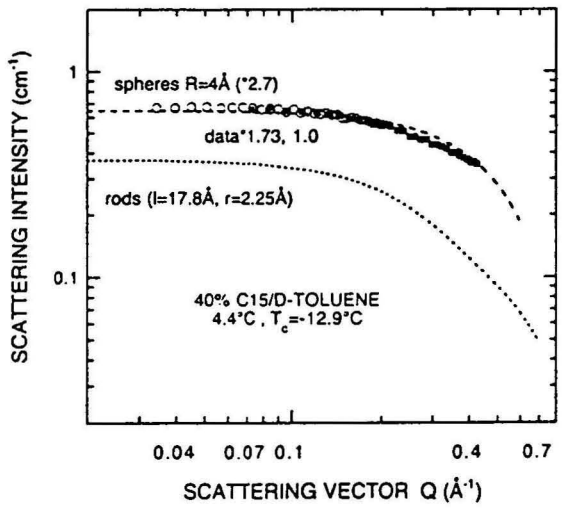

Figure 4.10: Theoretical fits to SANS data for the 40% solution of C15 in D-toluene at the temperature 4.4°C. Note that although a reasonable fit can be obtained using spheres, the required scattering intensity exceeds the calculated value by a factor of 2.7, way beyond the maximum possible absolute calibration error.

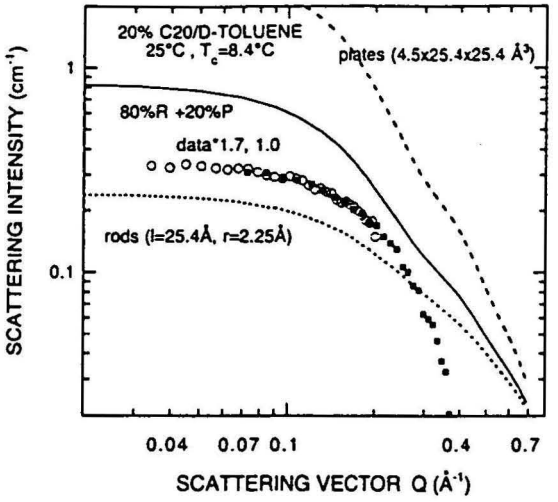

Figure 4.11: SANS data for the 20% solution of C20 in D-toluene at the temperature 25°C and theoretical curves for monomers (rods), flat aggregates (plates) of aspect ratio equal to unity, and a combination of these two curves. Note that no reasonable fit can be obtained.

predicted theoretically for spheres made entirely of n-alkanes. The theoretical-to-experimental contrast ratio (now calculated using full equation 2.16) is about 4.5 at the temperatures above T_c and 67 near T_c. The fits are presented in figures 4.12, 4.13, 4.14 and 4.15.

SANS data for the 10% and 20% solutions of C28 at the temperatures just above T_c can be fitted reasonably well using theoretical formula for monodisperse spheres. As for the solutions of C20, the sphere diameter is about 9Å and the contrast value is by a factor of about 4 less than the theoretical prediction (figures 4.16 and 4.17). The fits are not perfect, though, suggesting that apart from the dominating sphere scattering there may be a small contribution from some other objects. This additional contribution becomes quite apparent at the temperatures below T_c. The SANS data acquired in these conditions cannot be interpreted as due to the scattering by spheres only. In analogy to the situation encountered for the solutions of single n-alkanes in nitrobenzene, we postulate that the additional scattering objects are monomers of n-alkanes (modelled as rods). As illustrated in figures 4.18 and 4.19, very good fits can be obtained except in the small-Q region, where onset of the Porod limit is observed.

It is important to realise that the concentration of C28 in the liquid phase at temperatures below T_c has not been measured. Therefore, the absolute intensity of the theoretical curve for monodisperse spheres now depends on two unknown quantities: the difference of the scattering length densities of the paraffin sphere

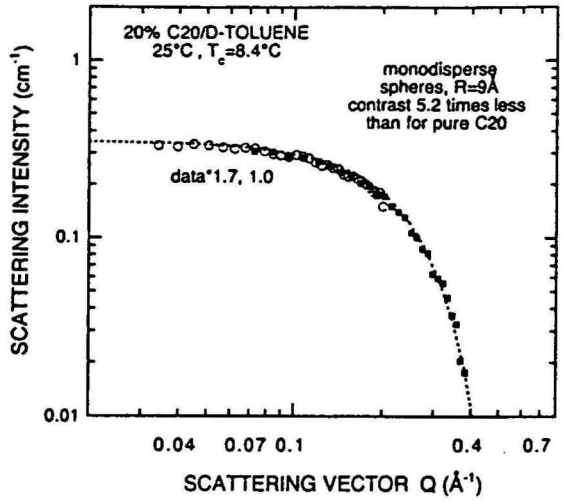

Figure 4.12: Theoretical fit to the SANS data for the 20% solution of C20 in D-toluene at the temperature 25°C. The theoretical curve corresponds to scattering by monodisperse spheres of radius 9Å. The contrast is 5.2 times smaller than predicted theoretically for a purely paraffinic sphere.

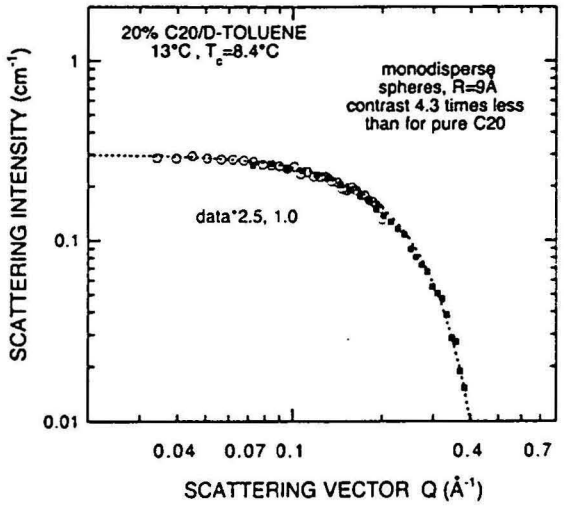

Figure 4.13: Theoretical fit to the SANS data for the 20% solution of C20 in D-toluene at the temperature 13°C. The theoretical curve corresponds to scattering by monodisperse spheres of radius 9Å. The contrast is 4.3 times smaller than predicted theoretically for a purely paraffinic sphere.

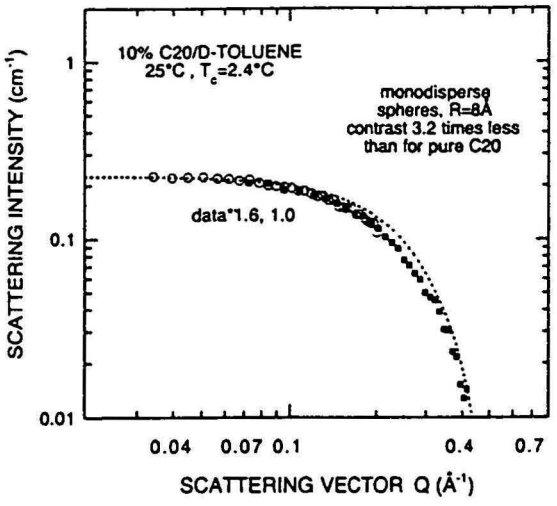

Figure 4.14: Theoretical fit to the SANS data for the 10% solution of C20 in D-toluene at the temperature 25°C. The theoretical curve corresponds to scattering by monodisperse spheres of radius 9Å. The contrast is 4.5 times smaller than predicted theoretically for a purely paraffinic sphere.

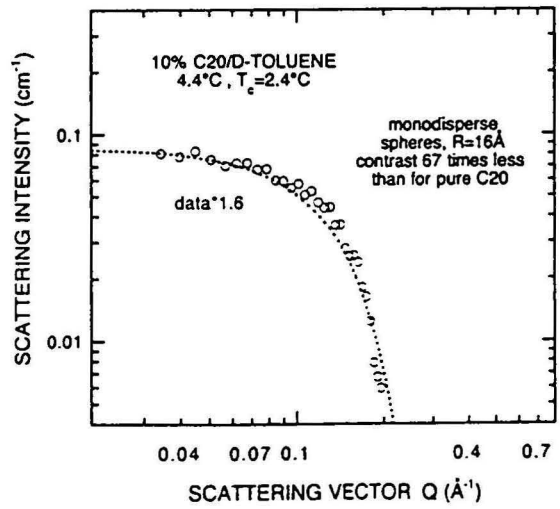

Figure 4.15: Theoretical fit to the SANS data for the 10% solution of C20 in D-toluene at the temperature 4.4°C. The theoretical curve corresponds to scattering by monodisperse spheres of radius 16Å. The contrast is 67 times smaller than predicted theoretically for a purely paraffinic sphere.

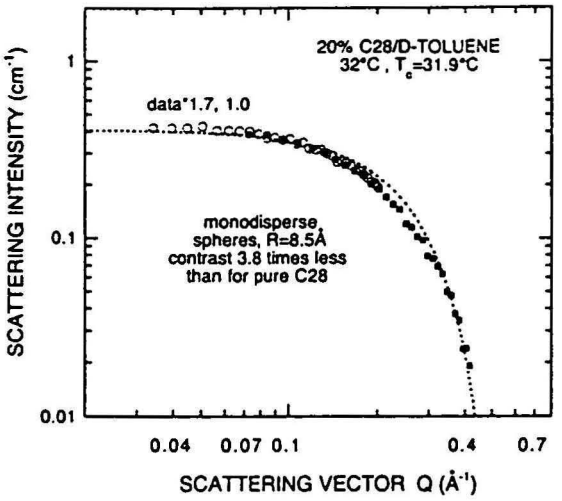

Figure 4.16: Theoretical fit to the SANS data for the 20% solution of C28 in D-toluene at the temperature 32°C. The theoretical curve corresponds to scattering by monodisperse spheres of radius 8.5Å. The contrast is 3.8 times smaller than predicted theoretically for a purely paraffinic sphere.

(comprised of n-alkane and some proportion of solvent trapped inside) and the solvent, and the paraffin volume fraction, both contributing to the contrast value (see equation 2.16). In contrast to this, the geometry of monomers (rods) is well defined and the numerical factor given in the figures after the *rods*$\star$ annotation is the relative concentration of monomers compared to the nominal value originally present in the solution.

From the SANS experiments on the 10% and 20% solutions of selected n-alkanes in deuterated toluene we obtain a detailed picture of the evolution of paraffin aggregation versus the temperature and the aliphatic chain length. The short-chain molecules (exemplified by C15) remain in the solution mostly as monomers, but also form some flat aggregates of four side-to-side molecules of the aspect ratio equal to unity. This is very similar to the behaviour of the solutions of n-alkanes in nitrobenzene. As the chain length increases to C20, all of the n-alkanes present in solution become concentrated in spherical aggregates. For the temperatures well above T_c the aggregates have a monodisperse distribution of apparent radius of about 9Å and their contrast value is 4 to 5 times less than expected for purely paraffinic objects. We believe that the decreased contrast values are related to the microstructure of the scattering objects: owing to the constraints on the paraffinic chain conformations, certain volume within each scattering object is occupied by solvent molecules.

A simple calculation shows that a densely packed sphere of radius 9Å could

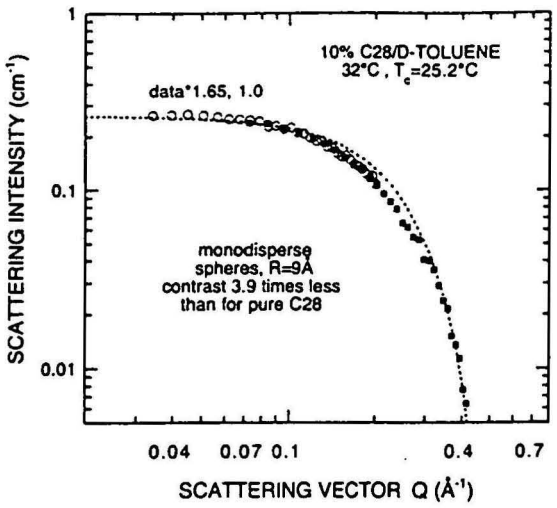

Figure 4.17: Theoretical fit to the SANS data for the 10% solution of C28 in D-toluene at the temperature 32°C. The theoretical curve corresponds to scattering by monodisperse spheres of radius 9Å. The contrast is 3.9 times smaller than predicted theoretically for a purely paraffinic sphere.

accommodate only 6 molecules of C20 or 4 molecules of C28. It is a straightforward matter to show using equation 2.16 that in order to lower the contrast by a factor of 4 to 5, the volume fraction of the solvent trapped inside the aggregates should be about 70% for the 10% solutions and 60% for the 20% solutions. This means that the spherical aggregates contain only two or at most three C20 molecules or one to two C28 molecules twisted into a loosely-knit, roughly spherical object easily penetrated by the solvent. Figure 4.15 shows that for C20 n-alkane as the temperature is lowered to a value close to T_c, the aggregates grow to a radius of 16Å. Calculation shows that both the size and the contrast value are consistent with an aggregate of 4 molecules and the volume fraction taken by the solvent of 88.5%. Thus, as the temperature is lowered, one may be observing coalescence of two C20 aggregates into one larger object.

Finally, SANS data for the solutions of C28 in deuterated toluene demonstrate that for even longer aliphatic chains either coiling-up of a single molecule or an aggregation process of two molecules into a loose, roughly spherical object takes place at temperatures above T_c. It is interesting to note that the apparent radius of the sphere is close to 9Å in all the cases which may indicate that, in accordance with our model, the aggregate size is limited by the statistical segment length rather than the total chain length. At temperatures well below T_c a large proportion of the aggregates dissolves (or the single molecules uncoil) and monomers of C28 become visible in the scattering spectrum.

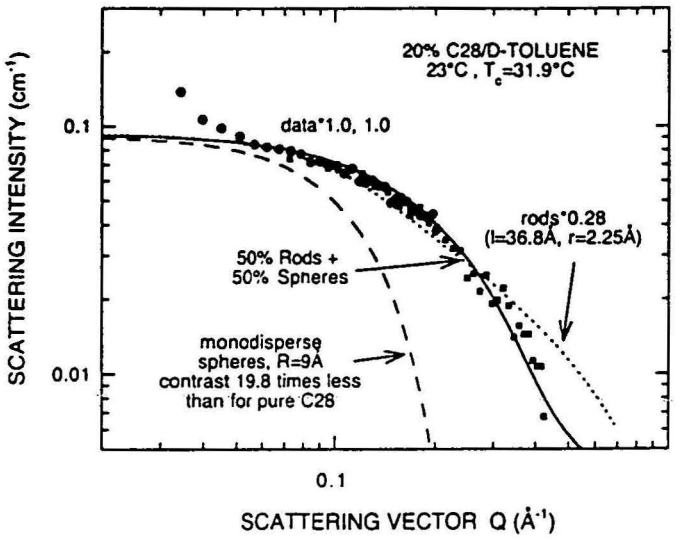

Figure 4.18: Theoretical fit to the SANS data for the 20% solution of C28 in D-toluene at the temperature 23°C. The experimental data are fitted (with solid line) assuming two contributions to the scattering intensity: from monodisperse spheres (radius 9Å, contrast 19.8 times less than for purely paraffinic spheres, broken line) and monomers (dotted line). The absolute intensity of both contributions is the same in the limit $Q = 0$.

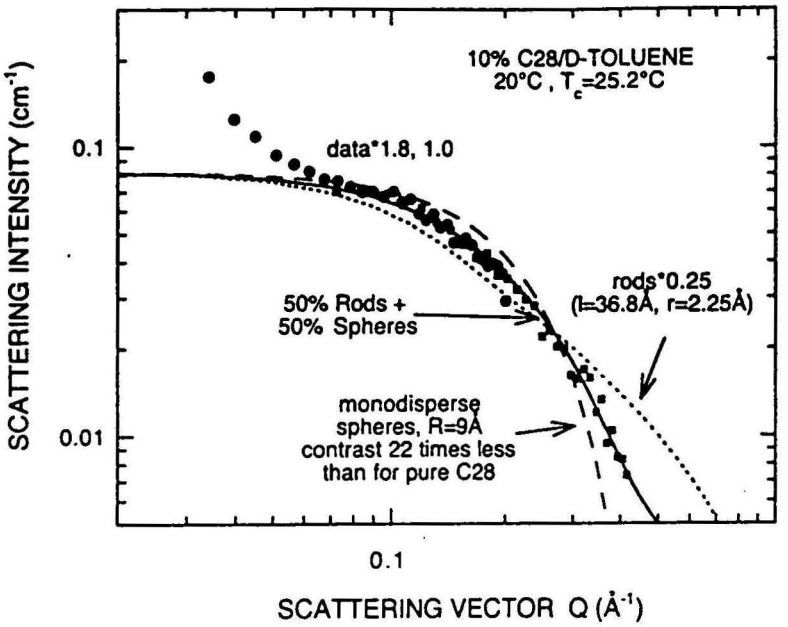

Figure 4.19: Theoretical fit to the SANS data for the 10% solution of C28 in D-toluene at the temperature 20°C. The experimental data are fitted (with solid line) assuming two contributions to the scattering intensity: from monodisperse spheres (radius 9Å, contrast 22 times less than for purely paraffinic spheres, broken line) and monomers (dotted line). The absolute intensity of both contributions is the same in the limit $Q = 0$.

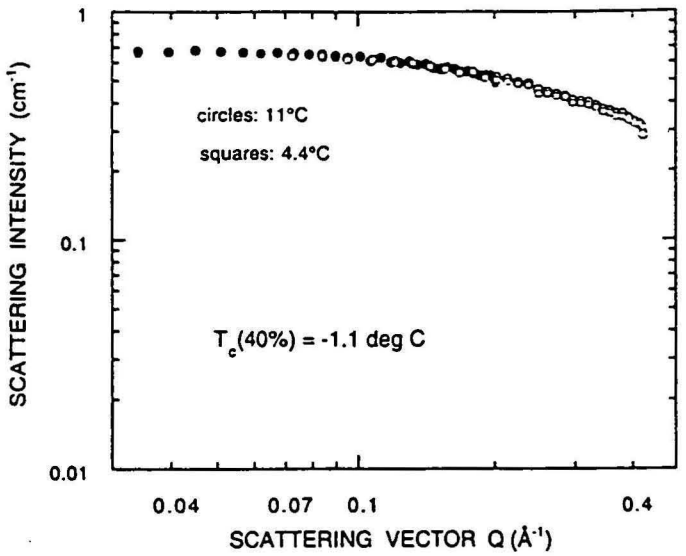

Figure 4.20: SANS results for the 40% solution of mixture A in D-toluene at temperatures 4.4°C and 11°C. T_c is the crystallisation temperature.

4.3 Solutions of mixture A in toluene

Most of the SANS data for D-toluene solutions of mixture A have been acquired in the concentration range 20% to 80%. The general results are presented in figures 4.20, 4.21 and 4.22.

The scattering spectra for the 40% and 80% solutions of mixture A (figures 4.20 and 4.21) are very similar both in shape and the absolute intensity to their single n-alkane counterparts (figures 4.4 and 4.6). Following the same arguments as previously used for the single n-alkane solutions in D-toluene we conclude that the scattering cross sections measured for the 40% and 80% solutions of mixture A are too high to be explained in terms of reasonable contrast values and/or aggregate geometry and probably result from some experimental artefact.

At temperatures above T_c the scattering cross section of the 20% solution of mixture A in D-toluene (figure 4.22) behaves differently than for any other n-alkane solution discussed so far: it keeps rising towards the small Q-values. This can be only explained by allowing for a polydisperse distribution of aggregates. The experimental results have been fitted assuming a bimodal (lognormal for each mode) distribution of spherical aggregates, the two modes being centered around the aggregate radius of 5.25Å and 39.3Å, respectively. It was not possible to fit our data using a unimodal polydisperse distribution. We have assumed that the contrast values for both types of aggregates are the same. Since the smaller objects are dominating the scattering intensity in the large-Q region where most of our data is concentrated, the values of fitting parameters obtained

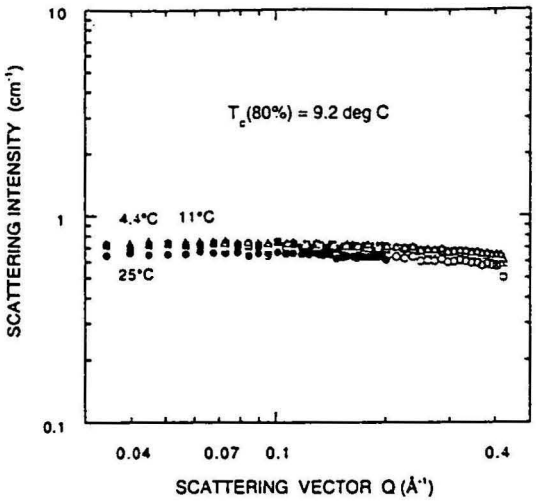

Figure 4.21: SANS results for the 80% solution of mixture A in D-toluene at three temperatures: 4.4°C, 11°C and 25°C. T_c is the crystallisation temperature.

for these objects are highly reliable. In contrast to this, the contribution from the larger objects to the scattering cross section, although clearly visible in the small-Q region, can only be quantified with precision probably not better than 50%.

Using formula 2.19 one can calculate $I(0)$ and compare it with the quantity I_0 obtained from the fit shown in figure 4.22. The neutron contrast between mixture A and D-toluene in a 20% solution is 5.9×10^{20} cm^{-4} and the volume of a 5.25Å radius sphere is 6.1×10^{-22} cm^3. This gives $I(0) = 0.36$ cm^{-1}, which is very close to $I_0 = 0.54$ cm^{-1} obtained from the fit. As I_0 has some contribution from the large scattering objects in addition to that coming from the spheres of radius 5.25Å (see figure 4.22), the calculated and fitted values for the small spheres appear to be very close to each other. This indicates that the small paraffinic spheres are densely packed. No similar conclusion can be drawn for the large aggregates, however, owing to the relatively large uncertainties of the fitted parameters.

Close packing may indicate that n-alkanes having different number of carbon atoms are involved in forming small aggregates. Based on our results for the solutions of single n-alkanes in D-toluene it is unlikely that molecules of one species could form such a compact three-dimensional object. The volume of a 5.25Å radius sphere is similar to the steric volume of the heaviest of n-alkanes present in mixture A. Therefore, it appears possible that the small aggregates are composed of one heavier molecule and possibly up to several light ones filling up the 'correlation hole' of the long chain. The very small number of large objects

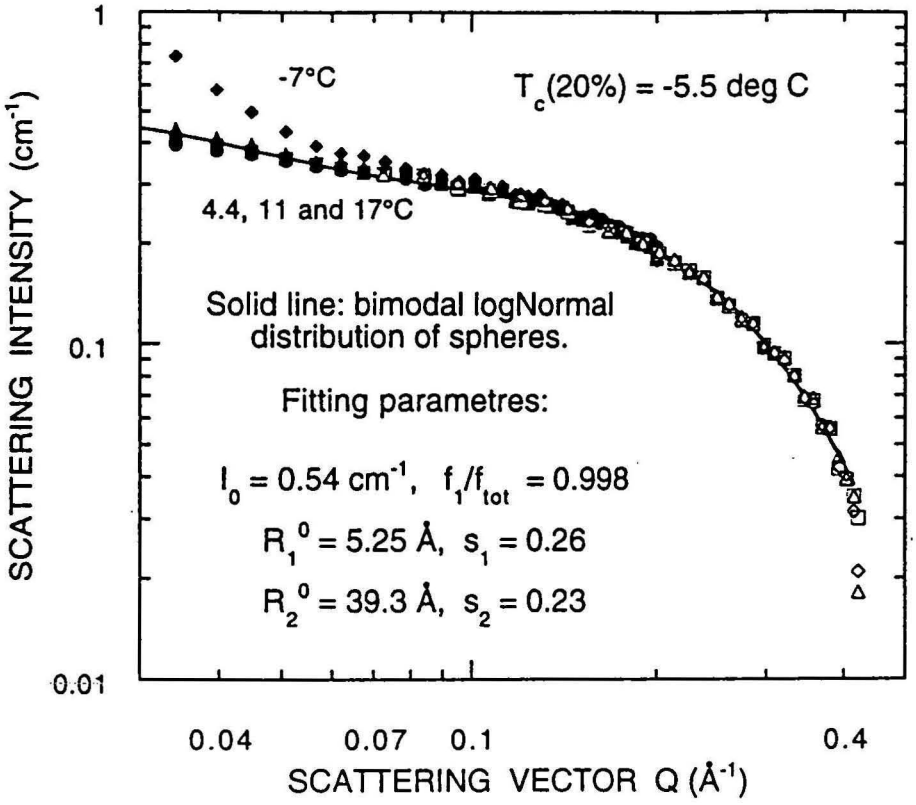

Figure 4.22: SANS results for the 20% solution of mixture A in D-toluene at various temperatures in the range −7°C to 17°C. T_c is the crystallisation temperature. The solid line shows a fit to the bimodal polydisperse model of spherical aggregates. The following fitting parameters have been used: I_0 - the total scattering cross section in the limit $Q = 0$, f_1 - volume fraction of type 1 (small spheres) aggregates, f_{tot} - total volume fraction of aggregates, ${R_1}^0$ - mean radius of type 1 aggregates, s_1 - standard deviation of the lognormal distribution of type 1 aggregates, ${R_2}^0$ - mean radius of type 2 aggregates, s_2 - standard deviation of the lognormal distribution of type 2 aggregates. For details see text.

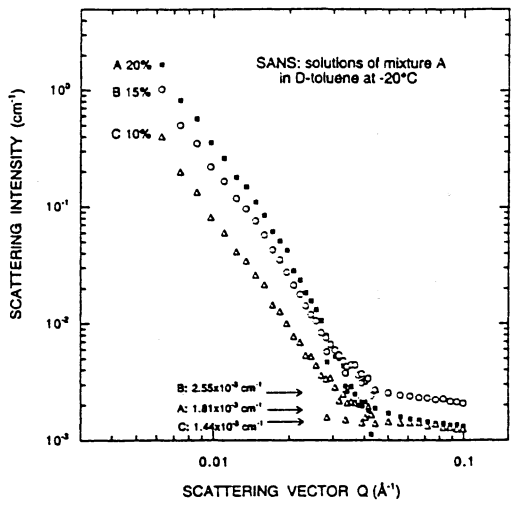

Figure 4.23: SANS results for the 10%, 15% and 20% solution of mixture A in D-toluene at the temperature $-20°C$. Arrows indicate the estimated level of the remnant liquid phase scattering background. T_c for all three solutions is above $-10°C$.

observed in the solution are likely to be built from loosely knit heavy molecules without the light counterparts. Such aggregation behaviour is more complex than that observed for the solutions of single n-alkanes in D-toluene: the small aggregates appear to be more compact and the large ones more extended, and both types are size polydisperse.

At temperatures well below T_c the solutions of mixture A in D-toluene gradually solidify. At the temperature $-20°C$ scattering from the liquid phase markedly decreases and one observes a Porod-limit-like scattering on the solidified interface (figure 4.23). After subtracting the estimated background originating from the remnant liquid phase scattering the slopes in the Porod region can be determined (figure 4.24). For the 10% and 15% solution of mixture A in D-toluene the least-square-fitted value of the slope is -3.79 and -3.75, respectively. In both cases the correlation coefficient is larger than 0.99. For the 20% solution of mixture A there is a pronounced non-linearity in the plot, indicating that the experimental results cannot be represented by a simple power law.

Slopes between -4 and -3 in the Porod region of two-phase systems may indicate a surface-fractal interface geometry in the linear scale region 200 Å to 1000 Å [41]. Fractal interpretation of the results presented in figure 4.24 would require more detailed studies of the three phases present in the system: the crystalline, amorphous and the liquid one. In particular, one would wish to explain why the interface geometry is smooth (Euclidean) for the solidified

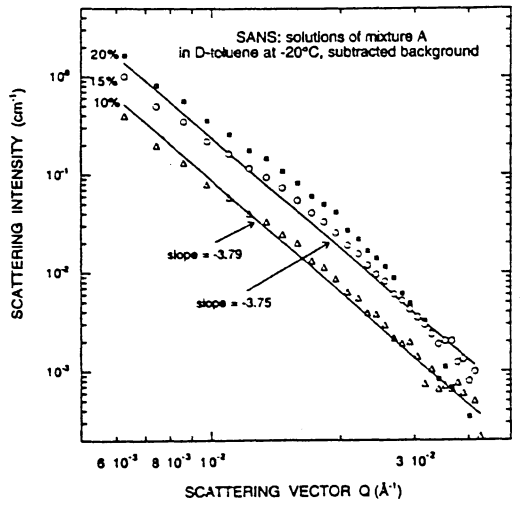

Figure 4.24: SANS data in the Porod region for the 10%, 15% and 20% solution of mixture A in D-toluene at the temperature $-20°C$. Background scattering due to the liquid phase pockets has been subtracted. The slopes have been determined using the least-squares method.

solutions of mixture A in D-nitrobenzene and rough (fractal) in D-toluene. Detailed structural studies of the solid phases below T_c are, however, outside the scope of this report.

Chapter 5

Gas chromatography studies of model fuels at various temperatures

5.1 Gas chromatography data

5.1.1 The methodology of sampling

The distribution of normal alkanes and solvent between the liquid and solid phase at different temperatures below the cloud point is an important piece of information required for the fine-tuning of thermodynamic models of paraffin crystallisation in complex systems. Prior to this project no such data were available in the public domain literature. Using the slightly modified optical system for video observation of T_c we have been able to extract samples of liquid phase under strictly controlled conditions.

For the nitrobenzene solutions of mixture A, where the paraffin crystals are large and float on the surface, it was sufficient to use an automatic pipette for sampling the liquid. The fuel specimen was maintained in a 20 ml glass bottle at the required temperature and the tip of pipette was positioned in a crystal-free region observed on the video monitor. The pipette was programmed to the lowest flow rate in order not to stir the liquid. Typically, a sample of 100 microlitres was taken for GC analysis. The sampling process was continously monitored and only crystal-free samples were kept. The fuel remaining in the bottle after sampling was disposed of. The paraffin crystals in toluene solutions of mixture A are very fine. They are also denser than the surrounding liquid. At a constant temperature below T_c these crystals would eventually deposit on the bottom, but even very delicate currents in the liquid would agitate them to form a suspension. Under these circumstances it was not possible to use the

automatic pipette for liquid sampling. Instead, the sampling was done using a syringe equipped with a 450 nm disposable paper filter. In order to prevent the paraffin crystals from melting in contact with the warm tissue, the filters were stored in a loosely-knit basket over the free surface of liquid nitrogen. The temperature in the basket was monitored with a digital thermometer and maintained at a value close to that of the sampled fuel. The temperature of filters was adjusted as necessary by changing the position of the basket in respect to the liquid nitrogen surface.

5.1.2 Results and discussion

Gas chromatography (GC) is a quantitative analytical technique that can be used to determine the absolute amount of individual n-alkanes in the total mass of the sample. GC takes advantage of different volatility of individual components in a complex mixture, which would therefore separate from the liquid phase in the GC column at different temperatures. A known amount of the analysed sample is introduced to the injection chamber. The resulting signal at the detector can be expressed in the absolute units of mass per unit volume after the calibration with standards of known concentration has been made. Usually the results are expressed in weight percent of n-alkane in the total sample volume. As the density of both solvent and solute are known, this could be readily translated into the volume percent.

Figure 5.1 shows a GC recorder trace obtained for two different samples of 5 vol% solution of mixture A in nitrobenzene, one collected at 20°C and another at −38.3°C. The peaks correspond to individual n-alkanes, with the maximum intensity for the most abundant n-alkane, C15. The n-alkane concentration by weight is proportional to the peak area.

Typically, six to nine samples of liquid phase have been collected at as many different temperatures in the region between the cloud point and pour point for each model fuel. Nine different concentrations of mixture A were studied, five in nitrobenzene and four in toluene.

Solutions of mixture A in nitrobenzene

The total paraffin content in the liquid phase versus temperature is shown in figure 5.2. Data obtained for high and low concentration solutions indicate a strikingly different behaviour below T_c. For the high concentration samples the total amount of paraffins in the liquid phase systematically decreases at low temperatures, which indicates that n-alkanes preferentially segregate into the solid phase. For the low concentrations of mixture A, however, there is no evidence of segregation. This indicates that nitrobenzene is either incorporated into the solid structure or microscopically trapped inside it. Transition between the two types of behaviour is gradual and occurs at the concentration of mixture A between 10 vol% and 15 vol%.

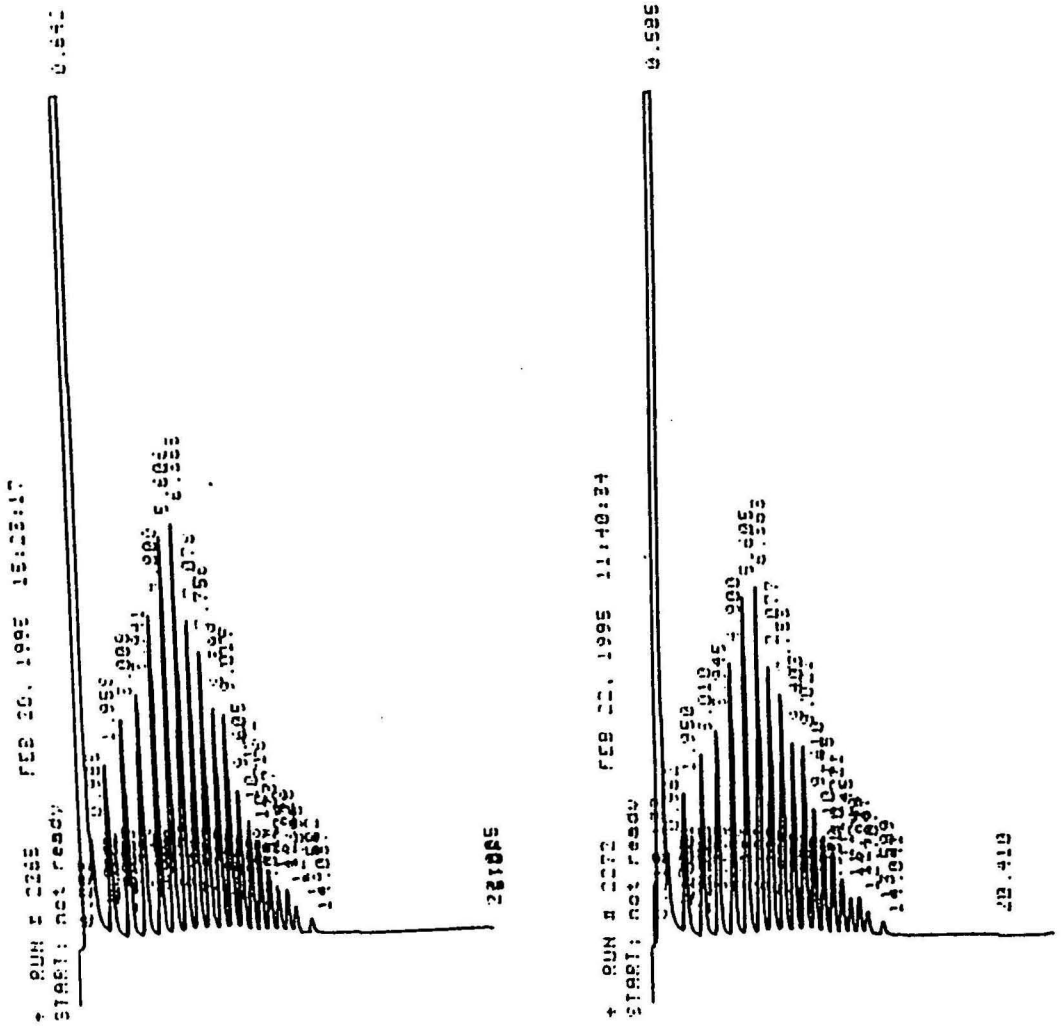

Figure 5.1: Gas chromatograms obtained for two samples of liquid phase extracted from a 5 vol% solution of mixture A in nitrobenzene at 20°C (left) and −38.3°C (right).

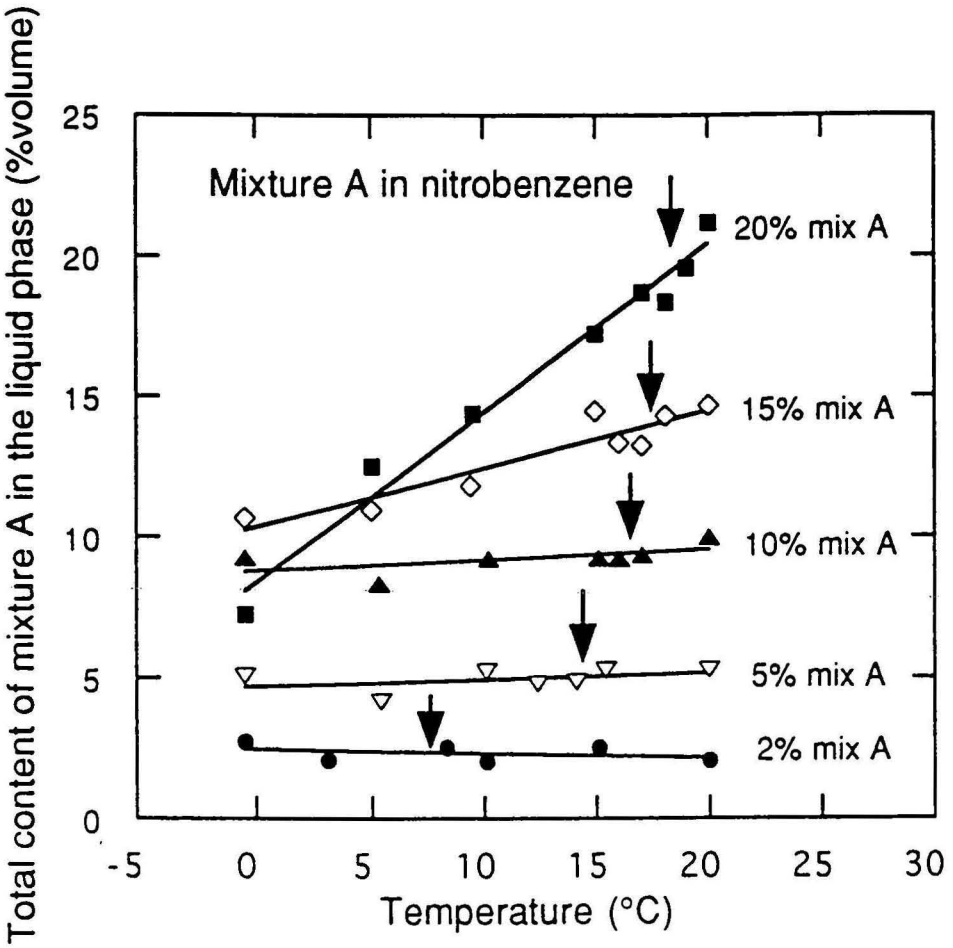

Figure 5.2: The total content of normal alkanes in the liquid phase of various nitrobenzene solutions versus temperature. Lines are guide for the eye only. The optically determined crystallisation temperatures are indicated with arrows.

The sequence in which the n-alkanes are removed from the liquid phase of the 20% solution of mixture A in nitrobenzene as the temperature drops is illustrated in figure 5.3. Part A of the figure shows the overall evolution of the paraffin distribution curve, whereas part B shows the detailed temperature dependence of the concentration of selected n-alkanes.

It follows that as the temperature is lowered below T_c, the heavy (*i.e.* above C20) n-alkanes precipitate first, with practically no change in the light paraffin concentration. This process ends at the temperature about 10°C. Below this temperature the light paraffins between C8 and C15 are being gradually depleted from the liquid phase. No sampling was possible below 0°C since the specimen was entirely solid.

At 0°C the paraffin distribution is much narrower than the original one (figure 5.3, part B). It is interesting to note that the maximum of distribution has not shifted and C15 remainded the most abundant species in the liquid phase. Similar results have been obtained for the 15% solution of mixture A, as illustrated in figure 5.4. Again, the heavy paraffins solidify first and the light ones last, although the latter ones largely remain in the liquid phase. As for the 20% solution, the least affected (in relative terms) is the concentration of C15 at the peak of distribution.

For yet lower concentrations of mixture A, the paraffin content (and their distribution) at low temperatures varies less and less from the original one. This is illustrated in figures 5.5, 5.6 and 5.7 for the 10%, 5% and 2% solutions, respectively. One can see from parts B of these figures that the selective segregation of n-alkanes to the solid phase systematically shifts towards the heaviest species as the concentration of mixture A decreases.

Solutions of mixture A in toluene

The total paraffin content in the liquid phase of mixture A versus temperature in the concentration range 5% to 30% is shown in figure 5.8. The behaviour observed here for the entire concentration range indicates that within experimental error the total n-alkane content in the solid and liquid phase is the same at any temperature. One should note that the measured paraffin content systematically exceeds the nominal values (by weight). This may be caused by some inadvertent loss of solvent during the sampling procedure.

Detailed GC data for individual paraffins are presented in next four figures (5.9, 5.10, 5.11, 5.12). For the 30% (figure 5.9) and, especially, 20% solution (figure 5.10) there is very little segregation between the solid and liquid phase in the entire temperature range. For the 10% and 5% solutions, however, there is a preferential segregation of the heaviest n-alkanes into the solid phase (see curves for C28 in parts B of figures 5.11 and 5.12).

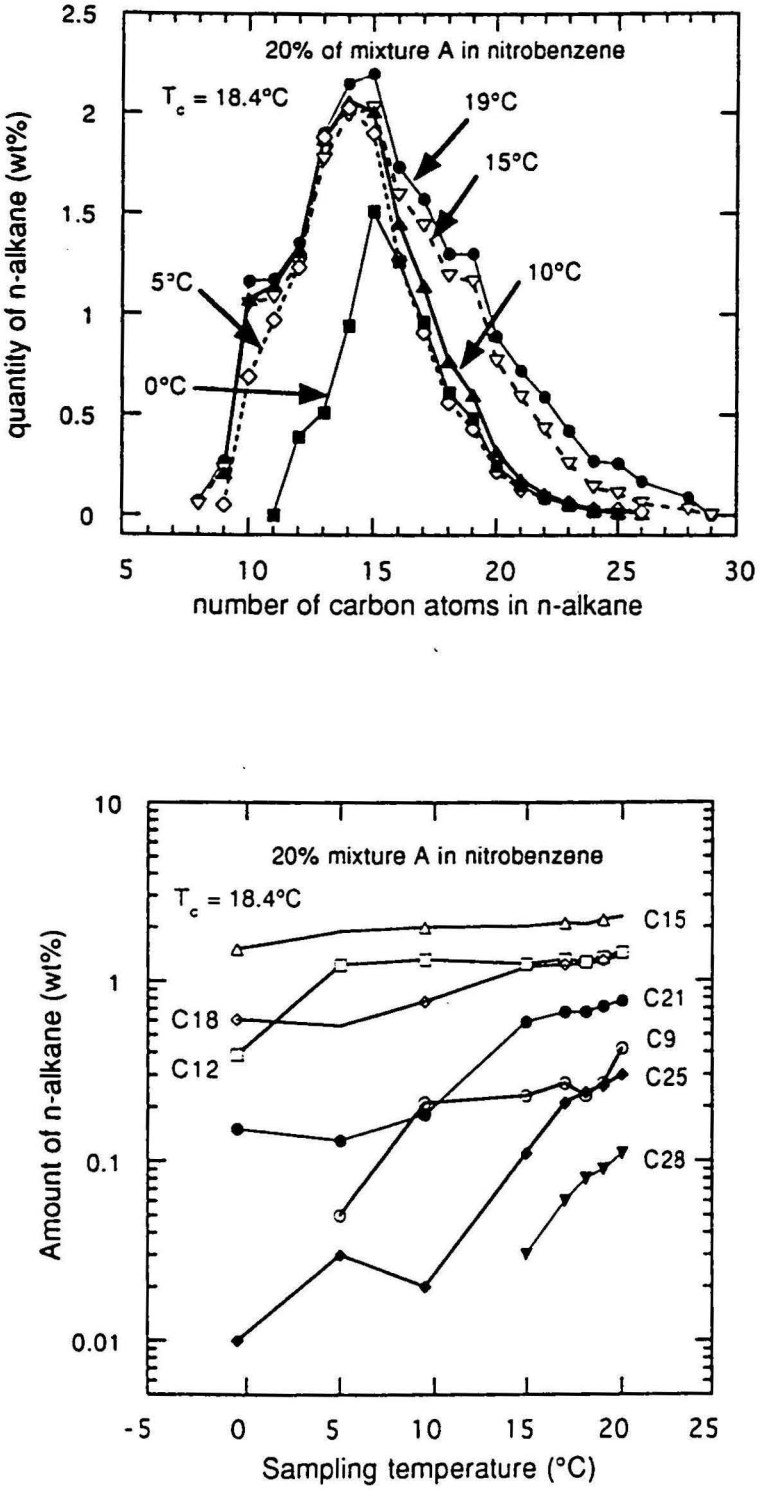

Figure 5.3: The n-alkane content in the liquid phase of 20% solution of mixture A in nitrobenzene versus temperature. A: the paraffin distribution; B: concentration of selected individual n-alkanes.

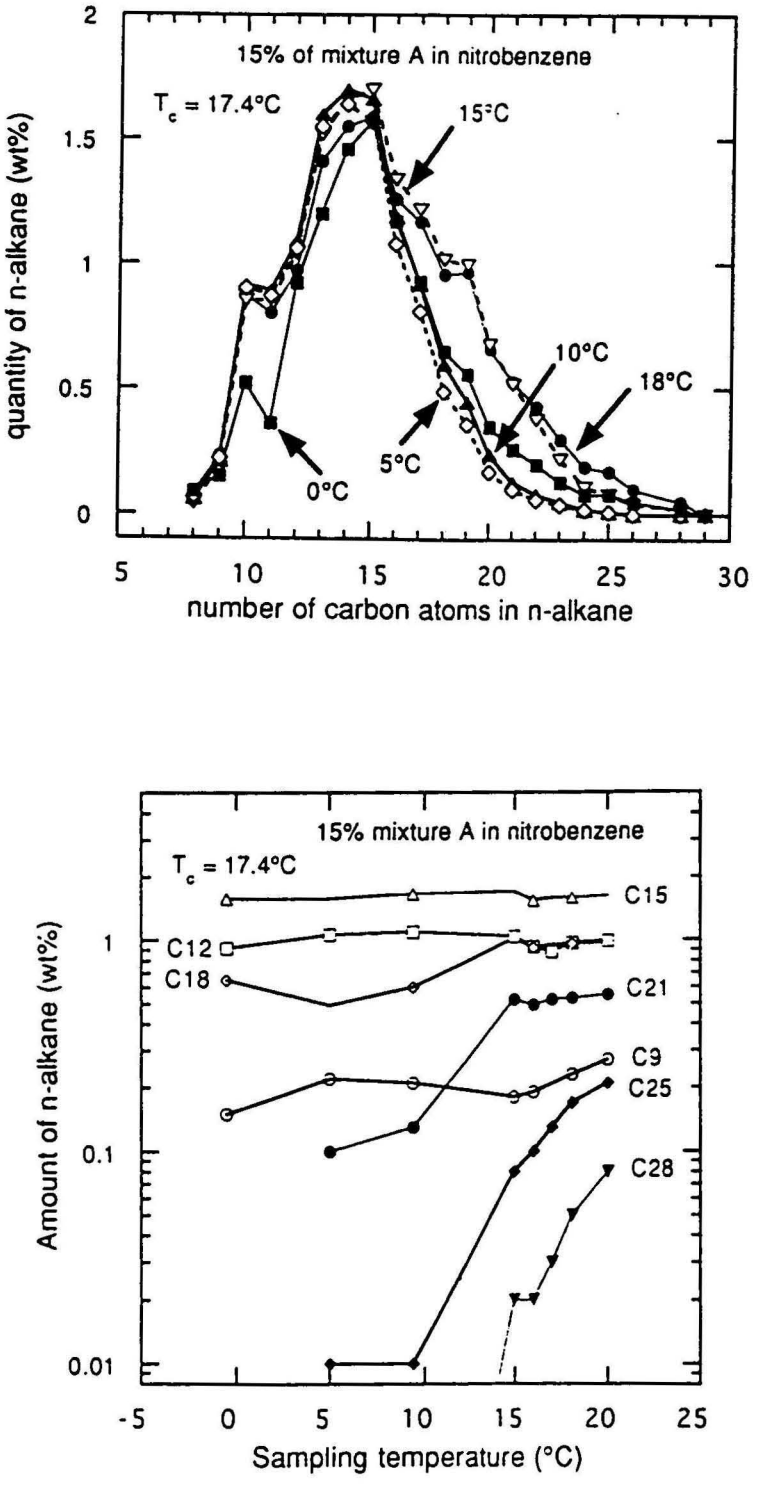

Figure 5.4: The n-alkane content in the liquid phase of 15% solution of mixture A in nitrobenzene versus temperature. A: the paraffin distribution; B: concentration of selected individual n-alkanes.

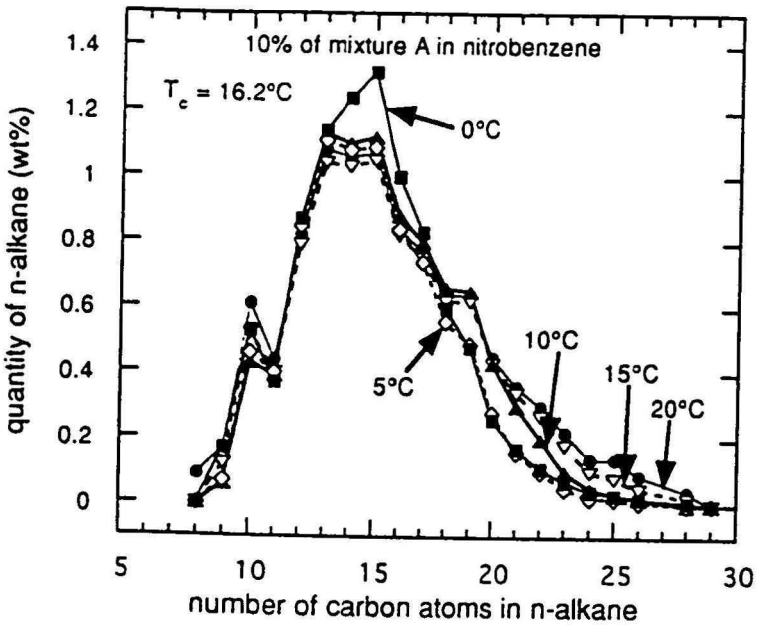

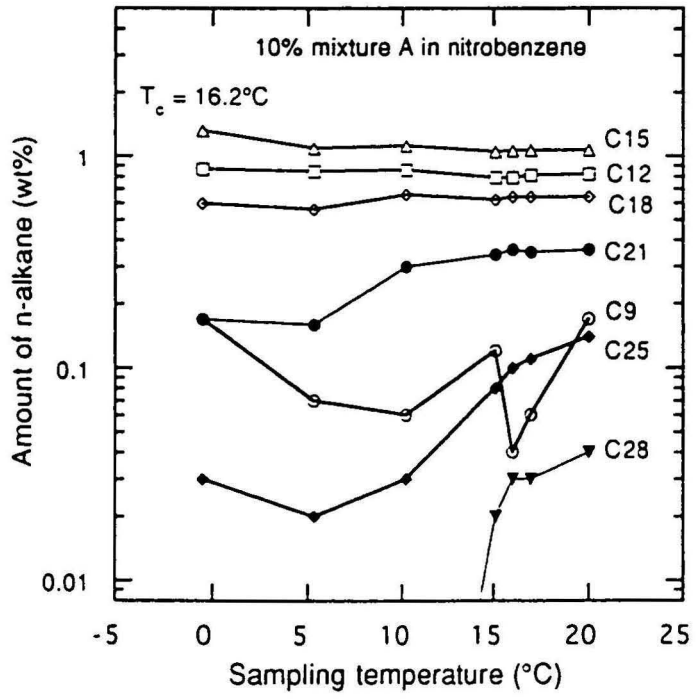

Figure 5.5: The n-alkane content in the liquid phase of 10% solution of mixture A in nitrobenzene versus temperature. A: the paraffin distribution; B: concentration of selected individual n-alkanes.

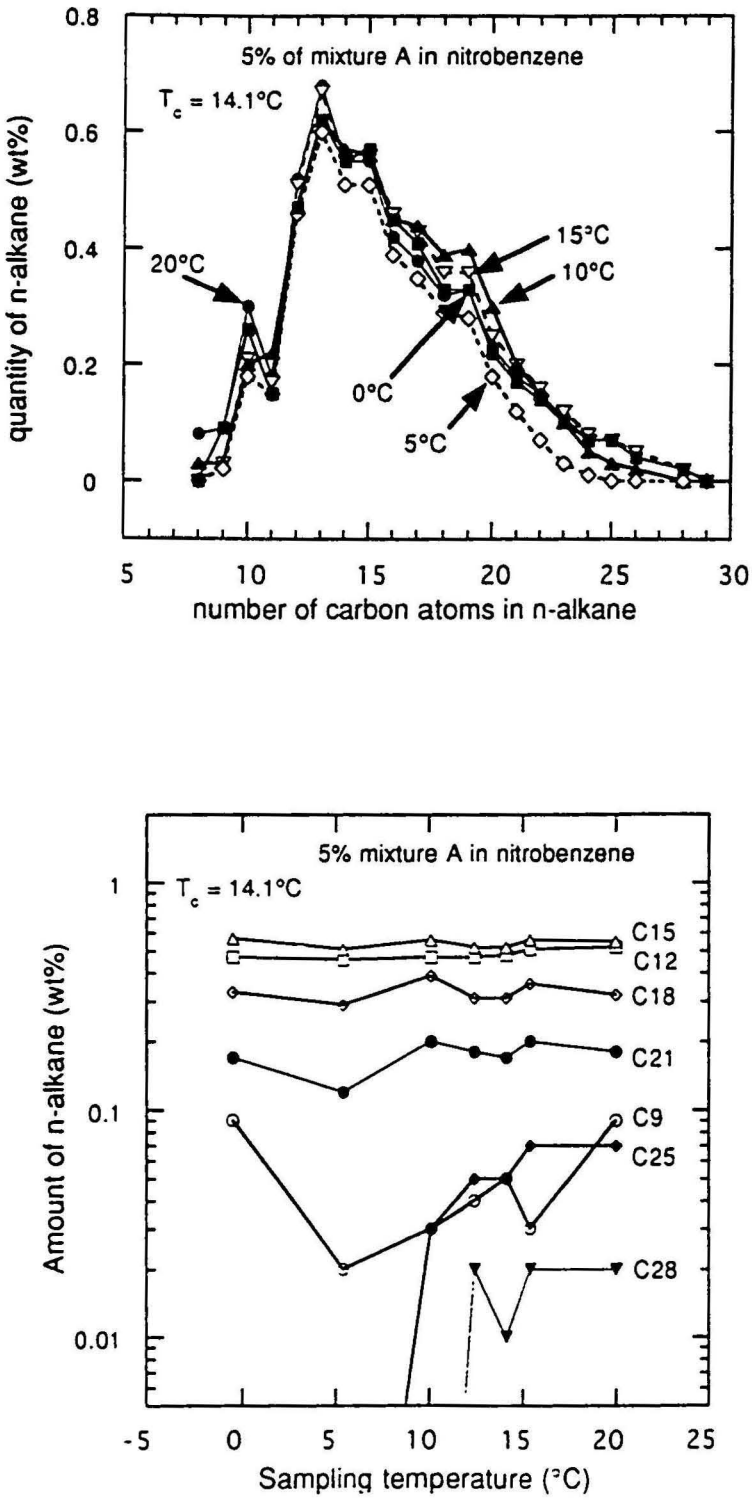

Figure 5.6: The n-alkane content in the liquid phase of 5% solution of mixture A in nitrobenzene versus temperature. A: the paraffin distribution; B: concentration of selected individual n-alkanes.

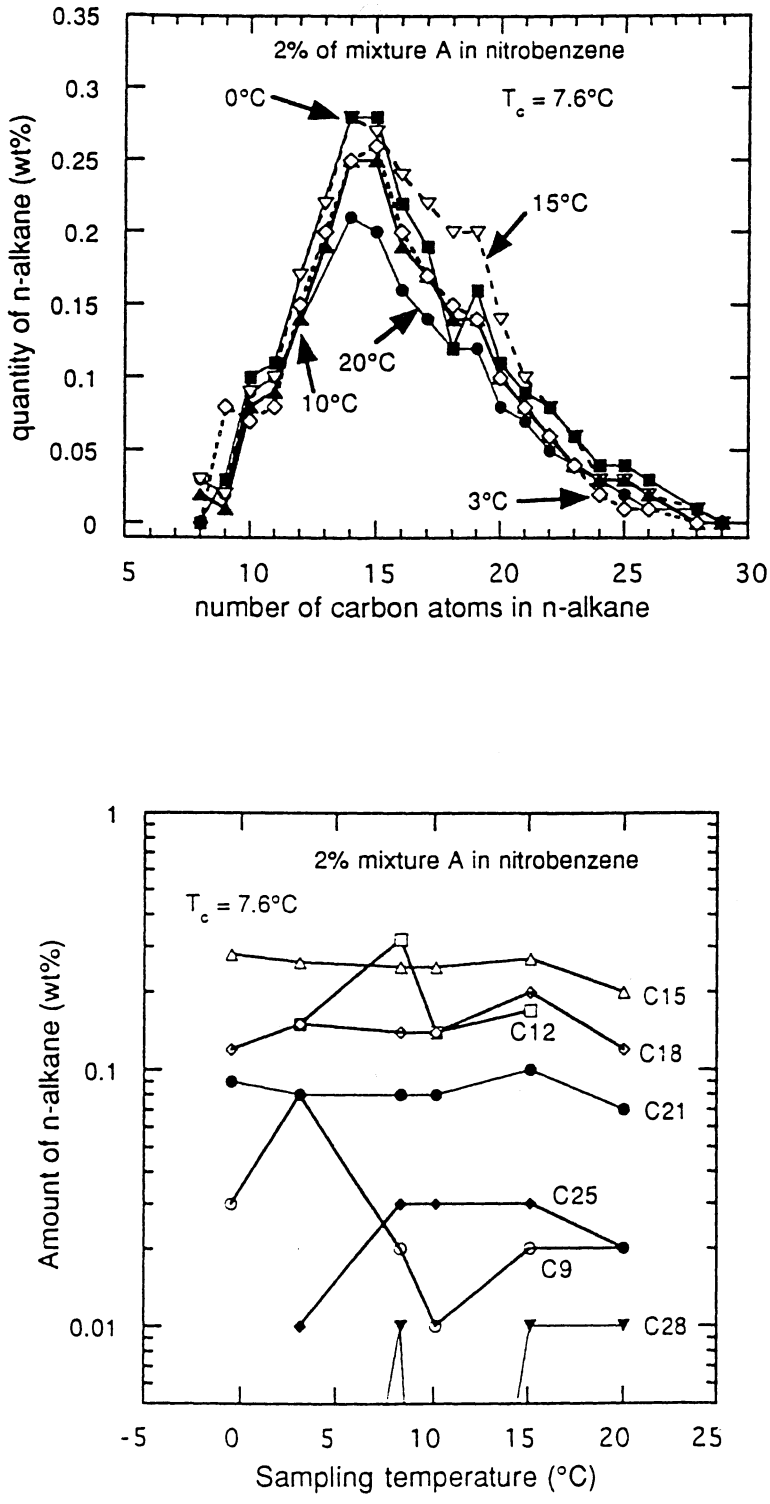

Figure 5.7: The n-alkane content in the liquid phase of 2% solution of mixture A in nitrobenzene versus temperature. A: the paraffin distribution; B: concentration of selected individual n-alkanes.

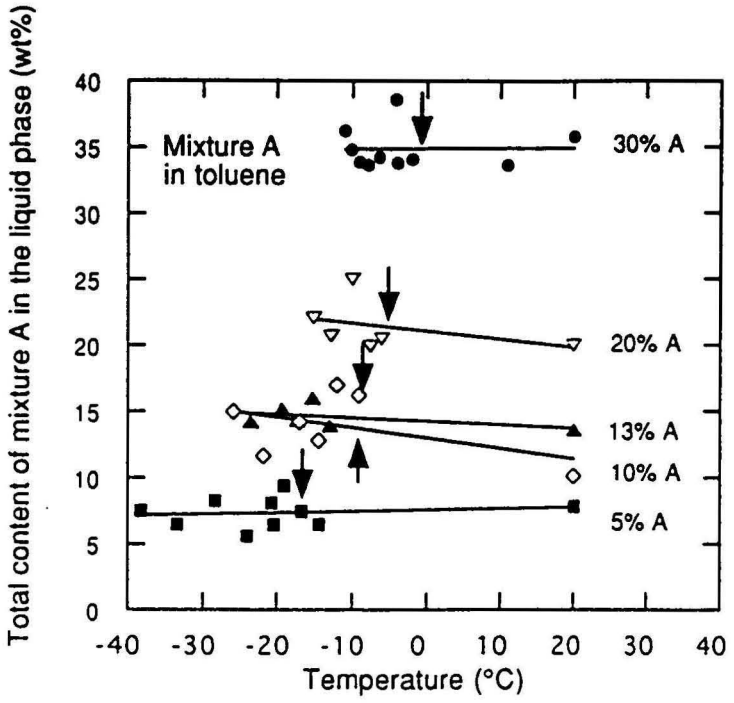

Figure 5.8: The total content of mixture A in the liquid phase of various toluene solutions versus temperature. The optically determined crystallisation temperatures are indicated with arrows.

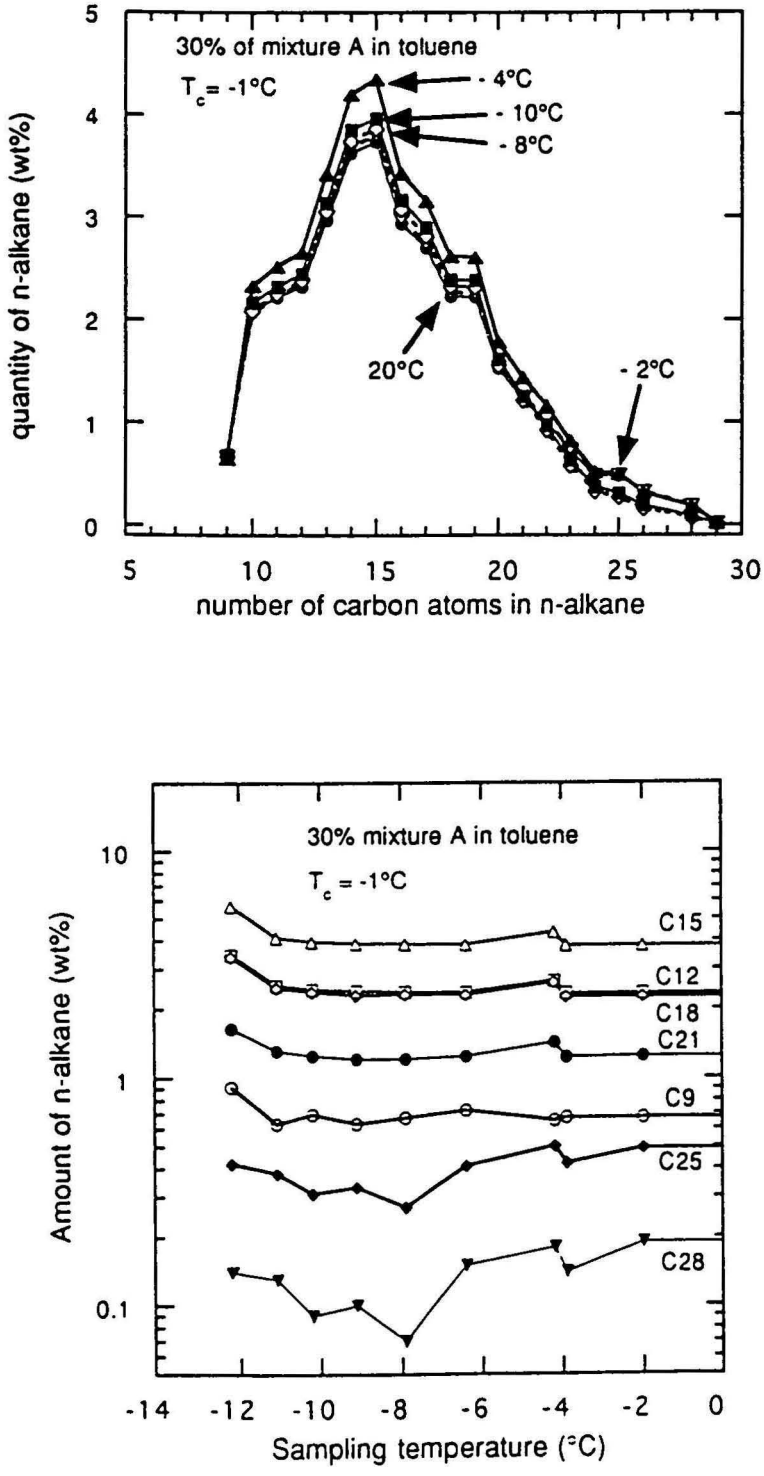

Figure 5.9: The n-alkane content in the liquid phase of 30% solution of mixture A in toluene versus temperature. A: the paraffin distribution; B: concentration of selected individual n-alkanes.

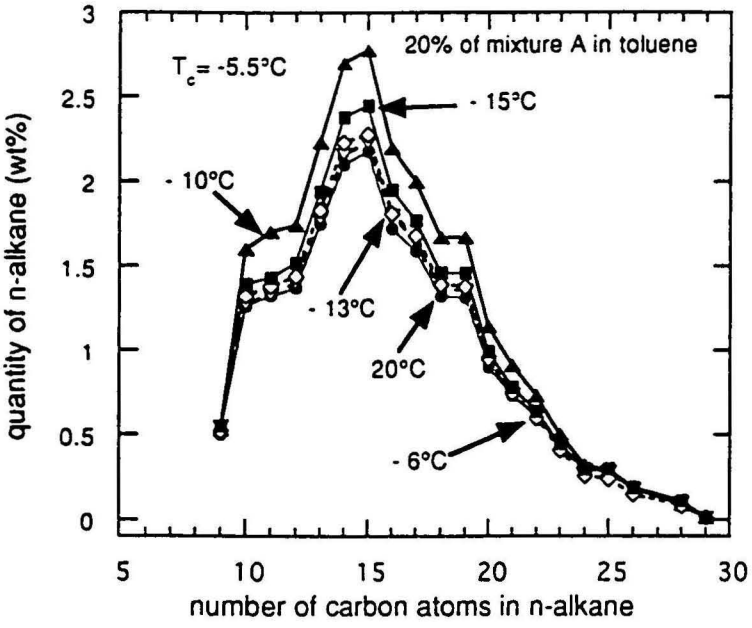

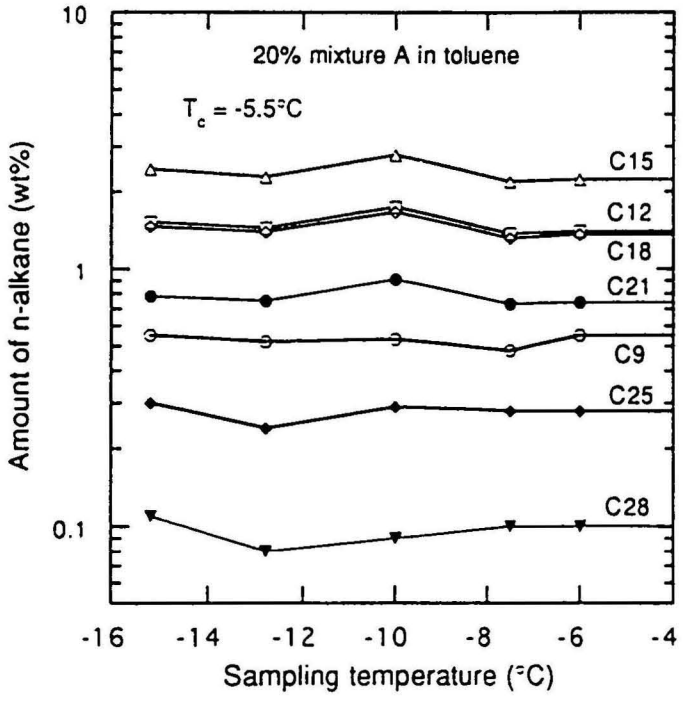

Figure 5.10: The n-alkane content in the liquid phase of 20% solution of mixture A in toluene versus temperature. A: the paraffin distribution; B: concentration of selected individual n-alkanes.

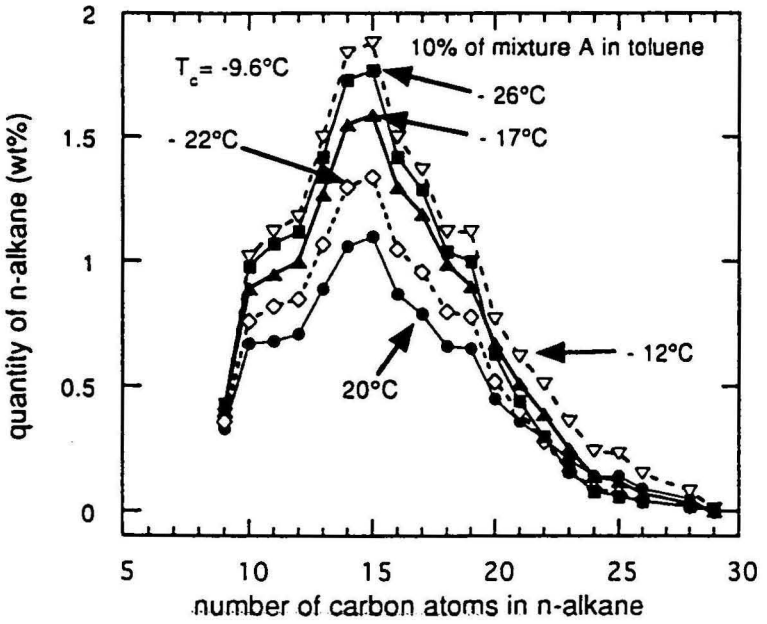

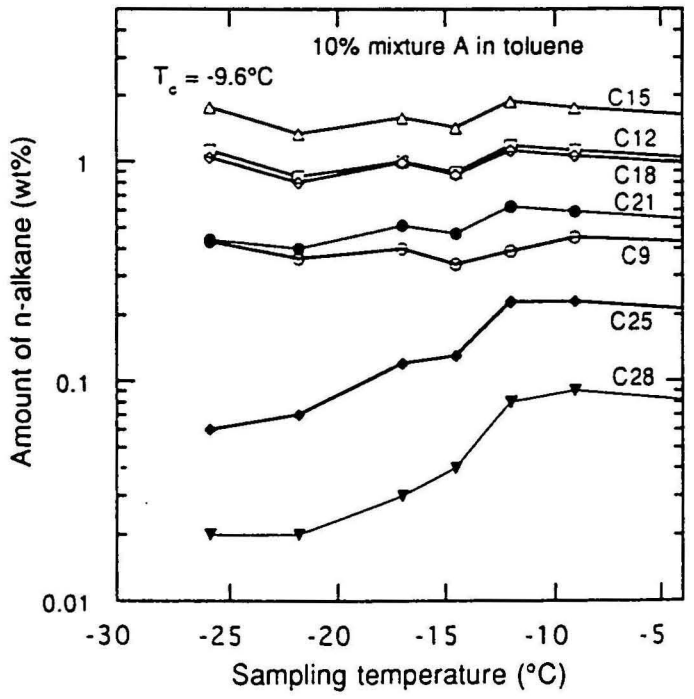

Figure 5.11: The n-alkane content in the liquid phase of 10% solution of mixture A in toluene versus temperature. A: the paraffin distribution; B: concentration of selected individual n-alkanes.

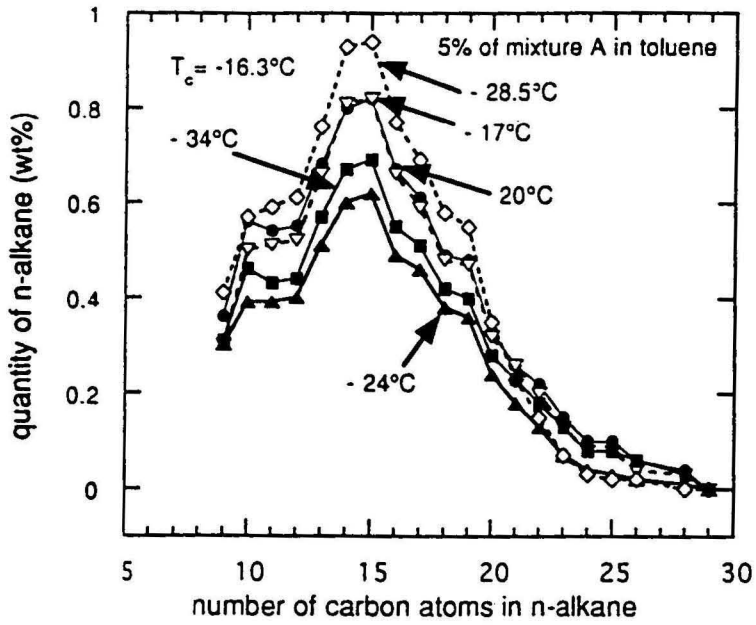

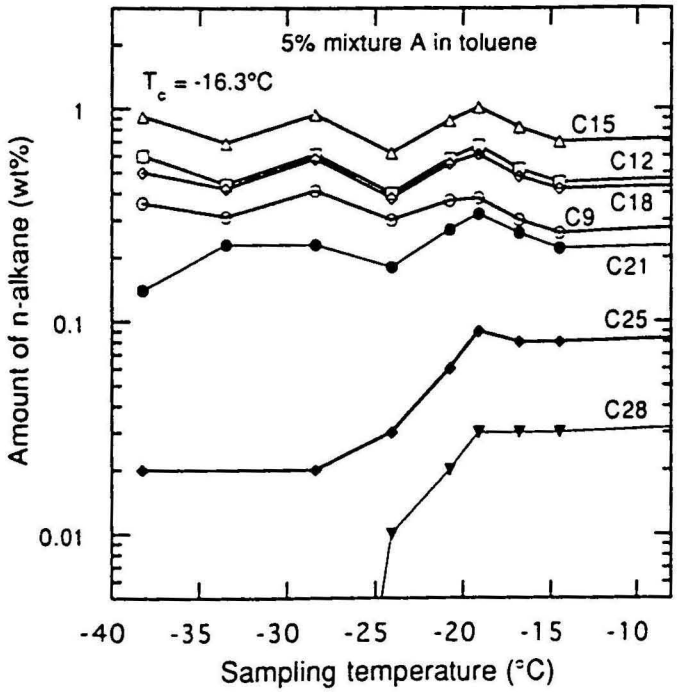

Figure 5.12: The n-alkane content in the liquid phase of 5% solution of mixture A in toluene versus temperature. A: the paraffin distribution; B: concentration of selected individual n-alkanes.

Conclusions

We have used gas chromatography to acquire detailed quantitative data regarding the composition of liquid phase below T_c for two types of model fuels: solutions of mixture A in toluene and in nitrobenzene. Upon solidification, there is a preferential segregation of heavy n-alkanes into the solid phase. This tendency is strongest for the high-concentration nitrobenzene solutions. If the volume fractions of the liquid phase versus temperature were known, the GC data could be converted to the absolute composition of the liquid and solid phase versus temperature. Even in the current form, however, our data can be used to test the thermodynamic models of paraffin solidification in complex systems.

Chapter 6

The effect of additives on the solidification of model fuels

6.1 Background

The crystallisation of waxy components (predominantly higher n-alkanes) out of diesel diesel fuels in winter conditions causes practical problems that affect their transport, storage and use ([43, 44, 45, 46, 47] and the literature cited therein). Below the crystallisation temperature (or the cloud point), T_c, the wax starts to separate from the fuel in the form of very thin rhombic platelets (at full growth about half a millimetre across and 10 micrometres thick). As the temperature drops, these platelets rapidly increase in number and eventually form a continuous, impermeable network that dramatically reduces fuel's ability to flow. At certain yet lower temperature (pour point) the fuel goes jelly and ceases to flow. This latter phenomenon may be triggered by no more than $2wt\%$ of waxy solids separated out of the total fuel mass.

Because of the design of the diesel engine fuel system the consequences of those events start to affect the normal fuel use at some temperature between the cloud point and pour point. More specifically, in order to protect the close mechanical tolerances of the high pressure injection pump there is a 1 micrometre filter installed on the main fuel supply line. If there are enough large crystallites formed in the fuel tank, they can block the filter and, consequently, starve the engine of fuel.

The modern solution to this problem is the use of chemical additives that either lower the wax crystallisation temperature or control crystal growth. Thus, the additives are divided into two general classes: T_c-depressants and flow im-

Table 6.1: General information about the additives studied in this work

Additive name	side chain length (carbon units)	number average molecular mass (polystyrene equiv units)
DB6858	12	40146
DB6860	18	41247
D6861	12	4797
C6862	18	4922

provers [44], sometimes called cold filter plugging point depressants [46].

A significant part of this project has been devoted to the study of T_c-depressant additives and the mechanism by which they lower the crystallisation temperature of model fuels. Four different T_c-depressant additives were supplied in a pure form by Mr. Gateau of the Chimie Appliquee, Biotechnologies, Materiaux division of IFP. The additives were polymethylacrylates of different monomer unit lengths and different molecular masses. Their T_c-suppressing ability in a real diesel fuel was determined using differential scanning calorimetry. The general information supplied with the additives is compiled in table 6.1.

This work was focused on the two lighter polymers, D6861 and C6862, and the most extensive data sets have been accumulated for systems containing these two additives. However, some fragmentary data were acquired also for systems with heavy polymers.

The total paraffin content in a typical diesel fuel is in the range $10-30wt\%$ (13.3% in Fuel A, 15.1% in Fuel B). In the industrial practice the amount of additive added to a fuel varies from 50 to 250 ppm. Therefore, our work was concentrated on the solutions of 10% and 20% of mixture A in toluene and nitrobenzene. For completeness of data the additive concentration range 0−3000 ppm was studied.

We have used two major experimental tools: determination of T_c using direct observation in polarized light and the Small Angle Neutron Scattering (SANS). These measurements were performed both for the binary mixtures of additives with deuterated toluene and in ternary solutions of deuterated toluene, mixture A and additive.

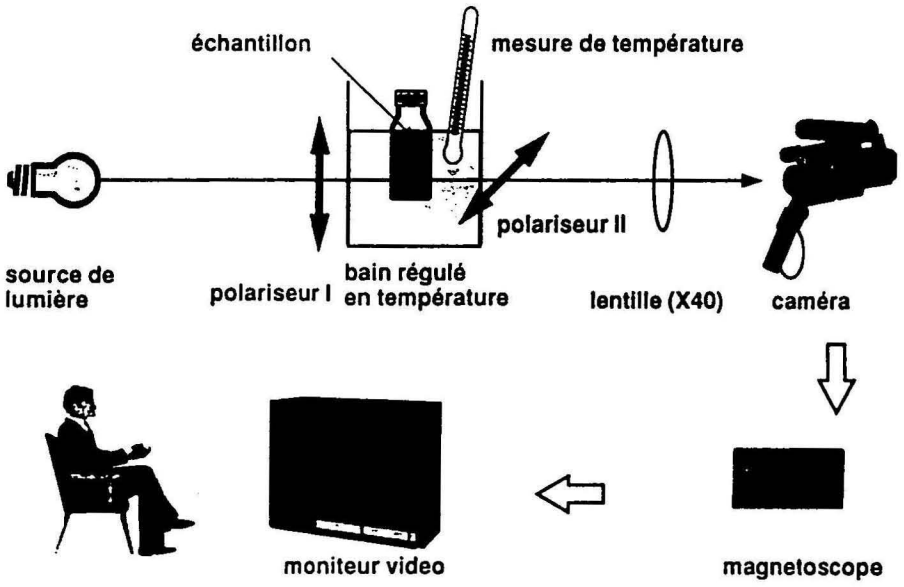

Figure 6.1: A schematic diagram of an experimental arrangement for optical observation of crystallisation.

6.2 Experimental set-up for optical observations of crystallisation

All data regarding the temperatures of crystallisation in fuels and model fuels presented in this work were obtained using an experimental arrangement specifically designed for this purpose. Basically, a transparent sample container was maintained in a controlled temperature environment and observed between crossed polarisers in transmitted light using a video camera equipped with a 40x photographic macro lens (figure 6.1).

The crystallisation images could be recorded on a video tape for further analysis. A photograph of the system is shown in figure 6.2.

Although the basic design of our system is similar to that of a cold-stage polarisation microscope of low magnification, there are important differences. Because of the relatively large focal length of the focusing lens, different temperature-controlled sample holders can be used. Consequently, we have been able to observe the crystallisation process in containers of various shapes and sizes. Typically, we have been using either 1 mm diameter X-ray glass capillaries or

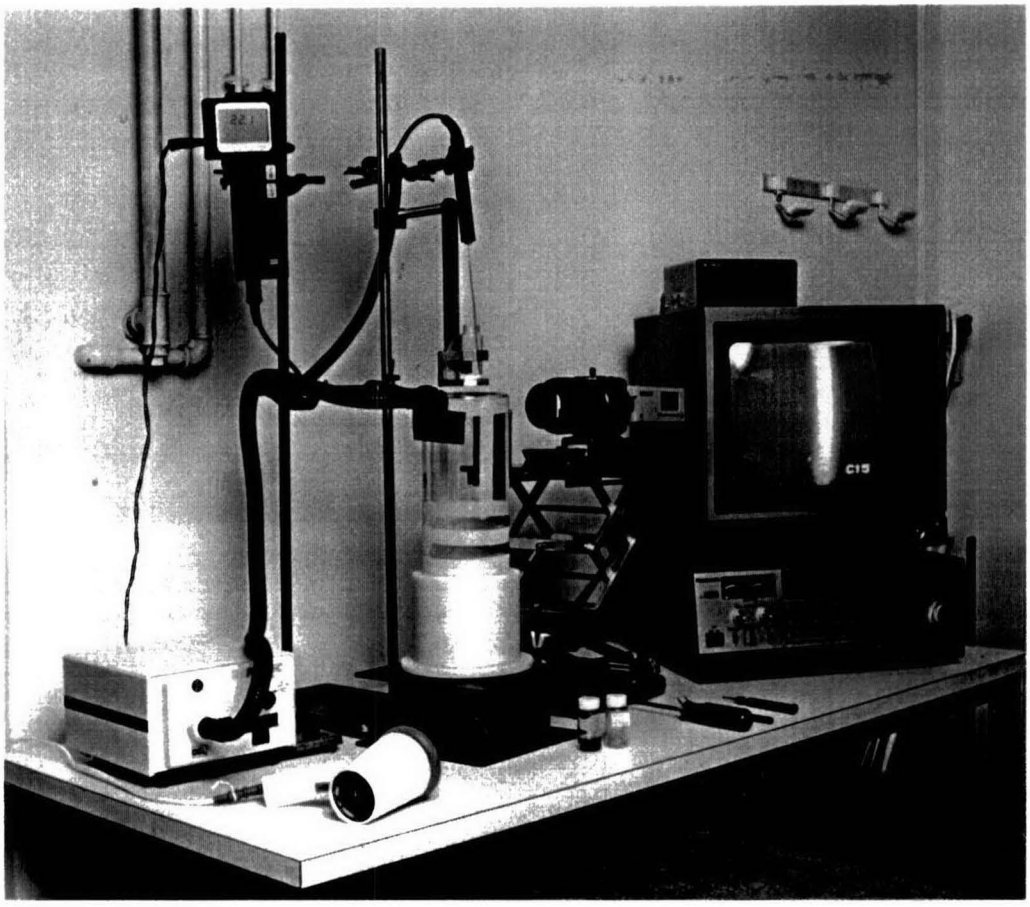

Figure 6.2: The experimental arrangement for optical observation of crystallisation.

20 ml glass bottles (so-called scintillation bottles). The possibility to employ the X-ray capillaries is advantageous for correlating the X-ray and optical observation results for the same sample. On the other hand, the use of bottles enabled us to observe the crystallisation process in a relatively large volume with a possibility of sampling the liquid phase under direct optical surveillance.

The temperature is controlled either using an externally-circulated thermal bath (temperature range from 10°C to 80°C) or by positioning the bottle in a glass cryostat partially filled with liquid nitrogen. In the latter case there is a temperature gradient inside the cryostat from 78 K (- 195°C) at the surface of the liquid to about 20°C at the top of the cryostat. The temperature of the sample is continuously monitored and can be controlled by adjusting the vertical position of the cryostat. The liquid inside the bottle can be easily sampled for further analysis since the bottle is maintained in the neutral atmosphere of dry nitrogen gas and there is no water condensation.

6.3 The morphology of paraffin solidification

The morphology of solid phase during crystallisation, both for solutions with and without additives, has been recorded using the optical arrangement for observation in polarized light described in the previous chapter. It is necessary to remind the reader that this arrangement offers the maximum magnification of 40x, which results in the linear resolution of about 10 micrometres. Therefore, this technique provides no information about the individual crystallites smaller than 10 micrometres, for which purpose the optical microscopy and electron microscopy are best suited. However, unlike the optical polarisation microscopy or electron microscopy, our technique enables one to follow in situ the general pattern of paraffin crystallisation in a large volume sample.

As discussed in the previous section, the fuel samples were contained either in 1 to 2 mm diameter X-ray capillaries or 20 ml glass bottles. As illustrated below, the crystallisation of same system may look different if different diameter containers are used. In general, a capillary filled with a liquid acts as a cylindrical lens and the optical image is deformed. Also, the role of surface-nucleated crystallisation may be much more pronounced in capillaries than in bottles. However, the SAXS studies are routinely performed in glass capillaries and it is sometimes advantageous to observe the crystallisation using the same container (and sample holder) as in the X-ray studies. In the following fifteen plates we present the snapshots of video recordings of different systems: diesel fuel Fuel A, pure n-alkane solutions in toluene and nitrobenzene, and mixture A solutions in toluene and nitrobezene with and without additives. The purpose is mostly illustrative as no structural information in the most interesting crystal size region 1 to 10 micrometres can be obtained from these micrographs. In order to really appreciate the sensitivity of the method it is best to watch the original video recordings. The micrographs shown below have been taken from

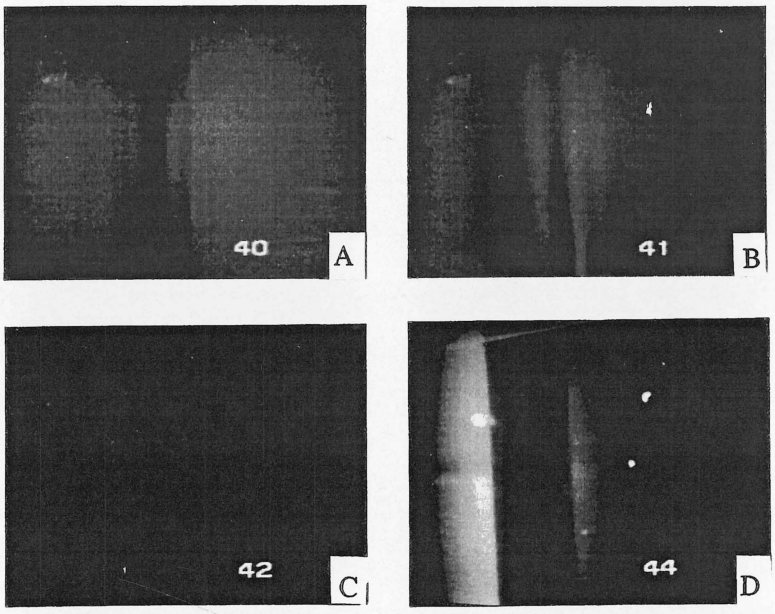

Figure 6.3: Optical micrographs of n-alkane crystallisation in nitrobenzene solutions: (A) 20% C10, (B) 10% C15 + 10% C16, (C) 20% C16 and (D) 20% C20. The vertical shadow is the image of a 1 mm diameter thermocouple jacket.

one to five minute duration recordings covering temperature intervals of several degrees in the vicinity of the corresponding crystallisation temperature.

Figure 6.3 illustrates the onset of crystallisation in four nitrobenzene solutions of pure paraffins, from C10 to C20. The evolution of crystallisation process for the heaviest paraffin in the series, C28, is shown separately in figure 6.4.

The trend is clear: the light paraffins form very small crystallites, visible as fine mist, whereas C20 and C28 produce much larger, optically active crystals. The crystallisation process of C28 is truly spectacular. The dark, elongated and nearly vertical shadow visible in all the micrographs is the image of a 1 mm diameter thermocouple jacket immersed in the bottle which also serves as a scale marker.

Figure 6.5 shows crystallisation of C15 in nitrobenzene. This is an interesting example, since the crystal structure of C15 just below the crystallisation temperature is hexagonal and does not exhibit the optical activity.

The micrographs show a slightly conical section of glass capillary fixed in a SAXS temperature-controlled sample holder. In order to make the sample

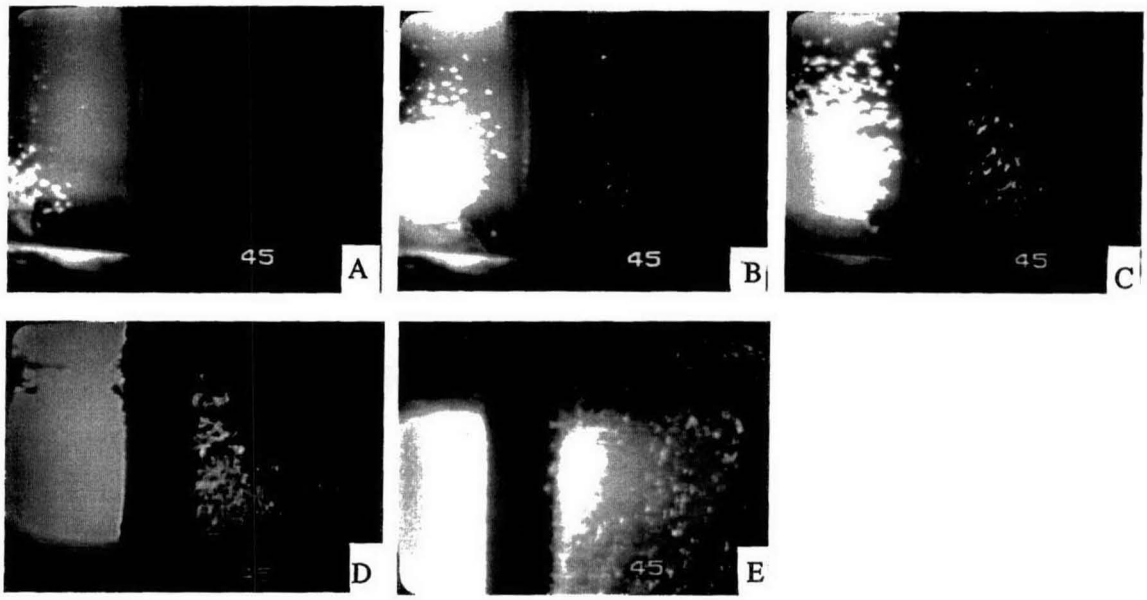

Figure 6.4: The optical record of time sequence of the C28 n-alkane crystallisation in a 20% nitrobenzene solution: (A), (B), (C), (D) and (E) correspond to the consecutive stages of crystallisation as the temperature decreases by about 2 degrees. The crystallisation temperature is 55.1°C. The vertical shadow is the image of 1 mm diameter thermocouple jacket.

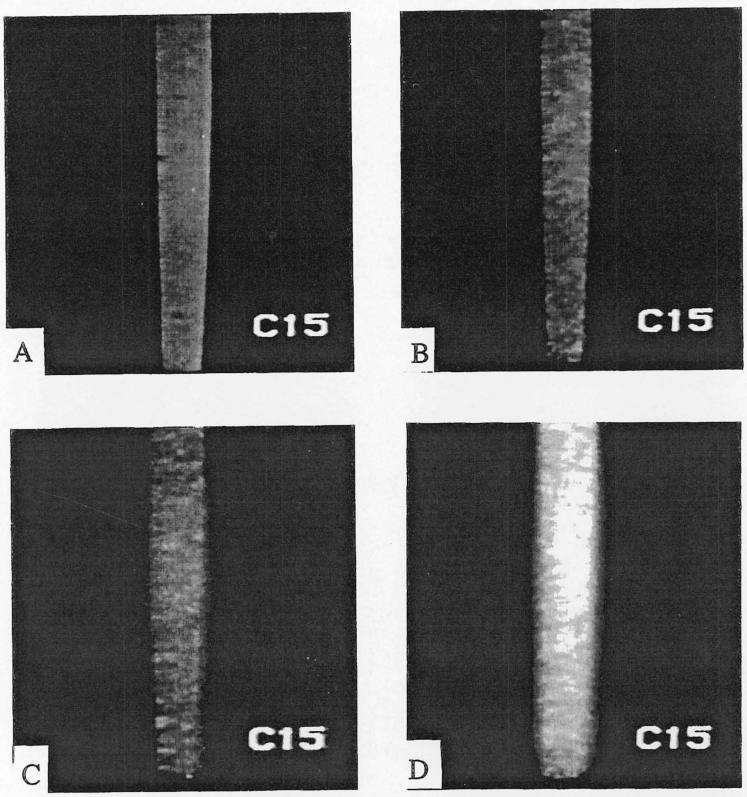

Figure 6.5: The optical record of time sequence of the C15 n-alkane crystallisation in a 20% nitrobenzene solution: (A), (B), (C) and (D) correspond to the consecutive stages of crystallisation as the temperature decreases. Note the increased crystallite brightness in micrograph (D).

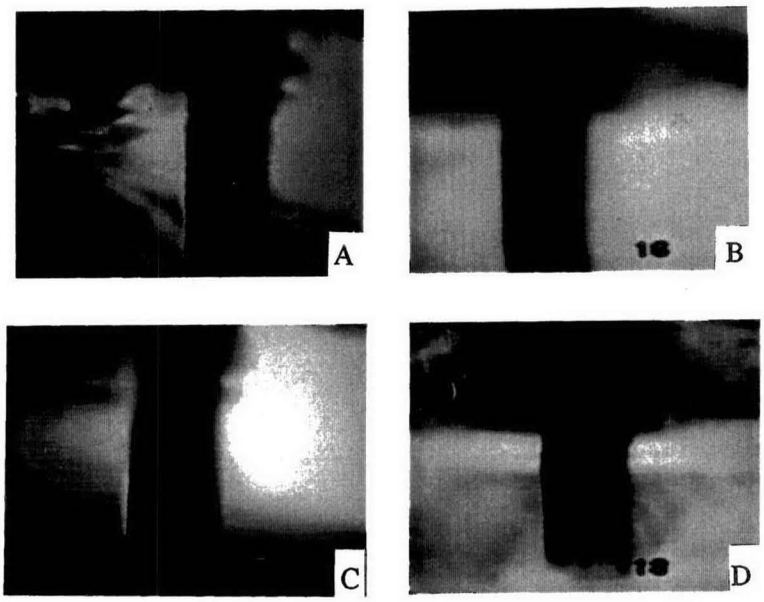

Figure 6.6: The crystallisation pattern for various toluene solutions of C20 and C28 n-alkanes: (A) 5% solution of C20, (B) 20% solution of C20, (C) 5% solution of C28, and (D) 10% solution of C28.

visible, the polarisers are not exactly crossed. Micrograph A shows the capillary prior to the onset of crystallisation. The mottled structure visible in B and C is caused by shadows of many fine, optically inactive crystals. Image D was taken just after the hexagonal-orthorombic phase transition, which appears instanteneous on the video recording. As the latter phase is optically active, image D is much brighter than both B or C.

In figures 6.6, 6.7 and 6.8 we show a series of crystallisation images of pure n-alkanes in toluene solutions. The images for C20 and C28 in the first of the figures show some structure, but the crystallites appear to be very fine.

The series of micrographs for the 10% solution of C20 (figure 6.7) is a record of a spectacular needle-like crystal growth process.

Figure 6.8 documents the early stages of crystallisation for a number of concentrations of C15 in toluene in the range $2 - 80\%$. For the concentrations below 20% (images D, E, F and G) there is an indication of a webby large-scale structure being formed, which may be the initial stage of gel formation. Figure 6.9 shows the onset of wax crystallisation in the diesel fuel Fuel A filtered

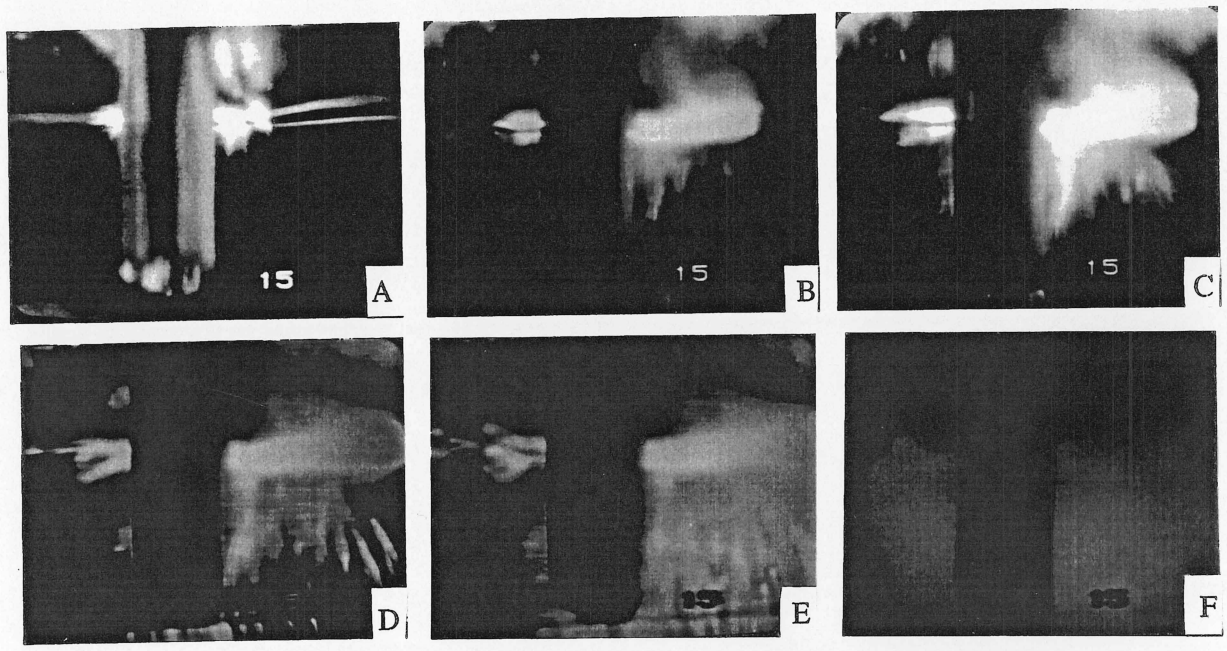

Figure 6.7: The optical record of the time sequence for the crystallisation of C20 n-alkane in a 10% deuterated toluene solution (temperature decreasing from (A) to (F)). The micrographs cover time span of about 30 sec and the temperature decrease is about 1 degree.

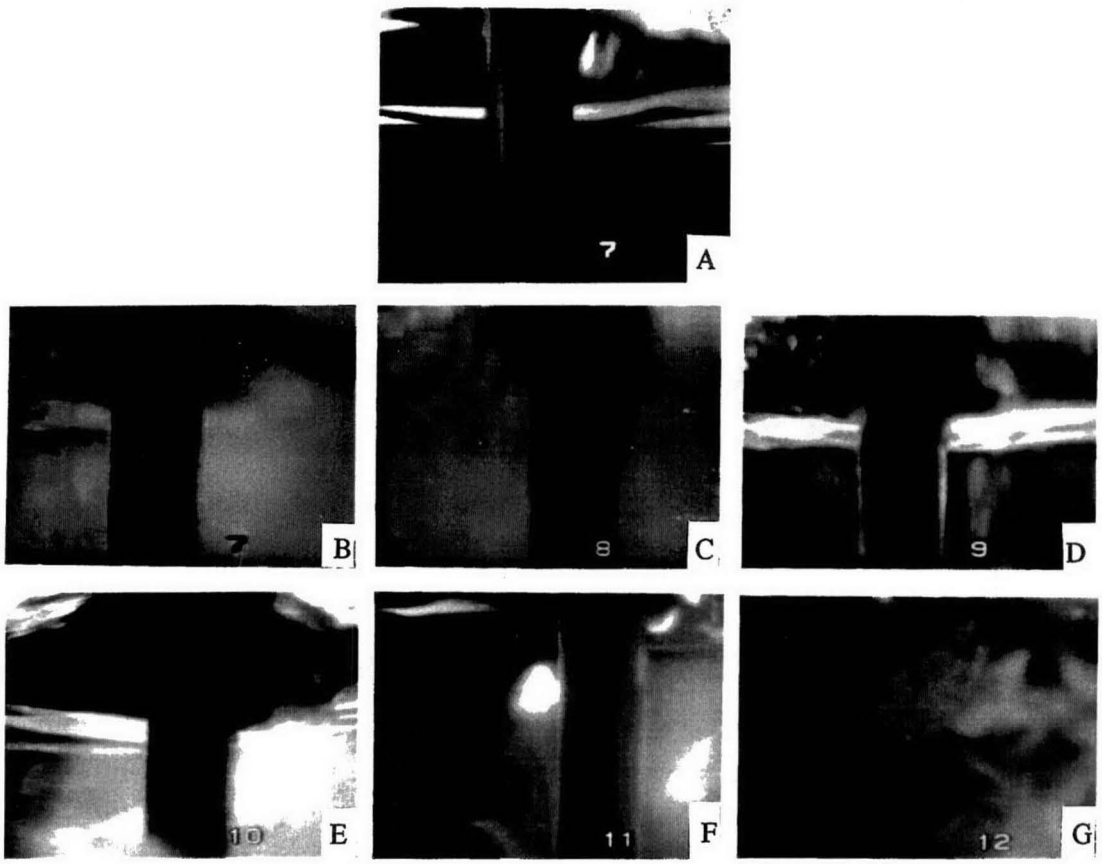

Figure 6.8: The early stage of crystallisation for several solutions of C15 in deuterated toluene: (A) 80% solution above the crystallisation temperature, (B) 80% solution, (C) 40% solution, (D) 20% solution, (E) 10% solution, (F) 5% solution and (G) 2% solution.

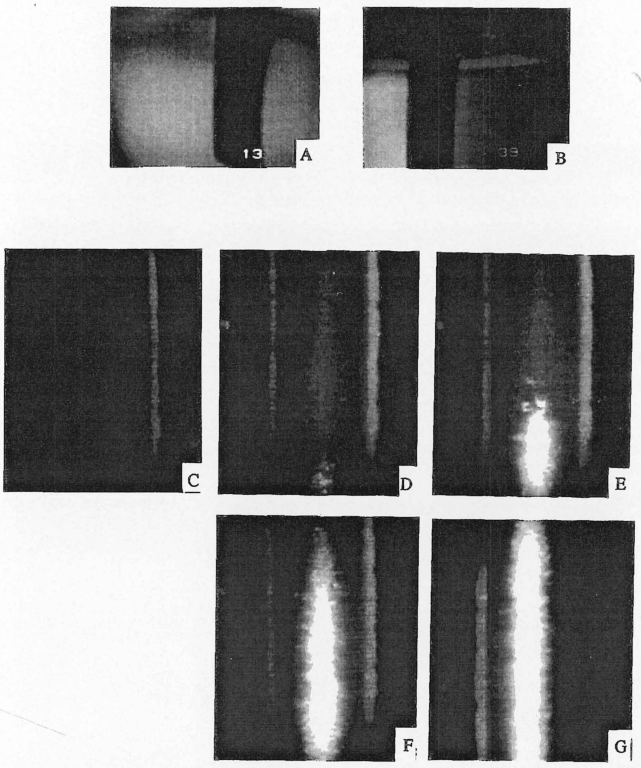

Figure 6.9: The early stage of crystallisation for (A) diesel fuel Fuel A filtered with a 1 micrometre filter and (B) Fuel A as obtained, both observed in a bottle. (C) to (G): the evolution of crystallisation pattern of Fuel A observed in a capillary.

through a 1 micrometre filter (image A), as obtained (image B) and the evolution of crystals in as-obtained Fuel A observed in a capillary (images C to G). Because of the design of the sample holder the capillary is most efficiently cooled from below and, consequently, the crystals first appear at the bottom. It is interesting to note that the capillary images suggest a presence of large crystallites, which is not apparent for the fuel contained in a bottle (images A and B). This is an illustration of either the optical distortion caused by the small diameter of capillary, or the container size effect, or both. The crystallisation temperature is in both cases the same within the experimental error.

The remaining figures illustrate crystallisation of various solutions containing mixture A of paraffins. In figure 6.10 the final crystallisation patterns (observed in capillaries) for concentrations from pure A (image A) to 2% in toluene (image D) are compared. It is apparent that the concentration of bright spots in the image is positively correlated with the amount of mixture A in the solution. However, in the view of the results for Fuel A discussed above (figure 6.9) it is

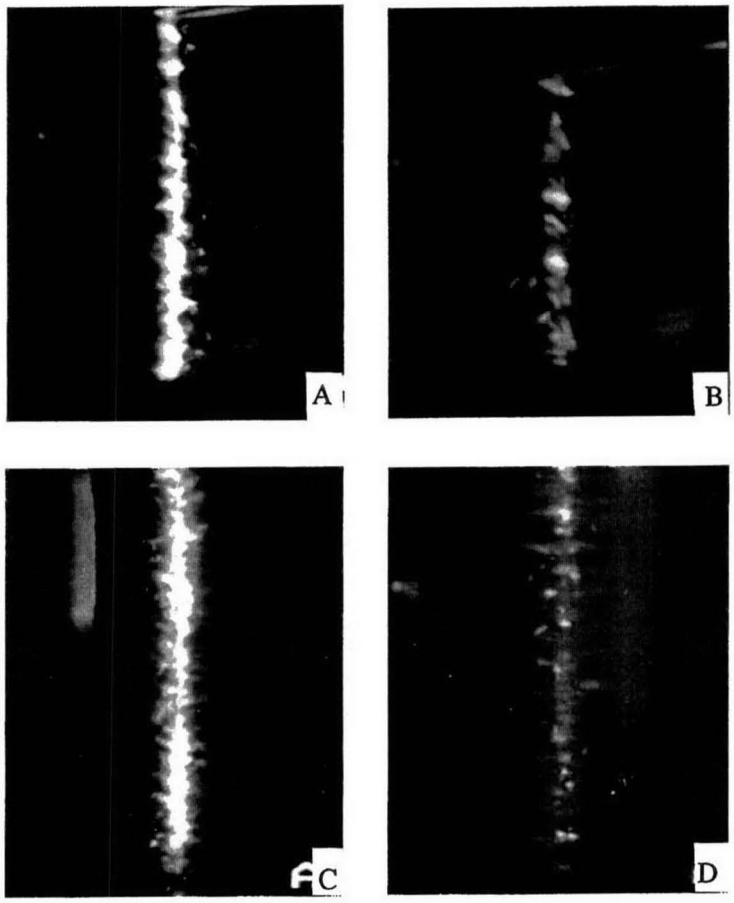

Figure 6.10: The final crystallisation pattern observed in capillaries for: (A) pure mixture A of paraffins, (B) 10% of mixture A in nitrobenzene, (C) 20% of mixture A in toluene and (D) 2% of mixture A in toluene.

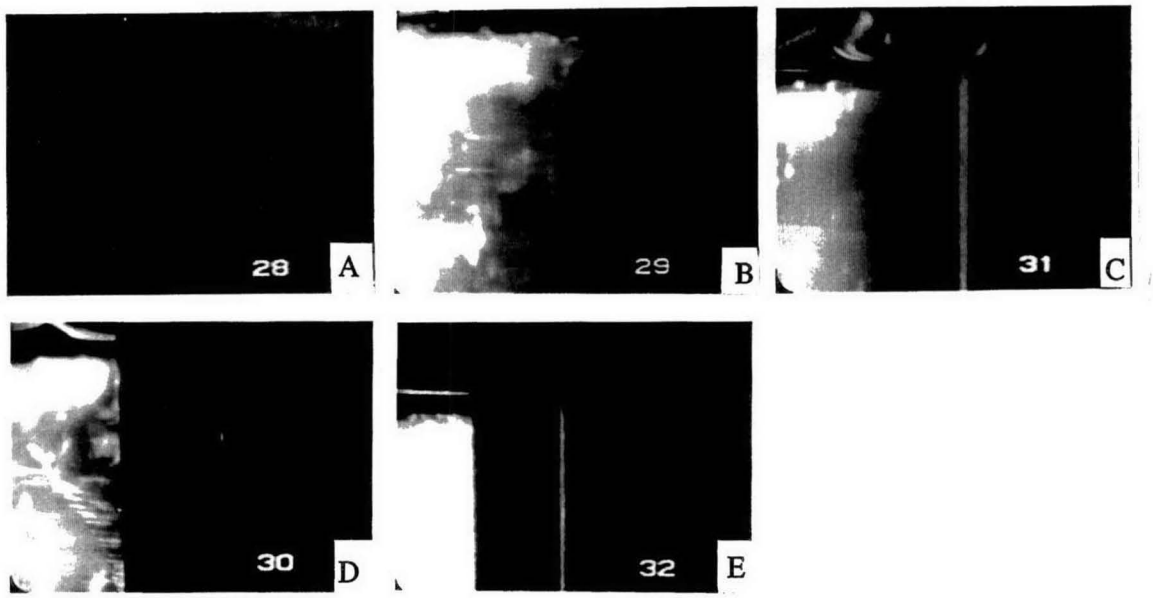

Figure 6.11: The early crystallisation patterns observed in bottles for several concentrations of mixture A of paraffins in nitrobenzene: (A) 20%, (B) 15%, (C) 10%, (D) 5% and (E) 2%.

a contentious issue whether these spots are true images of macroscopic crystals.

Figure 6.11 shows a comparison of the early stages of crystallisation for several solutions of mixture A in nitrobenzene in the concentration range 2% to 20%. There is an indication of large crystallites being formed in those systems. The formation and evolution of those crystallites upon cooling is illustrated in figure 6.12 for the 15% solution.

Finally, the early stages of crystallisation of mixture A in toluene in the concentration range 2% to 80% are illustrated in figure 6.13. Very fine crystallites are only formed, resulting in the mist-like appearance of the optically active solid phase.

Figure 6.14 gives a summary of the crystallisation images for the 20% solutions of mixture A in nitrobenzene containing four different additives: C6862 (A to C), DB6858 (D), DB6860 (E) and D6861 (F). The concentration of additives in B, D, E and F is close to 300 ppm. In this particular case the micrographs are substantially inferior in their information content to the video recordings, in which one can observe a fine structure composed of a system of very thin

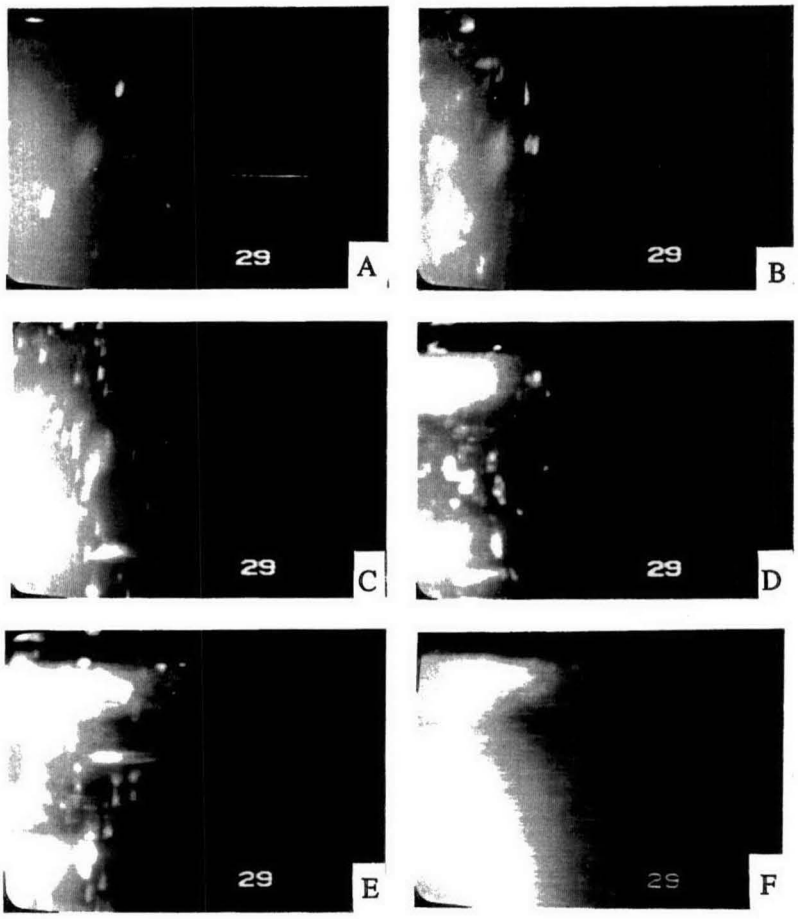

Figure 6.12: The evolution of crystallisation pattern for a 15% solution of mixture A in nitrobenzene. Micrographs (A) to (F) correspond to the temperature decrease of about 2 degrees and were recorded in the time span of about two minutes.

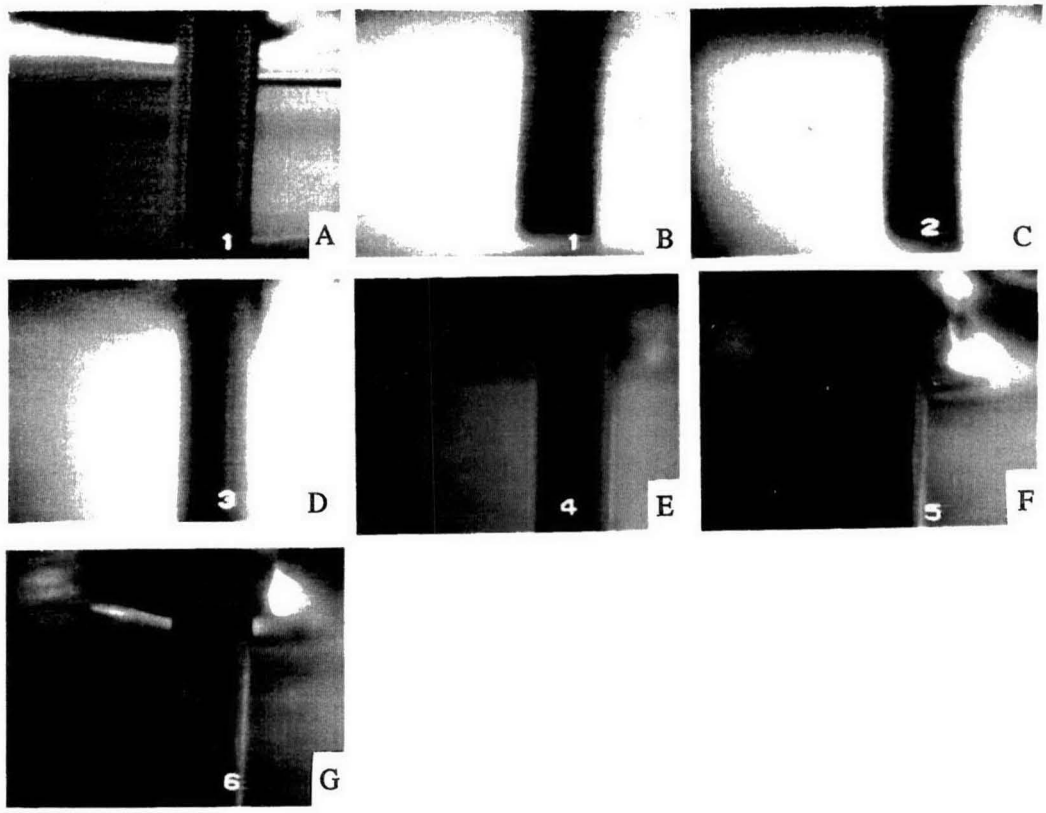

Figure 6.13: The early crystallisation patterns observed in bottles for several concentrations of mixture A of paraffins in deuterated toluene:(A) the 80% solution above the crystallisation temperature, (B) 80% solution, (C) 40% solution, (D) 20% solution, (E) 10% solution, (F) 5% solution and (G) 2% solution.

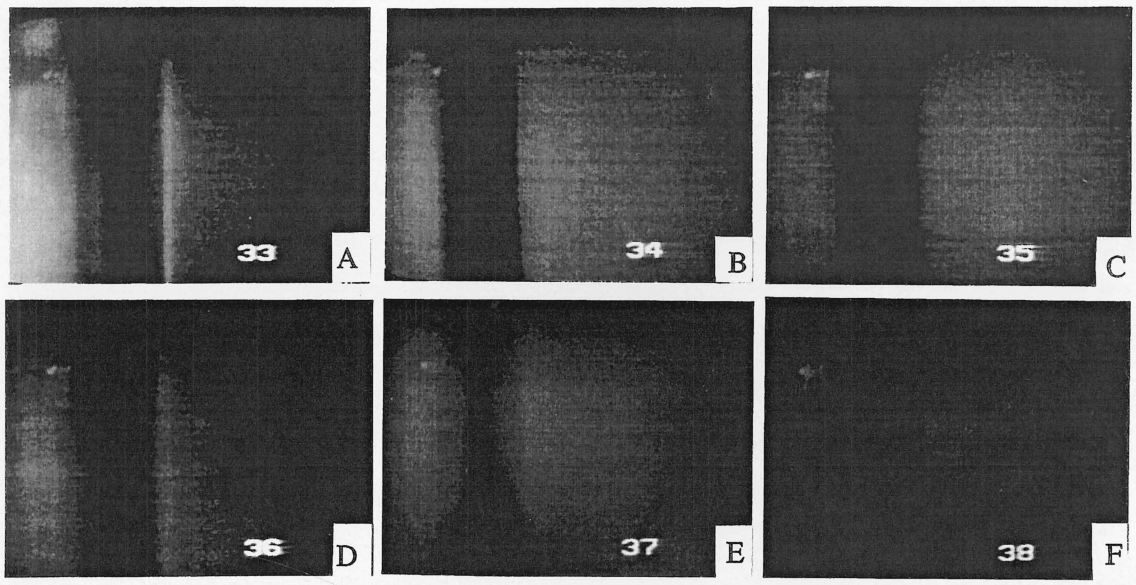

Figure 6.14: A summary of the crystallisation images for the solutions of 20% mixture A in nitrobenzene containing four different additives: (A) 103 ppm of C6862, (B) 297 ppm of C6862, (C) 1043 ppm of C6862, (D) 283 ppm of DB6858, (E) 305 ppm of DB6860, and (F) 286 ppm of D6861.

vertical and horizontal lines slowly and independently moving across the screen. We note that this crystallisation mode is distinctly different from that observed for pure mixture A in nitrobenzene (see figures 6.11 and 6.12).

A detailed comparison of the crystallisation images for mixture A with three different additives in toluene solutions are presented in figures 6.15, 6.16 and 6.17. As for the nitrobenzene solutions, the horizontal/vertical fine structure is present there. It is perhaps best visible for the additive C6862 (micrographs B and C in figure 6.15). The crystallisation mode (fine mist) observed for the remaining two additives appears to be similar to that found in the toluene solutions without additives (figure 6.13).

Even a casual perusal of the above crystallisation images indicates that there is a rich variety of nearly macroscopic structures formed during the paraffin crystallisation process in different solvents, both with and without additives. The video technique, combined with large volume samples in which the movement of solid particles is possible over relatively large temperature intervals (which

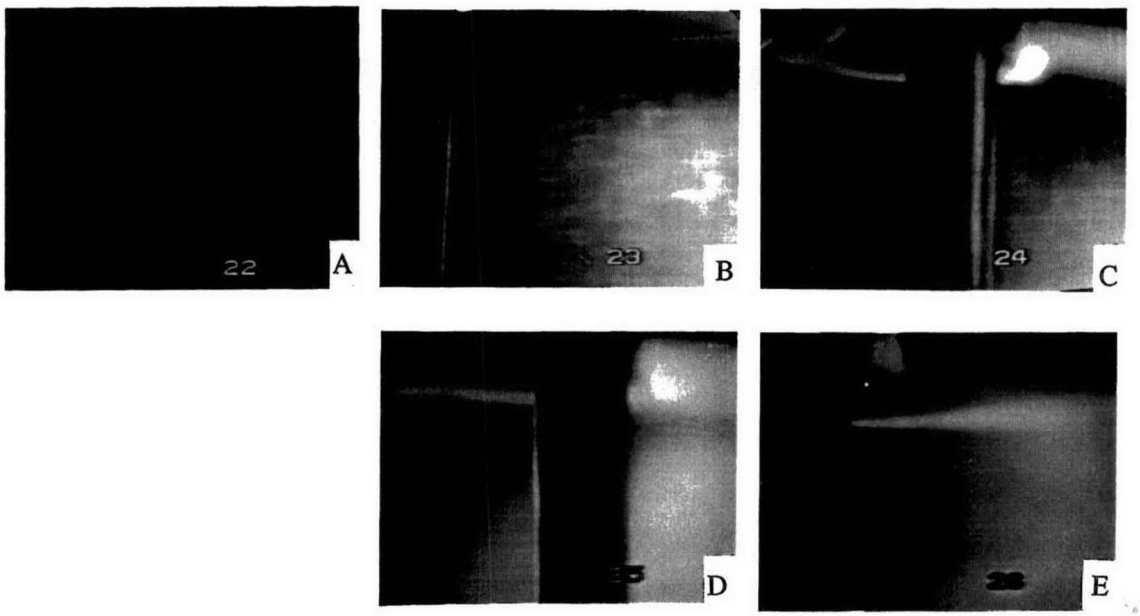

Figure 6.15: Crystallisation images for the solutions of 20% mixture A in toluene containing additive C6862: (A) 90 ppm of the additive, (B) 240 ppm, (C) 525 ppm, (D) 1025 ppm and (E) 3116 ppm.

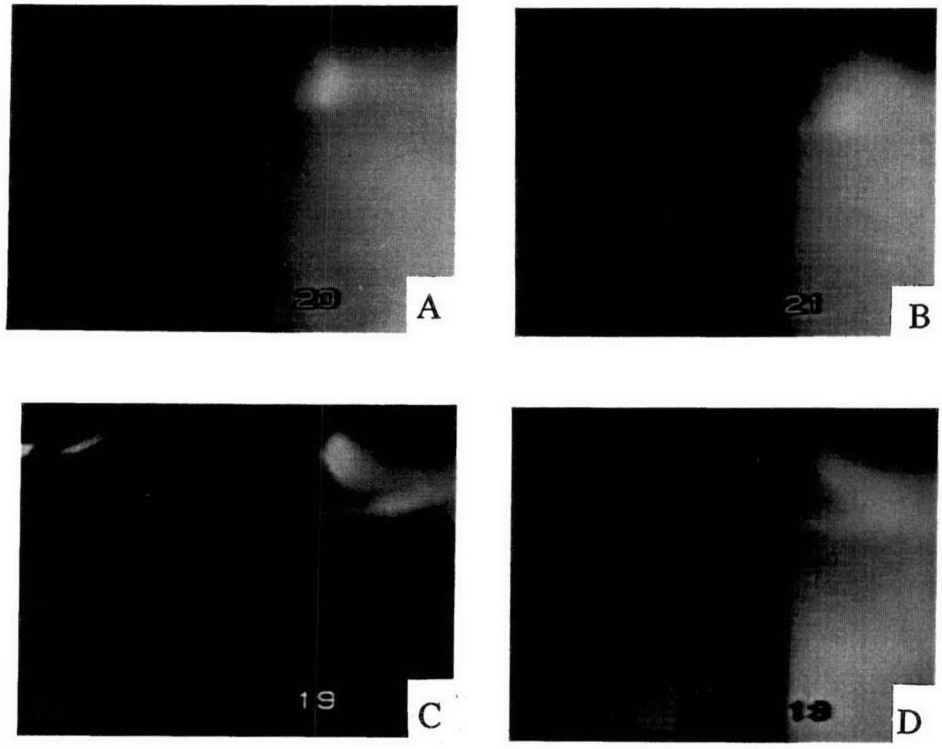

Figure 6.16: Crystallisation images for the solutions of 20% mixture A in toluene containing additive D6861: (A) 575 ppm of the additive, (B) 1200 ppm, (C) and (D) 2720 ppm in the beginning and towards the end of crystallisation, respectively.

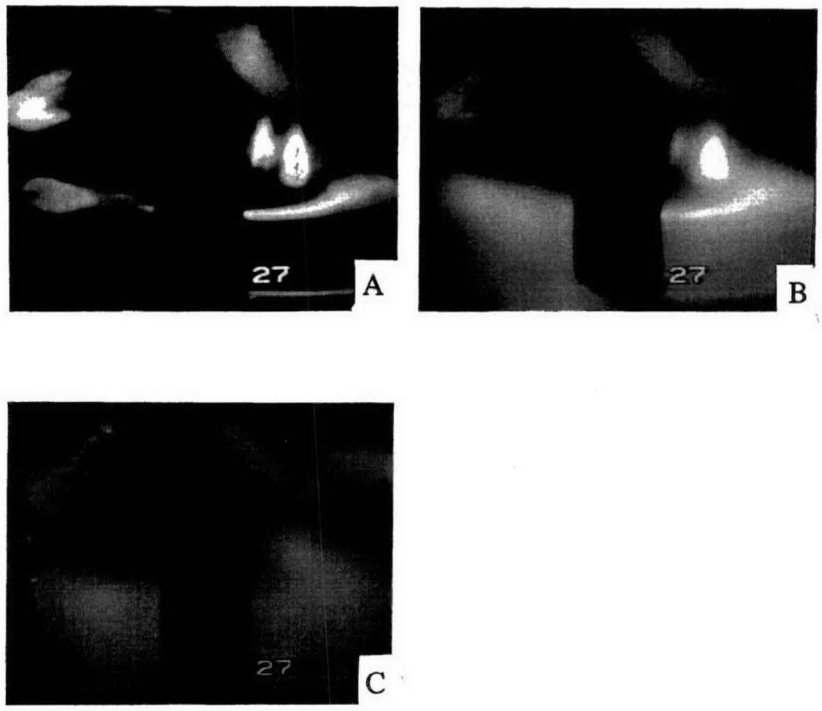

Figure 6.17: Three consecutive crystallisation images for the solution of 20% mixture A in toluene containing 4416 ppm of additive DB6858 obtained in a short time interval during sample coolinge. A meniscus formed around the thermocouple jacket is well visible.

remains in contrast to the polarisation microscopy) enables one to observe the dynamics of the bulk crystallisation process: the growth of first crystallites, development of interconnected network of the solid phase and, eventually, the total solidification, either in the form of crystals, or gel, or both. We have not pursued this aspect of our technique in any detail owing to the character of the additives studied here (T_c-depressants), but the fragmentary observations we have made prove that this sort of structural studies could be in principle performed with our equipment.

The additive-induced change of appearance of the precipitated solid phase is the first indication of the polymer-paraffin interaction at the molecular level. Little can be said about this process on the basis of the optical observations of crystallisation alone, but one can anticipate that the specific solidification scenario should depend both on the additive and solvent.

6.4 The analysis of additive effectiveness based on T_c data

T_c data for the nitrobenzene and toluene solutions of mixture A with various additives are presented in figures 6.18 and 6.19, respectively. These are the so-called response curves of fuel to different additives [47]. Data for the light additives show that for C6862 T_c initially drops quickly with the increased concentration of additive and reaches a plateau at about 1000 ppm, independently of the solvent, whereas for D6861 the decrease of T_c is much less pronounced and nearly linear in both solvents. There are only two experimental points for the heavy additives, both in nitrobenzene.

One notes that the effect obtained (i.e. the decrease of solidification temperature measured, for instance, at the near-saturation concentration of 1000 ppm of additive) varies widely from one system to another. For instance, it is 0.5°C for D6861 in the the 20% nitrobenzene solutions and 8.5°C for C6862 in the the 20% toluene solution. Even for the same additive (for instance, C6862) the maximum effect is 1.1°C in nitrobenzene and 8.5°C in toluene. Comparisons can be also made with data obtained by calorimetry for a diesel fuel containing 150 ppm of additive (table 6.2). The observed magnitudes of T_c decrease are: 1.2°C (diesel fuel), 0.3°C (20% of mixture A in nitrobenzene) and 0.05°C (20% of A in toluene) for D6861 and 3.1°C, 1.0°C and 1.5°C, respectively, for C6862.

Quite clearly, the net effect of the same additive may be quite different for different systems. Therefore, in order to be able to make meaningful comparisons between different systems there is a need to work out an universal approach that would enable one to judge the additive action at the molecular level rather than solely in terms of the T_c decrease. Although a large magnitude of T_c drop may be the only desired practical outcome of using an additive, its underlaying cause can be only understood along the lines of molecular-level models.

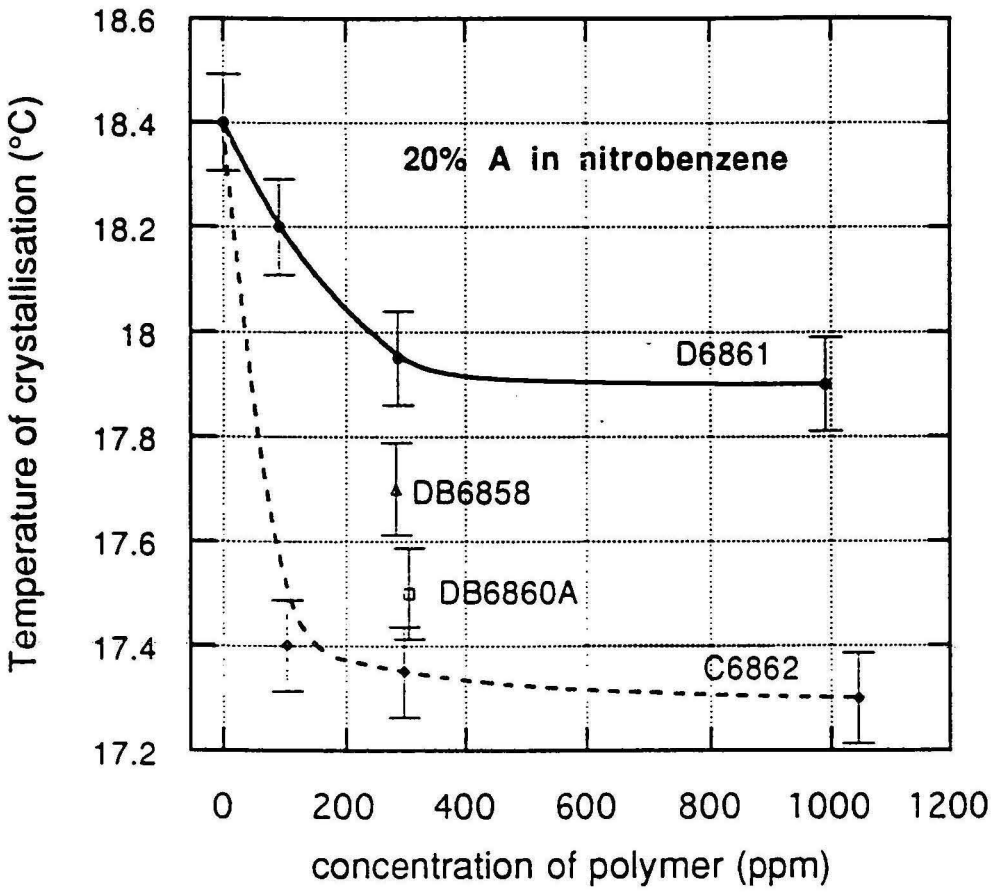

Figure 6.18: The response curves for the two light additives, D6861 and C6862, in the 20% solution of mixture A in nitrobenzene. Two experimental points corresponding to the two heavy additives, DB6858 and DB6860, respectively, at the concentration about 300 ppm are also shown.

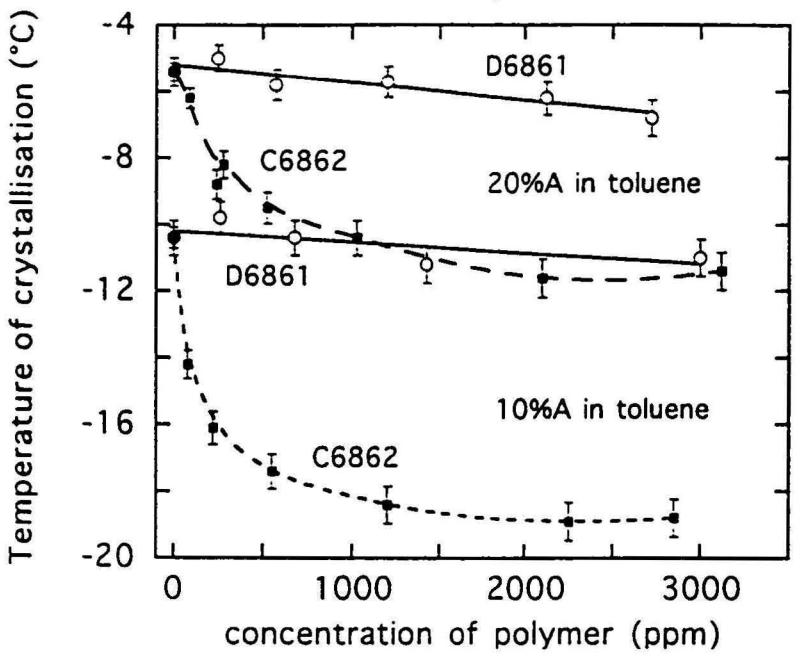

Figure 6.19: The response curves for the two light additives, D6861 and C6862, in the 20% and 10% solutions of mixture A in toluene.

Table 6.2: The paraffin crystallisation temperature T_c (in oC) for various systems. The concentration of additive was 150 ppm for all cases. Value for the (commercial) diesel fuel was obtained using Differential Scanning Calorimetry, other data by optical means.

Additive name	diesel fuel	20% of mixture A in nitrobenzene	20% of mixture A in toluene	10% of mixture A in toluene
none	−8.0	18.4	−5.4	−10.4
DB6858	−8.9	17.9	no data	no data
DB6860	−10.5	17.8	no data	no data
D6861	−9.2	18.1	−5.3	−10.1
C6862	−11.1	17.4	−7.0	−15.1

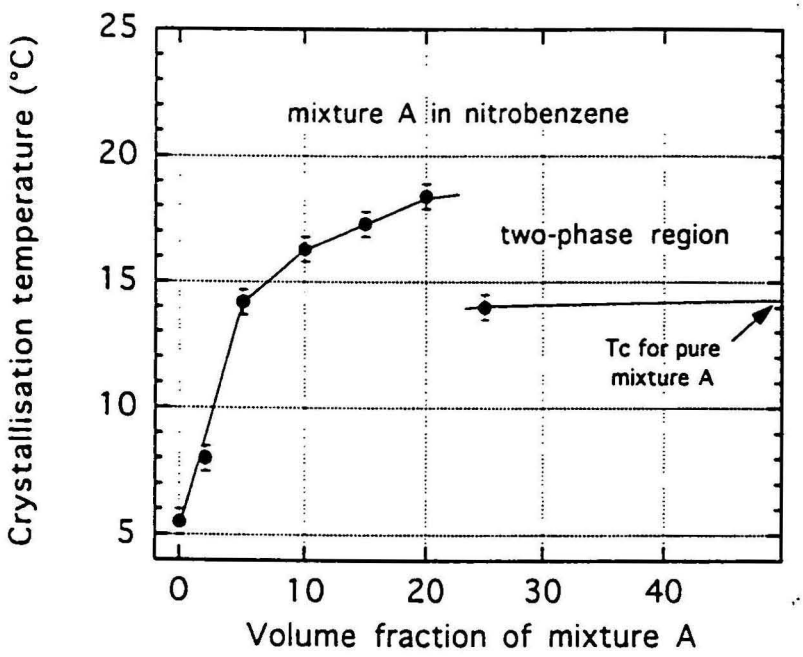

Figure 6.20: The liquidus line for the mixture A - nitrobenzene pseudo-binary system. The crystallisation temperatures have been determined by optical means. Note that the system becomes two-phase at the paraffin volume fraction above 20%.

One can try to quantify the effect of paraffin-additive interaction solely on the basis of T_c experimental data and without specifying the molecular mechanisms in action. The only assumption is that a decrease of T_c upon addition of a polymer is caused by the polymer molecules eliminating a proportion of paraffin molecules from taking part in the solidification process, for instance by forming regions of increased paraffin concentration in the vicinity of polymer molecules. At this point we leave the question of how exactly is that done aside. We will return to this question in the next section.

From the additive-free T_c versus mixture A concentration data (figure 6.20) and Figure 6.21) one can find the paraffin concentration that corresponds to a given value of T_c for both the toluene and nitrobenzene solutions. By taking the value of T_c measured for the corresponding solution with an additive (figures 6.18 and 6.19), the weight percentage of mixture A eliminated by a given ppm amount of an additive can be found. These values may be quite impressive: for instance, in the solution of $10wt\%$ of mixture A in toluene the amount of 80 ppm

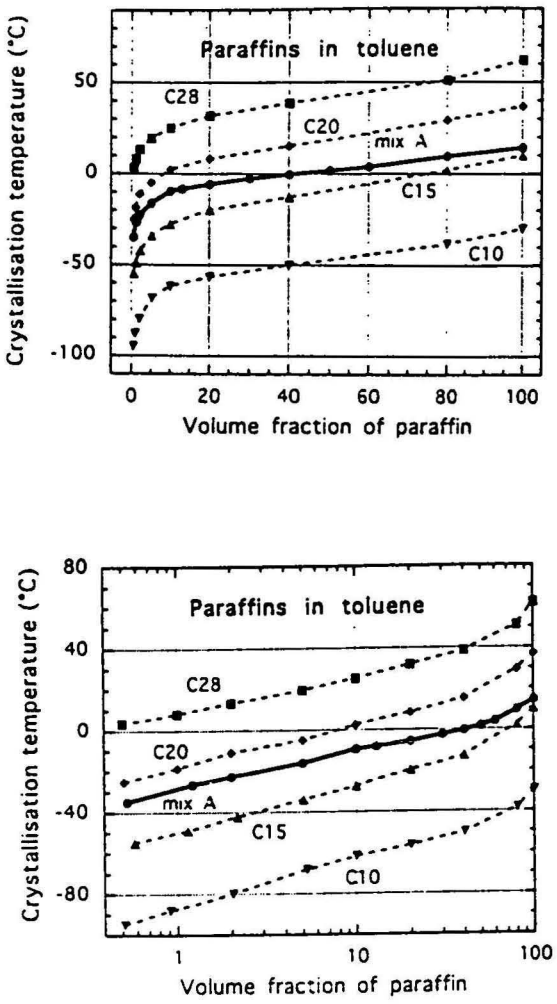

Figure 6.21: The liquidus lines for the binary solutions of several n-alkanes in toluene and for the mixture A - toluene pseudo-binary system. The crystallisation temperatures have been determined by optical means. (A) and (B): linear and logarithmic paraffin volume fraction scale, respectively. On the logarithmic scale, note the different slope for the mixture A curve.

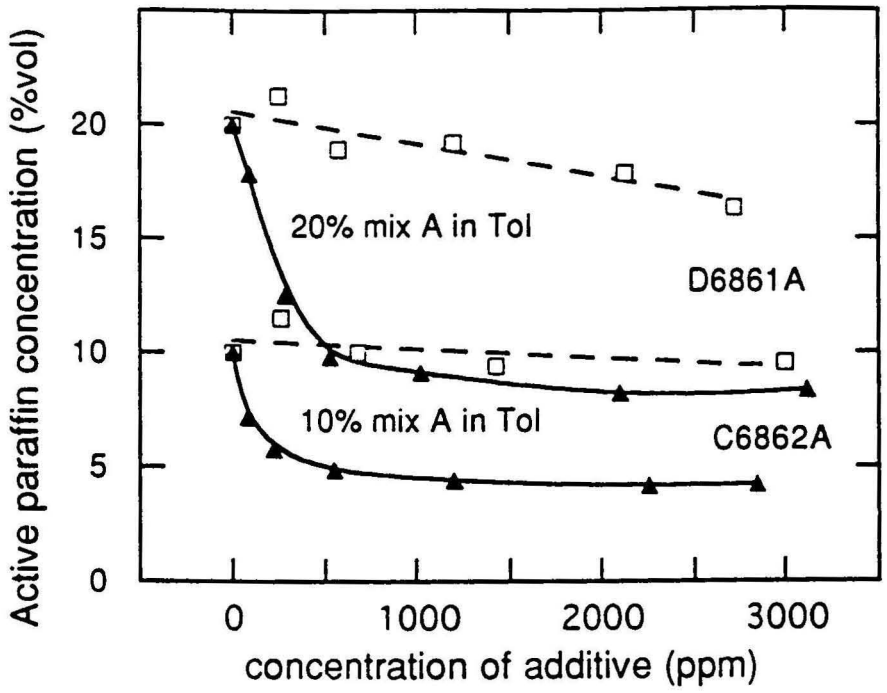

Figure 6.22: The paraffin concentration that remains active in the crystallisation process after the additive has been added versus the additive concentration for the two light additives, D6861 and C6862, in the 10% and 20% solutions of mixture A in toluene. The points have been calculated following the procedure described in the text. Lines are guide for the eye only.

of C6862 eliminates about $3wt\%$ of paraffin (figure 6.22). Since the chemical formulae of both the paraffins and additives used by us are known, these data can be explicitly expressed in terms of the average number of paraffin molecules (of mixture A) eliminated by a single polymer molecule. We define this quantity as the paraffin-to-polymer molecular ratio, abbreviated PPMR.

It is important to realise that both the mixture A and additive distributions are polydisperse, the former by its very nature of being a mixture of 21 normal alkanes of molecular weights in the range $114 - 394$ g/mole and the latter owing to the technological process used for the polymer synthesis. We show below using SANS results that the light polymer polydispersity, $\frac{M_w}{M_n}$, is 1.6 for C6862 and 3.0 for D6861. Data for the plots below were calculated using the average molecular weight for mixture A of 230 g/mole, which is close to the molecular weight of the most abundant n-alkane, C16. For the additives, the supplied values of M_n (Table 6.1) determined by size exclusion chromatography

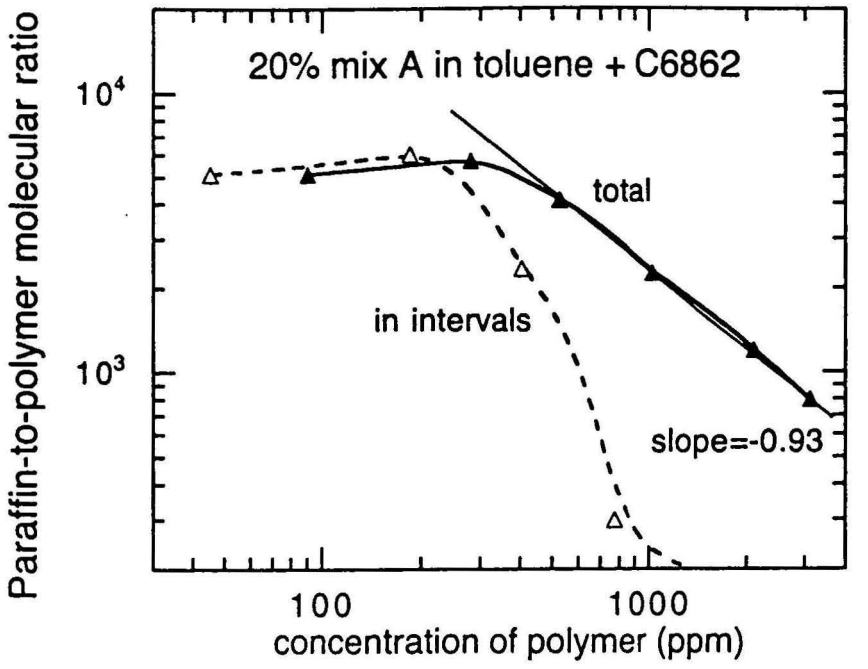

Figure 6.23: The paraffin-to-polymer molecular ratio for the 20% solution of mixture A in toluene containing the additive C6862. Lines are guide for the eye only.

in polystyrene equivalent units were used.

Figures 6.23, 6.24, 6.25 and 6.26 show the average number of paraffin molecules eliminated from the solidification process by a single polymer molecule, calculated for various combinations of the paraffin and additive concentrations in toluene and nitrobenzene. As discussed above, the additive action (i.e. the decrease of T_c per unit mass of additive) is most effective for the low polymer concentrations and saturates at about 1000 ppm. In order to reflect this changing response of mixture A to additives, we plot not only the paraffin-to-polymer molecular ratio for the total number of 'average' molecules of mixture A eliminated by a given additive concentration, but also the variation of this ratio in intervals between the two consecutive additive concentrations. It is the 'total' value that counts in the practical use of additives, but the 'in intervals' values better reflect the concentration dependence of the additive efficiency.

The most extensive data set has been obtained for additive C6862 in the toluene solutions of mixture A. For the 20% solution of A (figure 6.23), the paraffin-to-polymer molecular ratio (PPMR) is constant (about 6000) up to

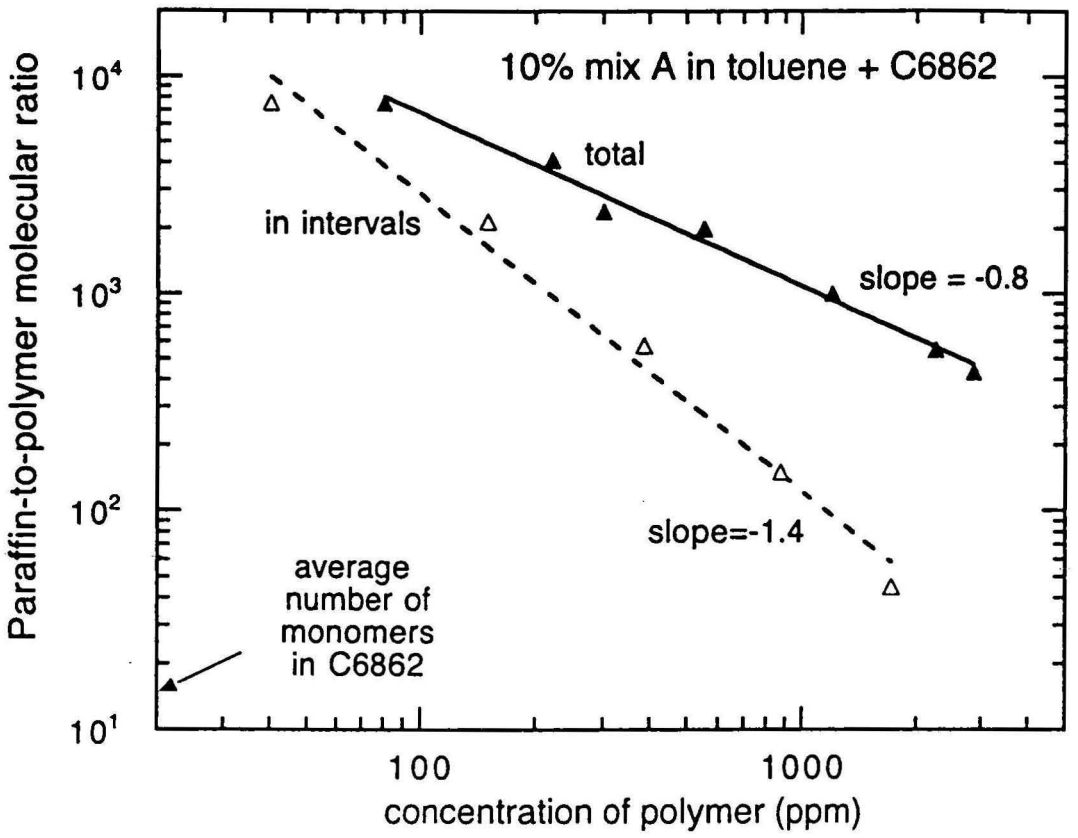

Figure 6.24: The paraffin-to-polymer molecular ratio for the 10% solution of mixture A in toluene containing the additive C6862. Lines are guide for the eye only.

the additive concentration of about 300 ppm. This concentration of additive eliminates from the crystallisation process about $8wt\%$ out of the total of $20wt\%$ of paraffins (figure 6.22). As the additive concentration increases above 300 ppm, the total PPMR decreases according to a power law with an exponent of -0.9. The 'in intervals' PPMR decreases steeply, thus reflecting the dramatic breakdown of the additive efficiency at higher concentrations. It can be seen from figure 6.23 that for the concentration of additive 1000 ppm one molecule of additive is about 60 times less efficient than in the peak at 100 ppm.

It is instructive to compare the above data with those presented in figure 6.24 for the same additive interacting with a 10% solution of mixture A in toluene. If the additive molecules were neutralising the paraffin molecules in a chemically non-specific way, one would expect the curves in figure 6.24 to coincide with their counterparts in figure 6.23 after the lower-concentration curves were horizontally shifted in such a way that the concentrations of paraffins remaining unaffected by the presence of additive were matched. This shift can be quantified from our T_c data (figure 6.19). For the 20% solution represented in figure 6.23 the concentration of free paraffins drops to 10% at about 400 ppm of the additive, which gives the required shift value for comparison with the 10% system (figure 6.24). Indeed, the slope of the 'total' curve for the 10% system is similar to the final slope of the 'total' curve for the 20% system and the order of magnitude of PPMR is the same in both cases. However, there is no exact match that would be expected for a strictly non-specific polymer-paraffin interaction.

In particular, the amount of paraffins neutralised by additive C6862 from the 20% solution of A in toluene saturates at 11.6%, regardless of the amount of additive. For the 10% solution, up to 5.8% of paraffins can be prevented from taking part in the crystallisation process (figure 6.22). The fact that these numbers remain in the same proportion to the original paraffin amount in the solution is most probably not fortuitous and strongly indicates that there is certain degree of chemical specifity that governs the process of paraffin-additive affinity. One of the possible interpretations would be that the additive efficiency saturates once the polymer-affine species of paraffins in mixture A have all grouped around the polymer molecules present in the solution.

The PPMR values for additive D6861 in the toluene solutions of mixture A (figure 6.25) are dramatically smaller than those discussed above for C6862. The maximum PPMR total value is about 500 for the 20% and 100 for 10% system. In the latter case we are approaching the $1:1$ ratio of paraffin molecules eliminated from the crystallisation process to the number of polymer monomers in solution. Quite obviously, such an additive is rather inefficient. As C6862 and D6861 additives have the same chemical structure of polymethylacrylate and almost identical number average molecular masses of about 5000 g/mole (table 6.1) and differ only in the number of carbon atoms in the side chains (12 for D6861 and 18 for C6862), one can relate the additive efficiency to the steric requirement of match between the side chain length and the average paraffin molecular length. The average paraffin molecular length in mixture A cor-

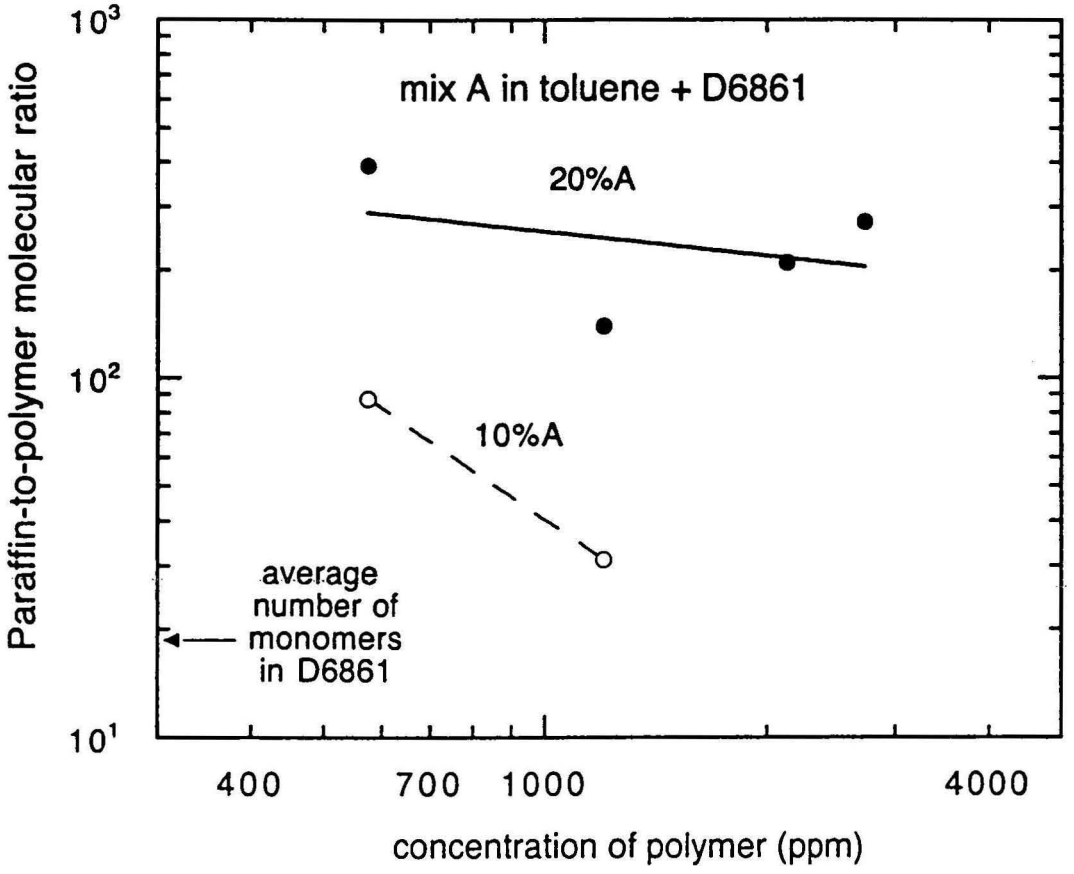

Figure 6.25: The paraffin-to-polymer molecular ratio for the 10% and 20% solutions of mixture A in toluene containing the additive C6861. Lines are guide for the eye only.

responds to 16 carbon atoms which closely matches the side chain length of C6862 but not that of D6861.

We finally discuss the solution of 20% mixture A in nitrobenzene, where data for all the four additives are available. The PPMR data are presented in two formats: one identical to that used for the toluene solutions (figure 6.26) and another based on the per monomer basis (figure 6.27). The first format is useful in order to make comparisons between data for additives acting in different solvents. The second one makes it possible to compare data for additives of markedly different molecular masses.

It is a striking result that the evolution of paraffin-to polymer molecular ratio (PPMR) for C6862 in the 20% nitrobenzene solution of mixture A (figure 6.26) is very similar to its behaviour in the 10% and 20% toluene solutions (figures 6.24 and 6.23). In particular, PPMR decreases from its maximum value of about 10000 at the additive concentration of about 100 ppm according to a power law with an exponent of -0.96. (However, no low concentration plateau is observed like for the 20% toluene solution). This result indicates a molecular-level universality of the polymer-paraffin interactions for the C6862 additive in different aromatic solvents. We note that in order to notice this universality it has been essential to calculate the paraffin-to-polymer molecular ratios; it is not apparent if corresponding T_c data for the different systems with additives are compared directly (see figures 6.19 and 6.18).

The PPMR data for the D6861 additive in nitrobenzene (figure 6.26) are again qualitatively similar to the corresponding data in toluene (figure 6.23), although there is a five-fold difference in the absolute magnitude. This may be an artefact, however, since both the nitrobenzene and toluene T_c data are grouped within a very narrow temperature range of about 1°C (figures 6.18 and 6.19) and, consequently, the systematic experimental error may be large.

The experimental PPMR points for the two heavy polymers, DB6858 and DB6860, are shown in figure 6.26 only for completeness; data for polymers of markedly different molecular masses should be discussed on a per monomer basis. Such a comparison is shown in figure 6.27. Although there is only one concentration studied (about 300 ppm) for each of the heavy additives, it appears that additives C6862 and DB6860 are most effective and group together. These additives have both 18 carbon atoms in their side chains and their corresponding number average molecular masses are 4900 and 41000, respectively. The remaining two additives, one light and one heavy, both with 12 carbon atoms in the side chains, appear to be markedly less effective in the nitrobenzene solutions of mixture A of paraffins.

In summary, it appears that close match between the side chain size and the n-alkane chain length is the most important factor for the effective polymethylacrylate additive T_c-depressant action in the toluene and nitrobenzene solutions of mixture A. The molecular mass may be important as much as it can affect the additive solubility. The choice of aromatic solvent seems to have little effect on the additive effectiveness at the molecular level (measured by PPMR).

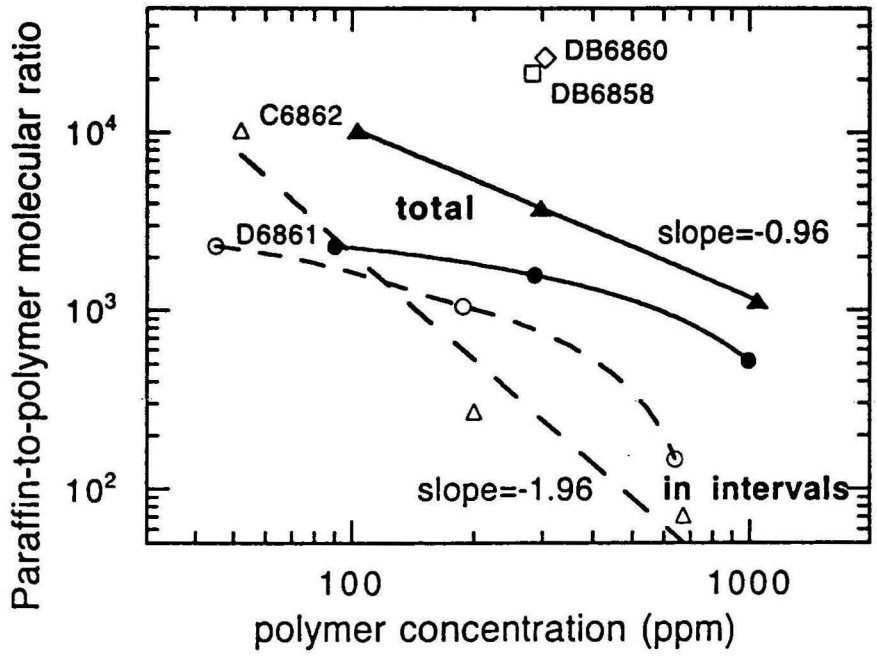

Figure 6.26: The paraffin-to-polymer molecular ratio for the 20% solutions of mixture A in nitrobenzene containing four different additives. The PPMR values have been calculated per one additive molecule. Lines are guide for the eye only.

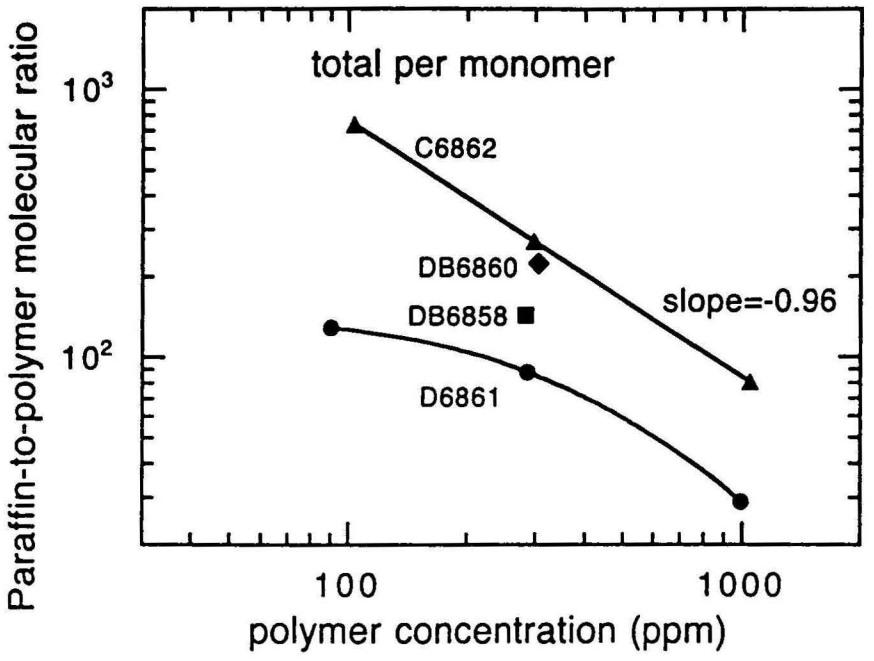

Figure 6.27: The paraffin-to-polymer molecular ratio (the 'total' values only) for the 20% solutions of mixture A in nitrobenzene containing four different additives. The PPMR values have been calculated per one additive monomer. Lines are guide for the eye only.

The absolute value of the decrease of the paraffin crystallisation temperature, however, strongly depends on the solvent via the concentration dependence of the liquidus line in the solvent - mixture A pseudo-binary phase diagram. For polymethylacrylates with 18-carbon side chain the average number of paraffin molecules per monomer eliminated from the crystallisation process varies from about 8000 at 100 ppm to 100 at 1000 ppm of the additive. For the additives with 12-carbon side chains these numbers are 10 to 100 times smaller.

6.5 Characterisation of additive molecules in toluene: a SANS study

Small Angle Neutron Scattering (SANS) is a standard method used to determine the size, shape and the molecular mass of polymers in solutions. In the context of the present study we considered it important to gain insight into the properties of additives in pure solvent (deuterated toluene in this case). Following the standard procedure, we have prepared a number of solutions of the additives in deuterated toluene in the concentration range 200 ppm to about 3000 ppm. The SANS spectra were obtained using the PAXE facility at Laboratoire Leon Brillouin in Saclay. The data were processed in a standard way described elsewhere in this report and the differential scattering cross sections in absolute units were obtained.

SANS data of the four additives in D-toluene solutions are presented in figures 6.28, 6.29, 6.30, 6.31 and 6.32. For all the cases we obtained smooth, featureless scattering curves that flatten out in the small-Q region. Such curves are typical for the polymer scattering in the dilute regime. The details of polymer molecule geometry (conformations) in solution are usually not known and may change depending on the polymer-solvent interaction. Therefore, instead of direct fits to theoretically-derived form factors the standard way of extracting the structural information from the scattering spectra is to construct the Zimm plot in the Guinier region, i.e. in the Q-range where the product $QR_g < 1$, where R_g is the radius of gyration of the polymer molecule.

The extent of the Guinier region depends on the experimentally accessible Q-range (specifically, its small-Q limit) and the size of scattering molecules. Typically, the modern SAXS and SANS facilities are sufficient for the studies of light polymers, whereas for heavy polymers the light scattering technique is more suitable as it enables one to access smaller Q-values. In the present study only data for the two light additives, D6861 and C6862, had overlap with the Guinier region. An attempt was made to acquire light scattering data for additives in toluene solutions, but that was unsuccessful owing to lack of dielectric contrast between the polymers and toluene.

Zimm plots for the two light additives, C6862 and D6861, are presented in figures 6.33, 6.34 and 6.35. The latter two plots correspond to the additive

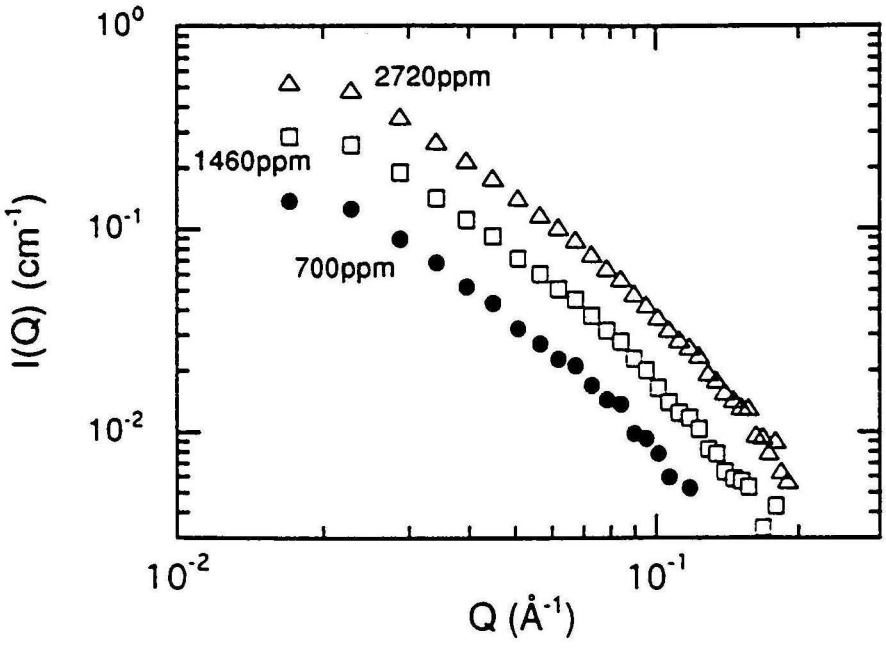

Figure 6.28: SANS data for additive DB6858 in toluene solutions at the temperature 13°C. Experimental curves for three additive concentrations are shown.

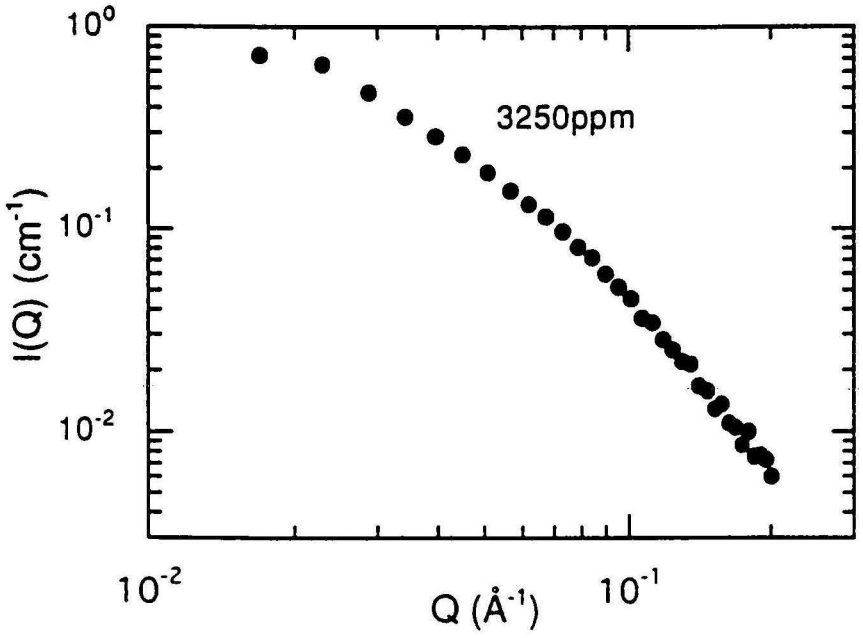

Figure 6.29: SANS data for additive DB6860 in toluene solution at the temperature 17°C. The additive concentrations is 3250 ppm.

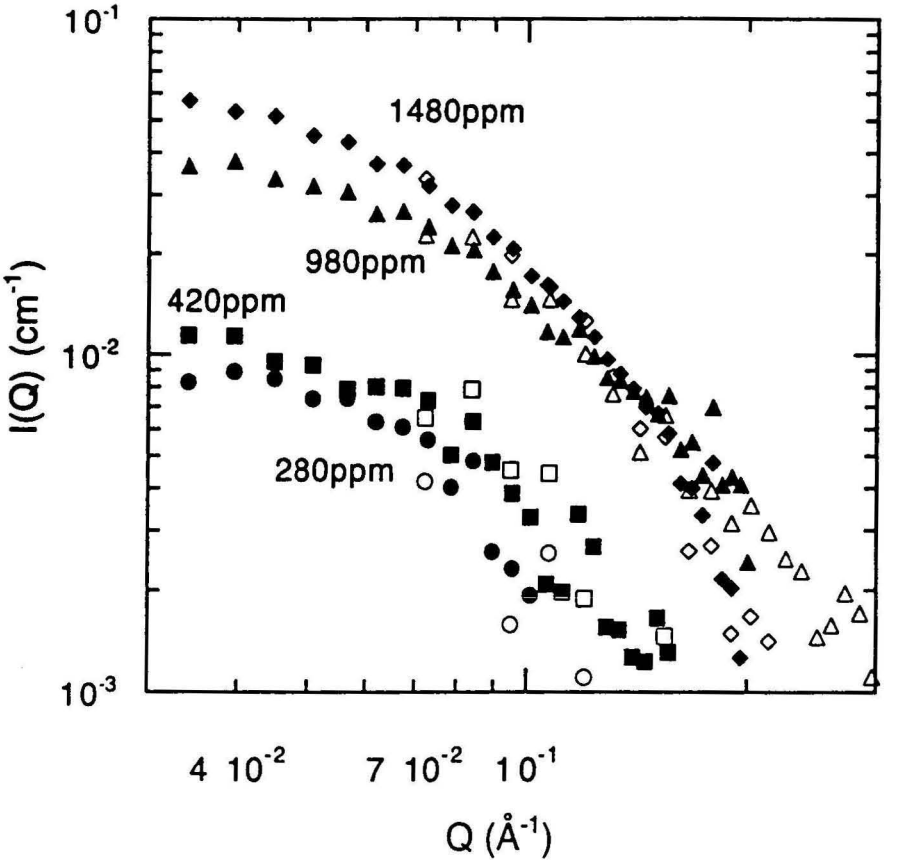

Figure 6.30: SANS data for additive C6862 in toluene solutions at the temperature 25°C. Experimental curves for four additive concentrations are shown. Full and empty symbols of the same shape correspond to two different experimental configurations.

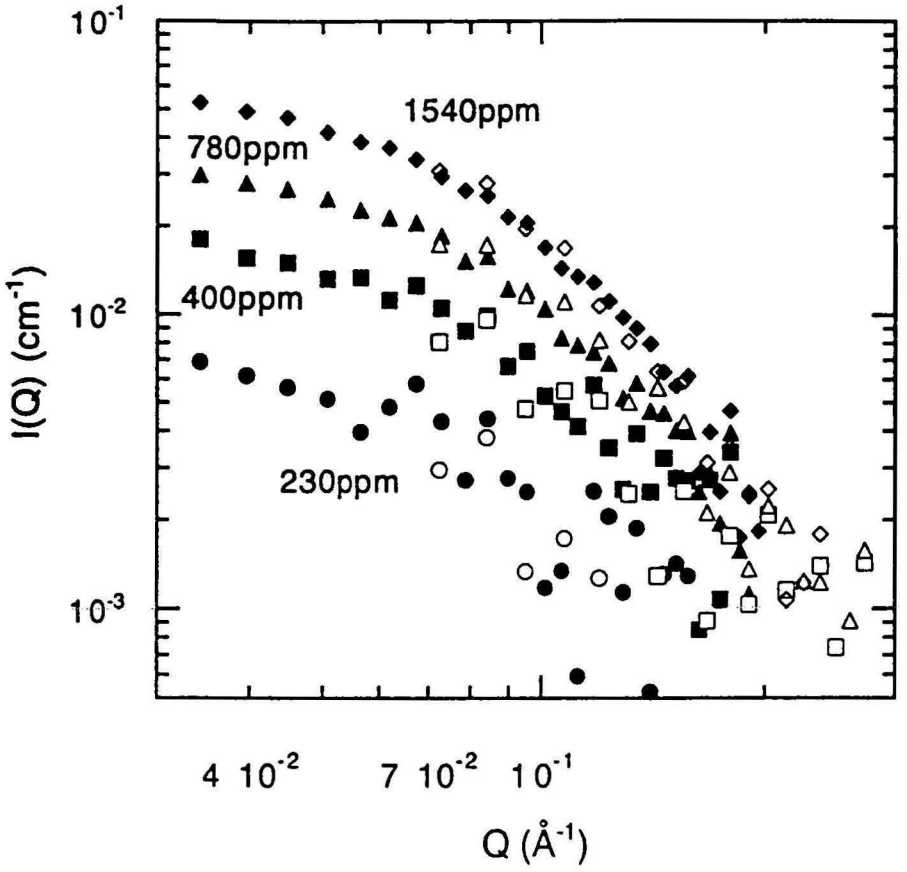

Figure 6.31: SANS data for additive D6861 in toluene solutions at the temperature 25°C. Experimental curves for four additive concentrations are shown. Full and empty symbols of the same shape correspond to two different experimental configurations.

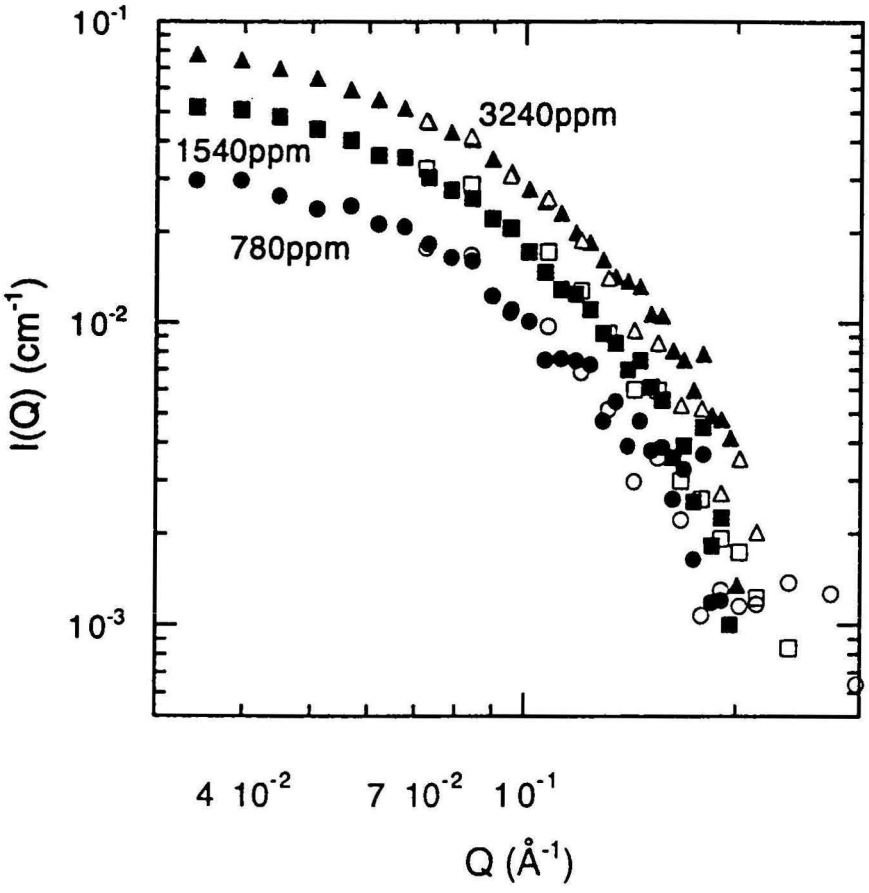

Figure 6.32: SANS data for additive D6861 in toluene solutions at the temperature $-7°C$. Experimental curves for three additive concentrations are shown. Full and empty symbols of the same shape correspond to two different experimental configurations.

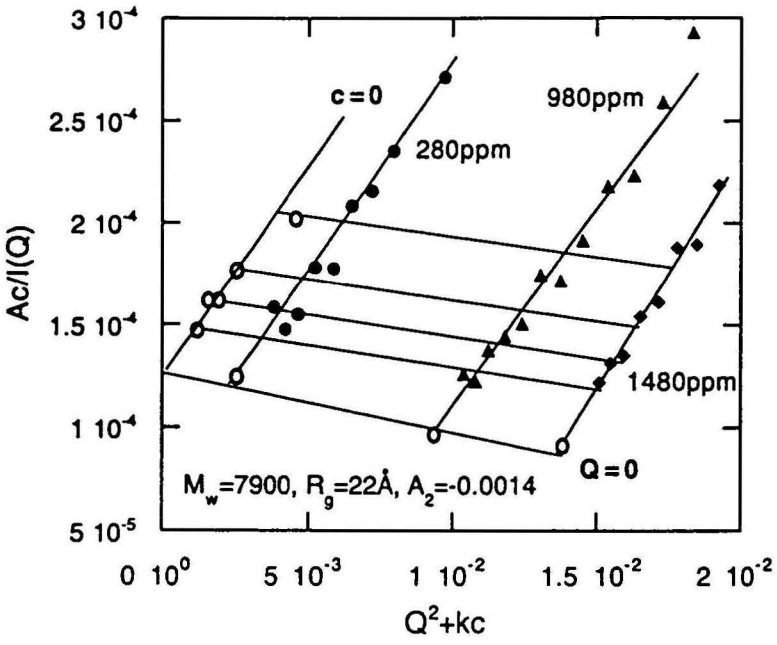

Figure 6.33: Zimm plot for the additive C6862 in deuterated toluene at the temperature 25°C.

D6861 at two different temperatures. Zimm plot is a graphical way of finding two limits for the experimental data, $c \rightarrow 0$ and $Q \rightarrow 0$. The molecular radius of gyration, R_g, and the second virial coefficient, A_2. are calculated from the slopes of the two limiting lines, $c = 0$ and $Q = 0$, respectively. The weight-average molecular mass, M_w, is determined by the point of intersection of these two lines.

The results are summarised in table 6.3. Data for additives C6862 and D6861 at 25°C indicate that the two polymers behave differently in toluene solutions. Despite nearly similar values of number average molecular mass (M_n is about 5000 g/mole for both additives), C6862 has a smaller M_w and smaller R_g than D6861. The most striking difference is the opposite sign of the second virial coefficient for the two polymers. For additive C6862 the value of A_2 is negative which indicates that toluene is a poor solvent and the polymer molecular form is compact, thus reflecting the attractive interactions between the monomers. For D6861, toluene is a good solvent and the molecule is more extended than for C6862. This may be partly contributed to, however, by the larger weight average molecular mass of D6861.

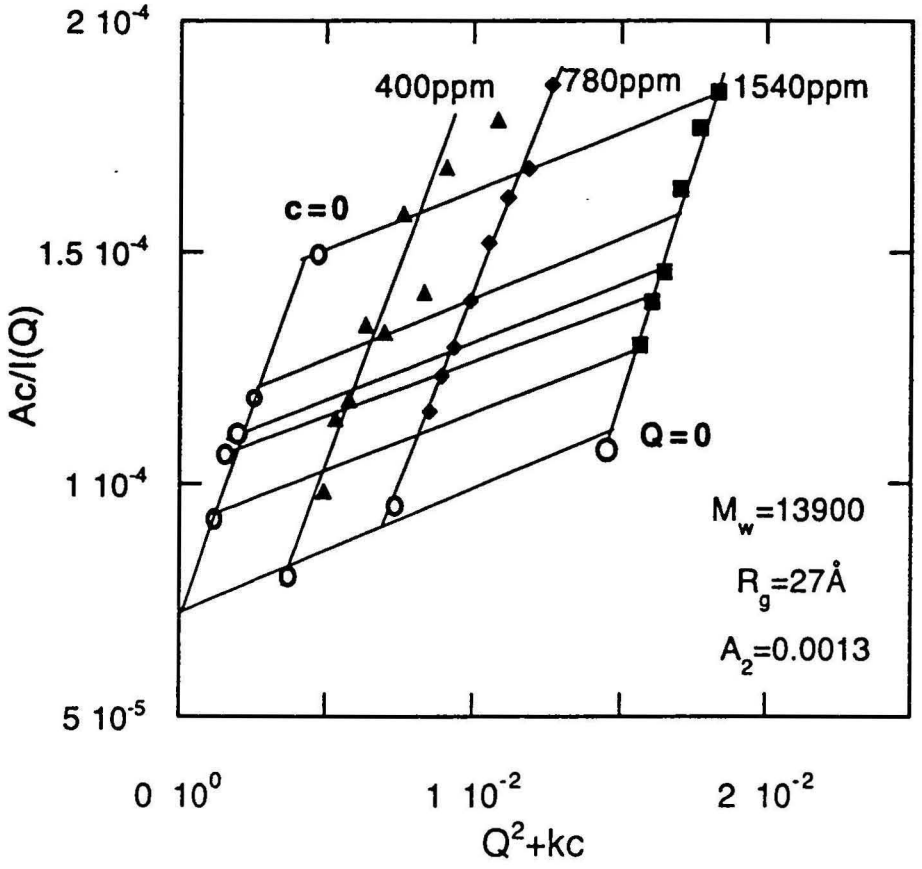

Figure 6.34: Zimm plot for the additive D6861 in deuterated toluene at the temperature 25°C.

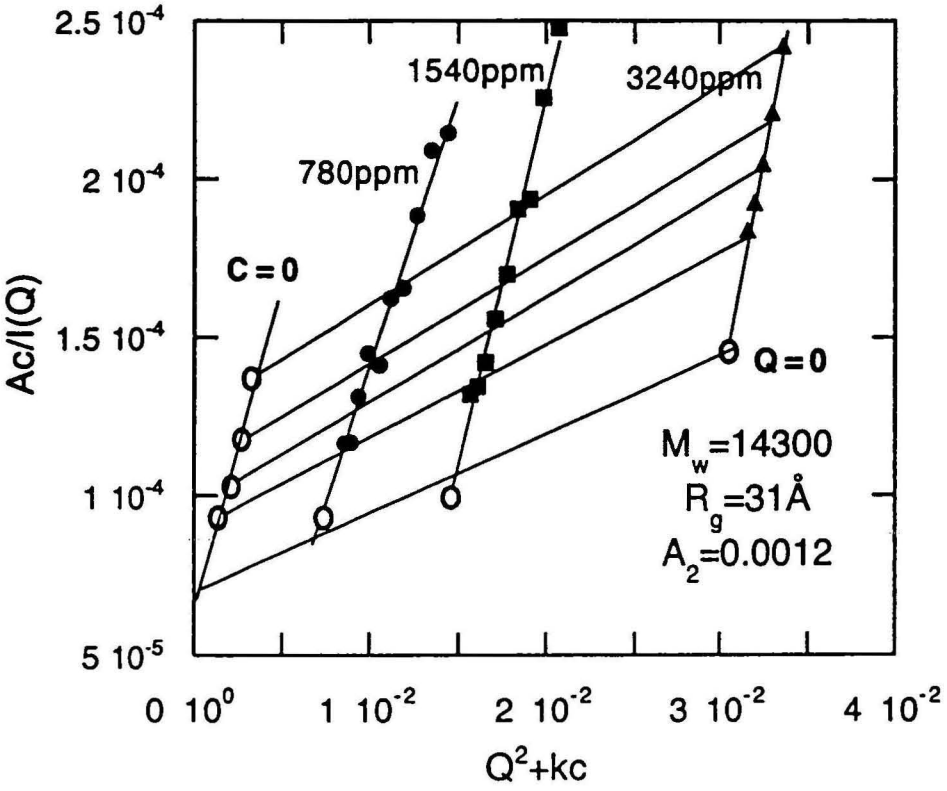

Figure 6.35: Zimm plot for the additive D6861 in deuterated toluene at the temperature −7°C.

Table 6.3: Parameters characterising the light additive behaviour in deuterated toluene solutions obtained from Zimm plots.

Additive name	M_w (g/mole)	R_g(Å)	A_2
C6862 at 25°C	7900	22	−0.0014
D6861 at 25°C	13900	27	0.0013
C6861 at −7°C	14300	31	0.0012

Another important finding is the thermal stability of the molecular configuration of additive D6861. The polymer characteristics derived from Zimm plots at 25°C and −7°C are very close to each other, thus indicating that there is no conformational change in this temperature range that might be brought about by, for instance, polymer crystallisation at low temperatures.

6.6 A structural model of additive-paraffin aggregation in toluene.

It is apparent from the PPMR data presented in figures 6.24, 6.23 and 6.27 that additives with 18 carbon atoms in the side chain, in particular C6862, are by far more effective than the ones containing 12 carbon atoms per side chain. Given the poor solubility of C6862 in toluene, one can propose the following T_c-depressant additive action model.

In solutions containing both aromatic solvent (toluene or nitrobenzene) and aliphatic paraffin molecules the aliphatic species tend to group around the chemically and sterically similar side chains of the additives. The closer the match between the polymer side chain length and the average paraffin chain length, the more effective this process becomes. Another important factor is the additive-solvent interaction. If it is repulsive, the aggregation of additive with aliphatic species becomes even more favoured, thus enhancing the additive effectivenes in terms of PPMR.

It follows from the PPMR data that for low concentrations (up to 100 ppm) of a light additive, on average up to 10000 of paraffin molecules can be associated with one 18-carbon side chain polymer molecule. This number decreases by an order of magnitude for additive concentrations of several thousands ppm. For the 12-carbon side chain additives the aliphatic cloud around the additive molecule may contain on average 30 to 2000 molecules of paraffins, depending on the additive species and concentration. Paraffin molecules are at higher concentration in the vicinity of the polymer molecule than in the bulk, but always

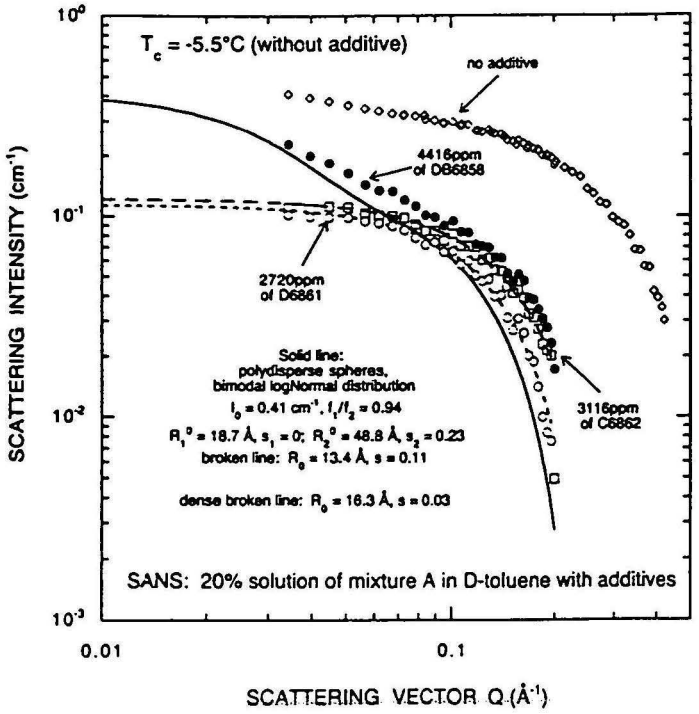

Figure 6.36: The effect of additives on SANS in the solution of 20% mixture A in toluene at 17°C.

remain molecularly mixed with the aromatic molecules of the solvent. All this indicates that the aliphatic cloud is a loosely bound, fluid object. It is not known whether the aliphatic cloud with a polymer molecule at its center solidifies at a higher or lower temperature than the bulk of the solution. According to our model, however, one important feature of this object is that it neither exchanges the aliphatic molecules with its neighbourhood nor grows in size during the crystallisation process, which lies at the heart of the T_c-depressant effect of the additive.

The presence of such dressed additive molecules in solution could be in principle detected using the SANS technique. Figure 6.36 shows SANS data for the 20% solution of mixture A in deuterated toluene containing high concentration of additives. As discussed above for solutions of mixture A without polymers (see figure 4.22), the scattering occurs on a bimodal distribution of spherical aggregates (centered around 5.25Å and 39.3Å), the smaller spheres being densely packed. The SANS data with additives (figure 6.36) indicate modifications to the structure of the scattering liquid: the small scattering objects become larger (the mean radii increase to 14 - 18Å), the large objects either disappear (for

D6861 and C6862) or grow in size (to 48.8Å radius for DB6858), and the contrast decreases. Both effects are qualitatively consistent with our structural model: the swollen spherical objects are aliphatic clouds around the additive molecules and the contract decreases because of the presence of deuterated toluene inside these objects. In order to fully test our model, however, additional SANS data would have to be acquired, in particular in the small-Q region.

Chapter 7

Pilot measurements

7.1 Observation of paraffin aggregates with a scanning tunneling microscope

7.1.1 Background.

It is a standard practice to cross-check the structural models derived from the interpretation of small angle scattering data using one or more methods of direct observation of the scattering objects. We have attempted to use the Scanning Tunneling Microscopy (STM) in order to observe the flat aggregates composed of several paraffin molecules whose presence in the liquid phase of mixture A in nitrobenzene has been adduced from our SANS and SAXS data. This has been a difficult task for several reasons. Firstly, the STM substrate has to be atomically flat, but must not be preferentially wetted by n-alkanes since this would cause a spontaneous growth of a paraffin layer. Secondly, in order to resolve the molecular structure of the aggregates special STM techniques may be needed and certainly very stable mechanical conditions are necessary. Thirdly, data have to be acquired from the liquid phase at a well controlled temperature just above T_c.

The STM system at our disposal was a basic Digital Instruments Nanoscope II. No liquid cell was available, there was no temperature control neither in the laboratory nor in the sample holder and the vibration environment was noisy. Also, no special techniques suitable for soft objects (e.g. the tapping mode) were available. In the view of this situation we have improvised some simple solutions which enabled us to test the usefulness of STM for our problem. Owing to the above limitations, however, the obtained data can be only considered as preliminary.

The natural choice of substrate for n-alkanes in STM experiments is highly oriented pyrolytic graphite (HOPG). In some previous studies, the physisorp-

tion of long chain n-alkane molecules from solutions has been observed at the graphite-solution interface ([48], [49], [50]) and solid-state transitions within adsorbed monolayers have been reported [51]. Those experiments have been performed using a specially designed, home-built STM equipment. In IFP, a molecular structure of a paraffinic layer adsorbed to HOPG from solution has been observed [52]. In this experiment it was noted that the individual molecules of light paraffins move across the substrate while being scanned by the tip. This effect may be expected to be amplified for very small aggregates of light paraffins in liquid solution being the object of the present study, as opposed to the solid phase layers studied previously.

7.1.2 Experimental procedures.

A slice of HOPG with freshly cleaved surface was placed in the STM's air cell. The tip was lowered into position and the image of substrate was taken. Next, several drops of the solution of 20% of mixture A in nitrobenzene were placed in the tip-substrate contact area using a syringe. Immediately after this step a number of open small glass containers filled with nitrobenzene were placed around the microscope and the entire area was sealed with a large glass bell. This created a saturated atmosphere of nitrobenzene around the microscope, thus preventing the specimen from evaporation. A number of STM images were taken over a period of several hours. The sample drop would eventually evaporate overnight. All images were recorded in the current mode. The currents used were either 50 pA or 950 pA and the bias was 20 mV.

Because of the potential health hazard associated with such a procedure, this was done only once and never repeated. Any further experiments in saturated atmosphere of an organic solvent would require design and construction of a specialised STM cell with controlled atmosphere and temperature.

7.1.3 Results and discussion.

We have captured a series of STM images of various objects which originate from the paraffin adsorption to HOPG substrate. Figure 7.1 shows the STM image of a freshly cleaved HOPG surface. One can clearly see a regular structure corresponding to individual carbon atoms. The measured interatomic distance corresponds to that expected for the graphite lattice. The following four photographs (7.2, 7.3, 7.4 and 7.5) show the top view and surface view of small objects whose size is about $3 \times 3 \times 0.45$ nm^3. These dimensions closely correspond to those predicted for the paraffin aggregates on the basis of the small angle scattering experiments.

As the solvent was slowly evaporating from the drop of liquid sample, we could observe the growth of paraffin aggregates on the HOPG substrate. Figure 7.6 shows a STM image of such aggregates at an early stage. As the growth

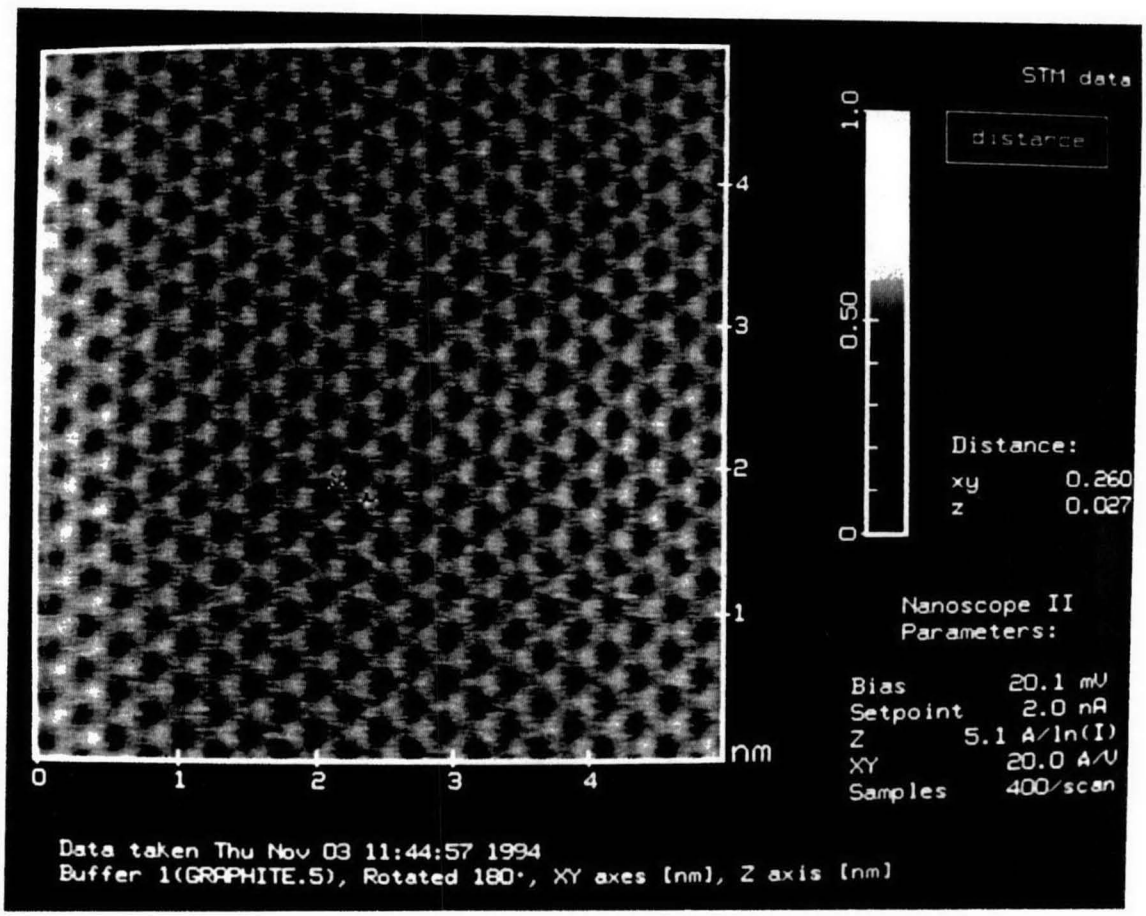

Figure 7.1: The STM image of a freshly cleaved surface of highly oriented pyrolytic graphite. Note the regular atomic structure of the graphite lattice.

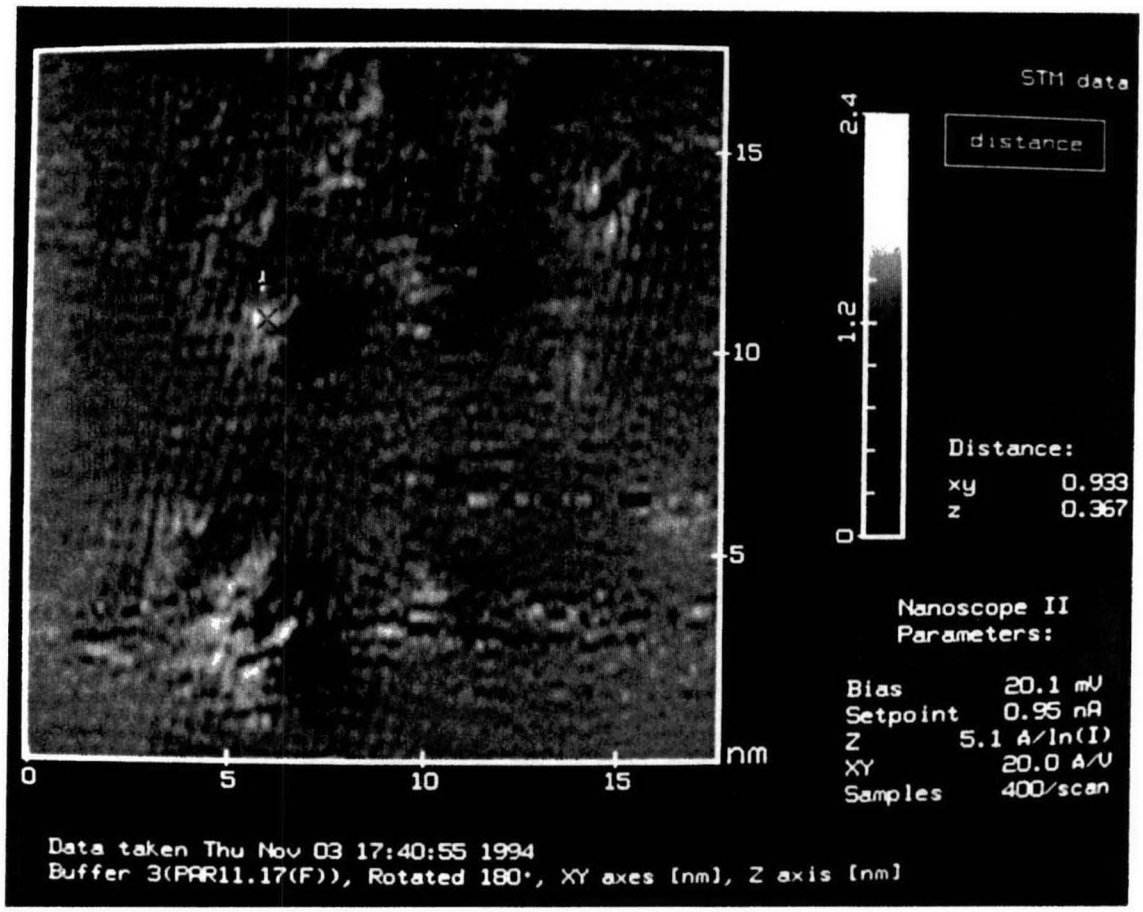

Figure 7.2: The STM image of a group of small deposits on the interface between HOPG and a solution of 20% of mixture A in nitrobenzene: top wiew.

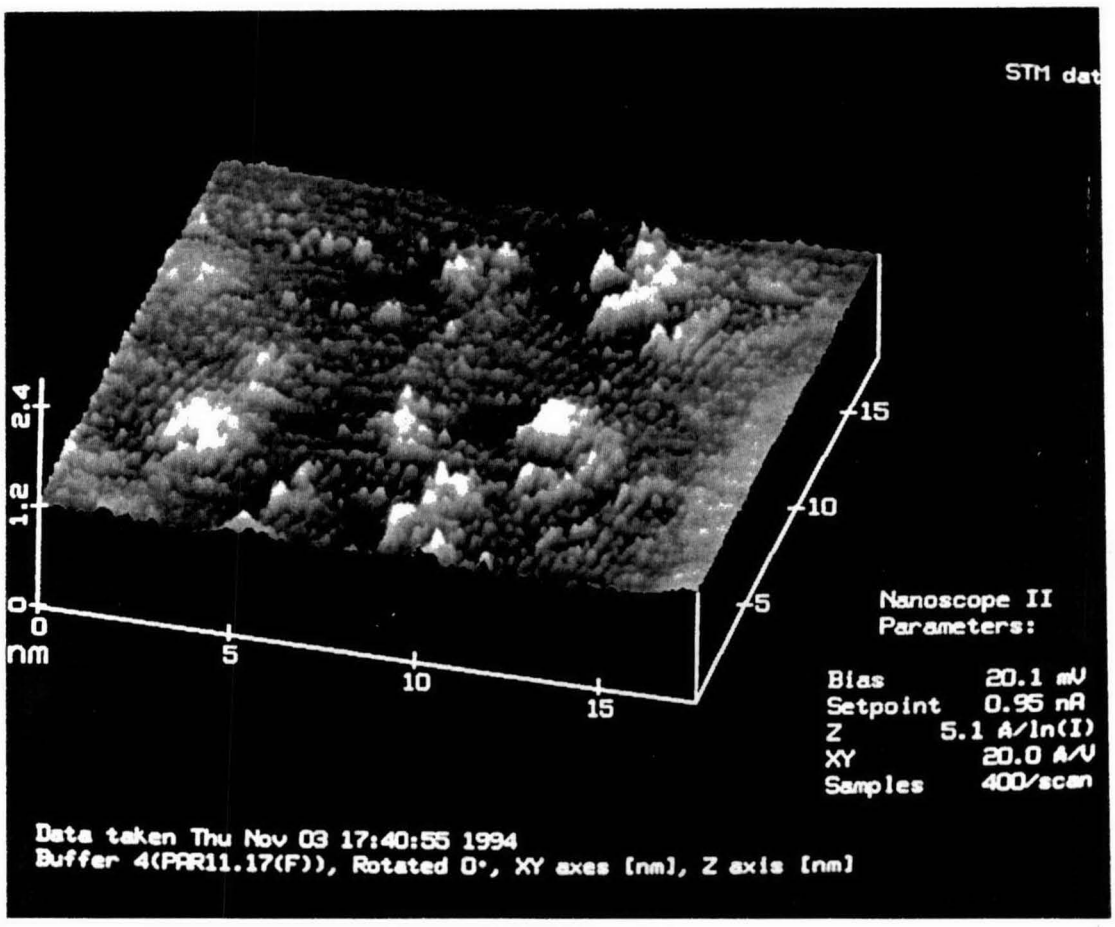

Figure 7.3: The STM image of a group of small deposits on the interface between HOPG and a solution of 20% of mixture A in nitrobenzene: surface view.

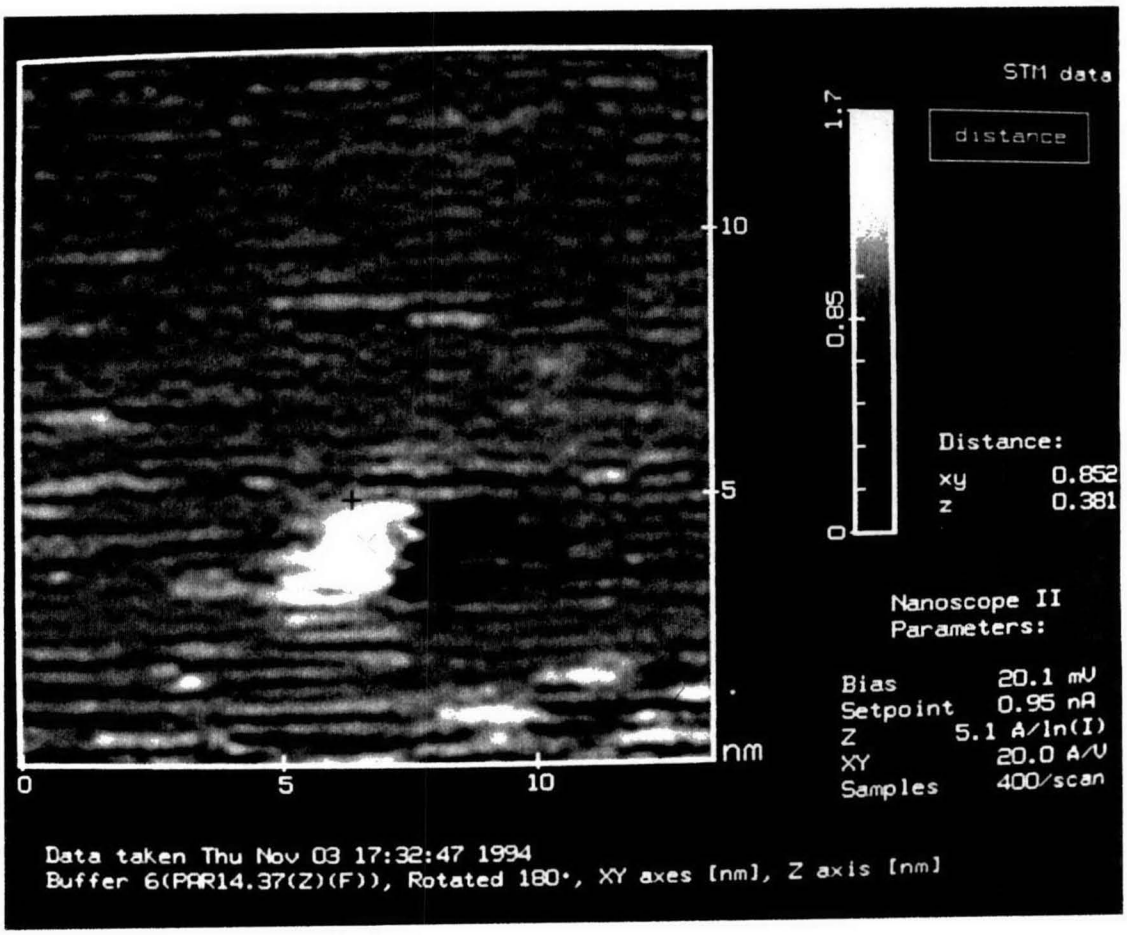

Figure 7.4: The STM image of a small deposit on the interface between HOPG and a solution of 20% of mixture A in nitrobenzene: top view.

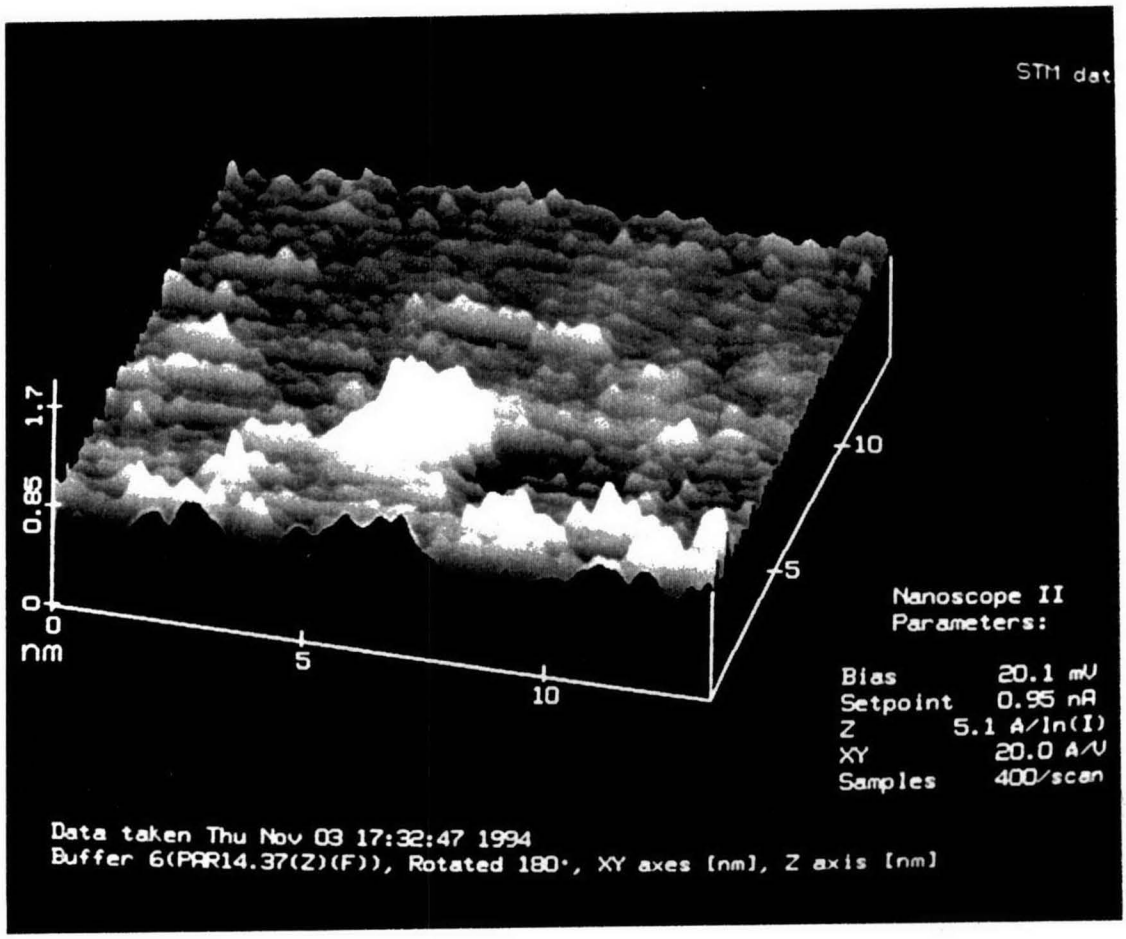

Figure 7.5: The STM image of a small deposit on the interface between HOPG and a solution of 20% of mixture A in nitrobenzene: surface view.

continued, all of the substrate would be eventually covered with a thick layer of paraffin.

We consider it a success that we have been able to observe the adsorbed objects of expected size and shape at all. However, these results cannot be considered conclusive since (1) data has not been obtained in a strictly controlled conditions, (2) the experiment was not repeated and (3) the atomic resolution of the paraffin images was not achieved.

7.2 Surface tension measurements on mixture A of paraffins near the freezing point

7.2.1 Background.

It has been recently discovered that pure normal alkanes above C14 exhibit a rare phenomenon of surface crystallisation ([53], [54], [55]). The experimental techniques used in the above work have been surface tension measurements ([53], [54], [55]), X-ray reflectivity, and grazing incidence X-ray diffraction [54]. The surface crystallisation phenomenon manifests itself as a marked decrease of surface tension in the temperature range between the surface crystallisation and bulk crystallisation. The reported studies pertained to various paraffins from C5 to C50 and it has been discovered that the existence and extent of the surface crystallisation region depends on the number of carbon atoms in the aliphatic chain.

The surface crystal of a pure paraffin is a highly ordered monolayer similar to the bulk rotator phase, in which the chains are vertically aligned and hexagonally packed with a long range positional order. For pure n-alkanes, the surface crystal exists at temperatures up to 3°C above the bulk freezing temperature, and its dependence on the number of carbon atoms can be quantitatively explained by a simple surface energy model [55].

Because in mixture A n-alkanes of different chain lengths are present, some of which exhibit surface crystallisation and some surface melting, it is not clear whether in this situation a surface crystalline layer would form. Furthermore, our interest in this subject is due to the fact that the limited growth of surface crystalline layer is associated with the limited wetting of solid phase by the liquid phase of n-alkane. This may be related to the phenomenon of paraffin aggregation into the limited size, flat objects which we have detected using the small angle scattering techniques.

7.2.2 Experimental procedures

The crucial requirement for the observations of surface crystallisation using the surface tension technique is precise control of temperature. In particular,

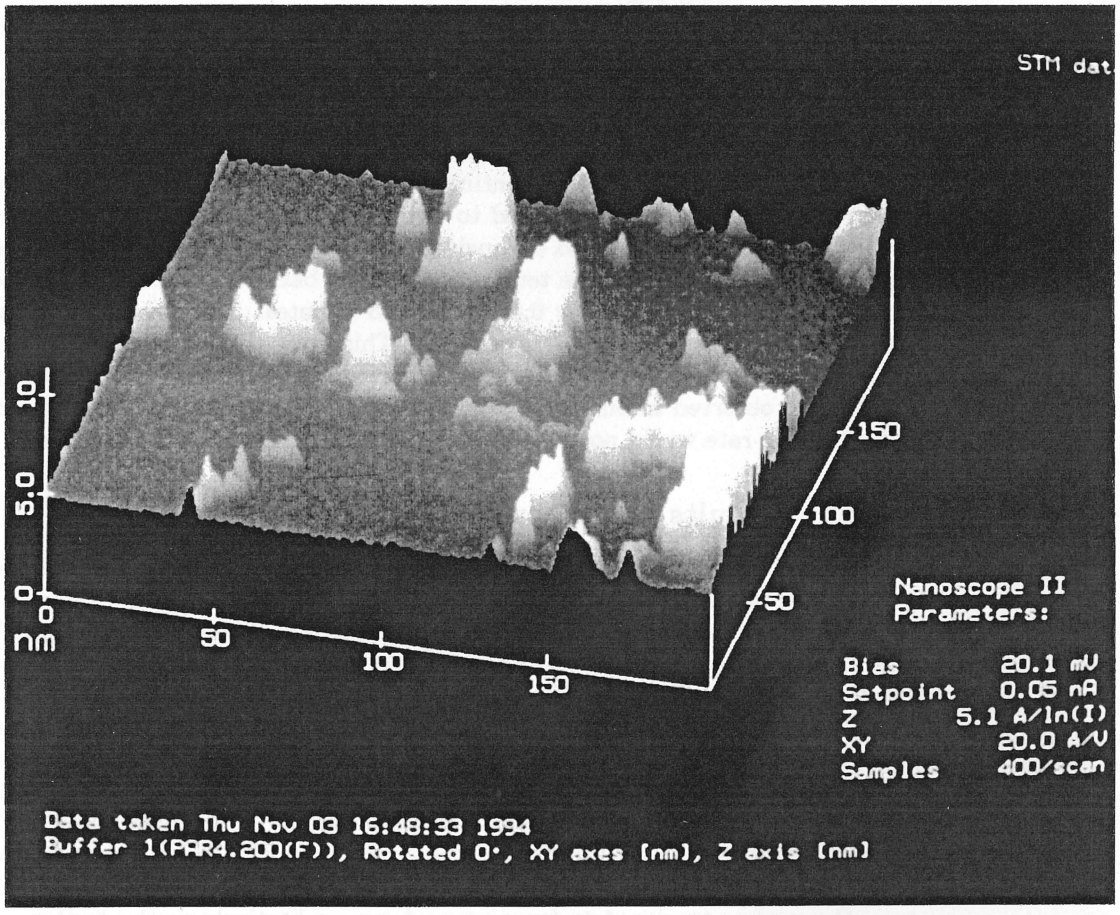

Figure 7.6: The STM image of a group of large deposits on the interface between HOPG and a solution of 20% of mixture A in nitrobenzene: surface view.

a homogeneous temperature distribution in the sample volume and very slow heating/cooling rates of the order of 0.1°C/hour are necessary.

Such experimental conditions could not be achieved with the equipment available at IFP and we have used the existing manually-controlled thermal bath installed on the Kruss Digital Tensiometer K10. Mixture A was placed in a standard 40 mm diameter glass container, cleaned in a standard way and whose purity was tested by measuring the surface tension of distilled water. After the tests, the water was removed and the container was dried using pure nitrogen gas. During measurements the container was sealed with a plastic cover with a slit in it, through which a platinum Wilhelmy plate was lowered into the liquid [56]. One end of a differential thermocouple was placed in liquid paraffin inside a glass jacket with clean external wall. The jacket was immersed next to the wall of the measurement container. The container was placed inside the standard Kruss heat-exchange vessel. The other end of the thermocouple was maintained at the temperature 0°C in a mixture of ice and distilled water.

The experimental data were continuously recorded using an X-Y chart recorder. The thermocouple voltage was fed to channel X and the surface tension (provided by the tensiometer) to channel Y. Two series of experiments have been performed, during which the temperature of the bath was manually decreased or increased, respectively, by 0.5°C every 15 minutes. This results in the average cooling/heating rate of 2 deg/hour. This rate is one order of magnitude faster than the optimal conditions, which most probably has caused the thermal hysteresis observed in our data. Unfortunately, any significantly smaller cooling/heating rate would not be practical with our experimental arrangement.

7.2.3 Results and discussion

The plots of surface tension versus temperature obtained on cooling and heating are shown in figure 7.7.

For pure paraffins one expects a gradual increase of surface tension as the temperature decreases towards the bulk freezing point, T_c. Recent studies of surface tension and X-ray reflectivity of pure normal alkane liquids have demonstrated that as the temperature decreases, a molecularly thin crystalline monolayer forms on the free liquid surface at the temperature T_s up to several degrees Centigrade above T_c ([53], [54], [55]). This phenomenon (called surface crystallisation) causes the surface tension to decrease steeply in the range between T_s and T_c. In thermal equilibrium conditions there should be no hysteresis between the cooling and heating cycle.

Our surface tension data for mixture A are qualitatively similar to those reported for heavier pure n-alkanes ([53], [54], [55]). As the temperature decreases, the surface tension initially increases and then drops steeply. The drop is not quite smooth, however, since one observes a structure at 15.5°C. It is possible that this structure reflects the incorporation of paraffins with different molecular weights into the surface crystalline layer, starting from the heavy ones. We

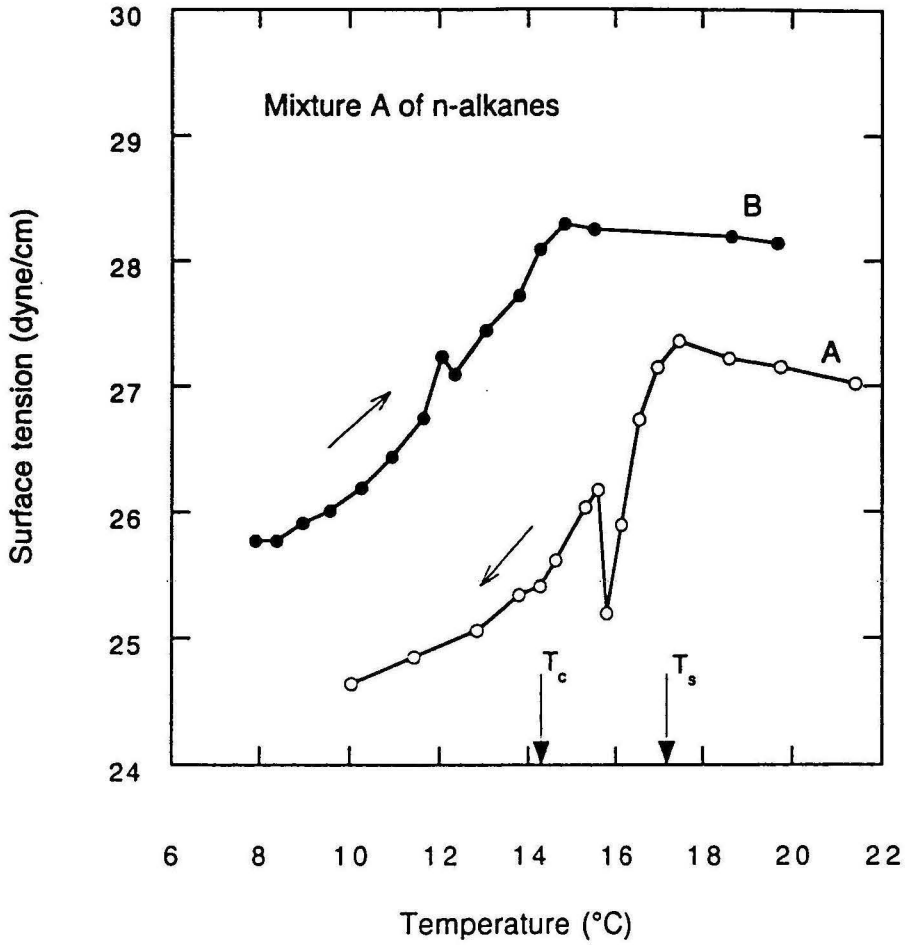

Figure 7.7: The temperature dependence of surface tension for pure mixture A. The bulk crystallisation temperature for pure mixture A is 14.2°C. Arrows indicate the values of T_c and T_s for curve A. Both the vertical and horizontal shift of curves A (cooling) and B (heating) is probably an experimental artefact.

also observe a pronounced hysteresis upon thermal cycling, which most probably is an experimental artefact caused by inadequate equilibration time allowed during heating. The absolute magnitudes of surface tension obtained by us at cooling and heating are slightly different, which is not expected.

We conclude that on the basis of our preliminary data it is likely that mixture A undergoes a surface crystallisation transition, with possible incorporation of different aliphatic species at different temperatures. Such process means formation of a molecularly thin crystaline layer on the liquid surface at the temperatures higher than the bulk crystallisation temperature. For quantitative studies of this phenomenon an improved temperature control would be necessary.

7.3 Dynamic light scattering from model fuels

Preliminary measurements of dynamic light scattering were performed for the 20% solution of mixture A in nitrobenzene. In a dynamic light scattering experiment the intensity of scattered light is measured as a function of time for a fixed value of the scattering vector **Q**. The time fluctuations of intensity are related to the molecular (Brownian) motion of the scattering particles. From the measured temporal behaviour of the intensity autocorrelation function the dynamic structure factor, $S(Q,\tau)$, is obtained. Since $S(Q,\tau) = exp(-D_oQ^2\tau)$, where D_o is the diffusion coefficient and τ is the time, the radius of the scattering particle can be determined from the Stokes formula $D_o = \frac{k_B T}{6\pi\eta a}$, where η is viscosity and T is the absolute temperature.

The dynamic light scattering has been measured for a sample of 20% mixture A in nitrobenzene at two temperatures: 23.4°C and 50°C. The paraffin crystallisation temperature in this solution is 18.3°C. From the analysis of the autocorrelation function a nearly monodisperse population of scattering objects of 4 nm diameter has been found. No objects were observed at 50°C. The results were reproducible after thermal cycling. These measurements provide an independent observation of paraffin aggregates which are present in solution just above the crystallisation temperature (23.4°C) but dissolve at high temperatures (50°C). This is fully consistent with our interpretation of SANS and SAXS results as well as with the direct observations by STM discussed in the previous section.

7.4 Near infrared absorption of crude oils

The observations of paraffin crystallisation by optical means can only be made in optically transparent media. There are problems for the crude oils since they are often opaque. Therefore, we have explored a possibility of doing optical observations in the near infrared spectral region for which commercial video cameras are available.

A typical absorption spectrum of a non-transparent crude oil in the near infrared spectral region 5000 cm^{-1} to 15000 cm^{-1} is shown in figure 7.8. It can be seen that there is a transmission window in the region 900 nm $\leq \lambda \leq$ 1700 nm in which even a 5 mm thick sample of crude oil would be transparent. We have obtained on loan an infrared Hamamatsu video camera and have directly confirmed the infrared transparency of black crude oils using the same optical system that was used by us for the transparent liquids. Therefore, with a set of infrared linear polarisers one could in principle make similar optical observations as those described elsewhere in this report for the transparent model fuels.

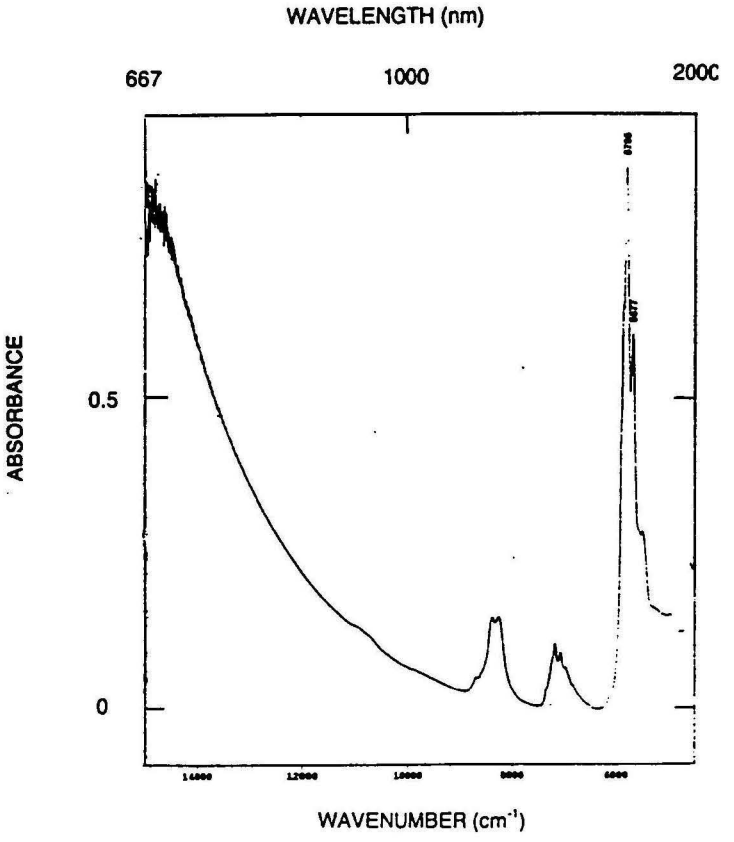

Figure 7.8: The absorption spectrum of a typical black crude oil. The units on abscissa are wavenumbers (measured in cm^{-1}) defined as $1/\lambda$, where λ is the wavelength. The spectral region covered by the spectrum is from about 660 nm to 2000 nm, with the wavelength increasing to the right. The visible spectral region extends from 400 nm (blue) to about 650 nm (red). The ordinate shows the product αd, where α is the absorption coefficient and d is the sample thickness; d = 2 mm in this case. A sample is considered opaque if αd is much larger than 1. This limit is reached for wavenumbers larger than 14000 cm^{-1}. The apparent decrease of the absorption curve on the left hand side of the spectrum is a purely electronic effect caused by the drop of the detector sensitivity combined with very low sample transmission. This is reflected in the high signal-to-noise ratio recorded in this region.

Bibliography

[1] B.P. Tissot and D.H. Welte, *Petroleum Formation and Occurence* **2nd edition**, 379 (Springer Verlag, Berlin 1984, 699p.)

[2] W.R. Turner, *Ind. Eng. Chem. Prod. Res. Develop.* **10**, 238-260 (1971)

[3] D.M. Small, ed., *Handbook of Lipid Research. The Physical Chemistry of Lipids: From Alkanes to Phospholipids* **vol. 4**, 183-232 and 561-575 (Plenum Press, New York 1986)

[4] D. Turnbull and L. Cormia, *Journal of Chemical Physics* **34**, 820-831 (1961)

[5] P.W. Teare, *Acta Crystallographica* **12**, 294-300 (1959)

[6] W. Piesczek, G.R. Strobl and K. Malzahn, *Acta Crystallographica* **B30**, 1278-1288 (1974)

[7] R.D. Heyding, K.E. Russell and T.L. Varty, *Powder Diffraction* **5**, 93-100 (1990)

[8] M. Maroncelli, S.P. Qi, H.L. Strauss and R.G. Snyder, *Journal of the American Chemical Society* **104**, 6237-4247 (1982)

[9] E.B. Sirota, H.E. King, Jr, D.M. Singer and H.H. Shao, *Journal of Chemical Physics* **98**, 5809-5824 (1993)

[10] J. Doucet, I. Denicolo and A. Craievich, *Journal of Chemical Physics* **75**, 1523 (1981)

[11] J. Doucet, I. Denicolo and A. Craievich, *Journal of Chemical Physics* **75**, 5125 (1981)

[12] M. Wesolowski, *Thermochimica Acta* **46**, 21-45 (1981)

[13] M. Chichkali and F.W. Jessen, *Industrial and Engineering Chemistry* **59**, 86-98 (1967)

[14] H.P. Ronningsen, B. Bjorndal, A.B. Hansen and W.B. Pedersen, *Energy and Fuels* **5**, 895-908 (1991)

[15] W.B. Pedersen, A.B. Hansen, E. Larsen, A.B. Nielsen and H.P. Ronningsen, *Energy and Fuels* **5**, 908-913 (1991)

[16] K.S. Pedersen, P. Skovborg and H.P. Ronningsen, *Energy and Fuels* **5**, 924-932 (1991)

[17] D.M. Small *Handbook of Lipid Research 4: The Physical Chemistry of Lipids: From Alkanes to Phospholipids* **4**, Plenum Press, New York 1986

[18] F.R.A. Neto, J.N. Cardoso, A.S. Pereira, M.C.Z. Fernandes, C.A. Caetano and A.L.C. Machado, *Journal of High Resolution Chromatography* **17**, 259-263 (1994)

[19] H.R. Faust, *Thermochimica Acta* **26**, 383-398 (1978)

[20] R. Miller and G. Dawson, *Thermochimica Acta* **41**, 93-105 (1980)

[21] F. Bosselet, J.M. Letoffe, P. Claudy, S. Esson and P. Valentin, *Thermochimica Acta* **70**, 7-18 (1883)

[22] F. Bosselet, J.M. Letoffe, P. Claudy and P. Valentin, *Thermochimica Acta* **70**, 19-34 (1883)

[23] F. Bosselet, J.M. Letoffe, P. Claudy, S. Esson and P. Valentin, *Thermochimica Acta* **70**, 35-47 (1883)

[24] D. Al-Sammerai, *Thermochimica Acta* **86**, 369-73 (1985)

[25] S.P. Shrivastava, R.S. Tandon, D.C. Pandey, D.C. Madhvaland S.K. Goyal, *Fuel* **72**,1345-1349 (1993)

[26] J.M. Letoffe, P. Claudy, M.V. Kok, M.Garcin and J.L. Volle, *Fuel* **74**, 810-817 (1995)

[27] J.C. Ravey, G. Ducouret and D. Espinat *Fuel* **67**, 1560-1567 (1988); Ch. Bardon, L. Barre, D. Espinat, V. Guille, M.-H. Li, J. Lambard, J.C. Ravey, E. Rosenberg and T. Zemb accepted by *Journal of Fuel Science and Technology*

[28] L. Clavel, *ETUDE DE LA CRISTALLISATION DES PARAFFINES DANS DES MELANGES COMPLEXES ET DES BRUTS A L'EQUILIBRE THERMODYNAMIQUE*, **RAPPORT CUST**, *Universite Blaise Pascal, Clermond-Ferrand 2* (1995)

[29] A. Guinier, G. Fournet, *Small Angle Scattering of X-rays* (Wiley Interscience, New York 1955)

[30] O. Glatter, O. Kratky, *Small Angle X-ray Scattering* (Academic Press, London 1982)

[31] P. Debye, A.M. Bueche, *Journal of Applied Physics* **20**, 518 (1949)

[32] B. Cabane, in: *Surfactant Solutions: New Methods of Investigation* ed. R. Zana (Marcel Dekker, New York 1987) p.57

[33] D. Espinat, *Revue de l'Institut Francais du Petrole* **45**, 1-131 (1990)

[34] G. Porod, *Colloid-Zeitschrift* **124**, 83 (1951)

[35] P. Debye, H.R. Anderson and H. Brumberger, *Journal of Applied Physics* **28**, 679-683 (1957)

[36] One of the general ways to formally approach the deconvolution problem is the maximum entropy method; see for instance J.D. Morrison, J.D. Corcoran and K.E. Lewis, *Journal of Applied Crystallography* **25**, 504 (1992)

[37] A. Guinier, *Compte rendu* **206**, 1641 (1938);**206**, 1374 (1938)

[38] B.H. Zimm, *Journal of Chemical Physics* **16**, 1093 (1948)

[39] P. Mittelbach, G. Porod, *Acta Physica Austriaca* **14**, 185-211 (1965)

[40] L.A. Feigin, D.I. Svergun, *Structure Analysis by Small Angle X-ray and Neutron Scattering* (Plenum Press, New York 1987)

[41] Literature on fractal scattering is extensive. For a review in geological context see, for instance: A.P. Radlinski, C.J. Boreham, G.D. Wignall and J.-S. Lin, *Physical Review B* **53**, 14152-14160 (1996)

[42] W.S. Dubner, J.M. Schultz and G.D. Wignall, *Journal of Applied Crystallography* **23**, 469 (1990)

[43] J. Denis and J.-P. Durand, J. Appell, P. Bassereau and J. Marignan, *Revue de l'Institut Francais du Petrole* **46**, 637 (1991)

[44] K. Lewtas, R. D. Tack, D. H. M. Beiny and J. W. Mullin, *Adv. Ind. Cryst.* **118**, 166 (1991)

[45] I. M. El-Gamal, E. A. M. Gad, S. Faramawi and S. Gobiel, *J. Chem. Tech. Biotechnol.* **55**, 123 (1992)

[46] P. Claudy, J.-P. Letoffe, B. Bonardi, D. Vassilakis and B. Damin, *Fuel*, **72**, 821 (1993)

[47] T. R. Coley *Diesel fuel additives influencing flow and storage properties* 105 (1986)

[48] G.H. Findenegg and H. Liphard, *Carbon* **25**, 119 (1987)

[49] G.C. McGonigal, R.H. Bernhardt and D.J. Thomson, *Applied Physics Letters* **57**, 289 (1990)

[50] J.P. Rabe and S. Buchholz, *Science* **253**, 424 (1991)

[51] L. Askadskaya and J.P. Rabe, *Physical Review Letters* **69**, 1395 (1992)

[52] F.Goffinont, *VISUALISATION IN-SITU PAR MICROSCOPIE A EFFET TUNNEL DE MOLECULES ORGANIQUES PHYSISORBEES SUR DU GRAPHITE*, **RAPPORT CUST**, *Universite Blaise Pascal, Clermond-Ferrand 2* (1994)

[53] J.C. Earnshaw and C.J. Hughes, *Physical Review A* **46**, R4494 (1992)

[54] X.Z. Wu, E.B. Sirota, S.K. Sinha, B.M. Ocko and M. Deutsch, *Physical Review Letters* **70**, 958 (1993)

[55] X.Z. Wu, B.M. Ocko, E.B. Sirota, S.K. Sinha, M. Deutsch, B.H. Cao and M.W. Kim *Science* **261**, 1018 (1993)

[56] C. Weser *GIT Fachzeitschrift fur das Laboratorium* **24**, 642-48 and 734-42 (1993), ed. G.I.T. Verlag Ernst Giebeler, Darmstadt

[57] G.W. Brady, C. Cohen-Addad and E.F.X. Lyden *The Journal of Chemical Physics* **51**, 4320 (1969)

[58] G.W. Brady and D.B. Fein *Journal of Applied Crystallography* **8**, 261 (1975) and references therein.

[59] A.P. Radlinski, L. Barre and D. Espinat *Journal of Molecular Structure* **383**, 51 (1996); presented at the conference on *Horizons in Small Angle Scattering from Mesoscopic Systems*, Stromboli, Italy, 27-30 September 1995.